

Reconstruction and reduction of uncertainties in aeroelastic systems

Sarma, Rakesh

DOI

[10.4233/uuid:4c3ba42f-091e-4b9a-b2bb-68e018a3d4db](https://doi.org/10.4233/uuid:4c3ba42f-091e-4b9a-b2bb-68e018a3d4db)

Publication date

2018

Document Version

Final published version

Citation (APA)

Sarma, R. (2018). *Reconstruction and reduction of uncertainties in aeroelastic systems*. [Dissertation (TU Delft), Delft University of Technology]. <https://doi.org/10.4233/uuid:4c3ba42f-091e-4b9a-b2bb-68e018a3d4db>

Important note

To cite this publication, please use the final published version (if applicable).
Please check the document version above.

Copyright

Other than for strictly personal use, it is not permitted to download, forward or distribute the text or part of it, without the consent of the author(s) and/or copyright holder(s), unless the work is under an open content license such as Creative Commons.

Takedown policy

Please contact us and provide details if you believe this document breaches copyrights.
We will remove access to the work immediately and investigate your claim.

RECONSTRUCTION AND REDUCTION OF UNCERTAINTIES IN AEROELASTIC SYSTEMS

RECONSTRUCTION AND REDUCTION OF UNCERTAINTIES IN AEROELASTIC SYSTEMS

Proefschrift

ter verkrijging van de graad van doctor aan de Technische
Universiteit Delft,
opgezag van de Rector Magnificus prof. dr. ir. T.H.J.J. van der Hagen,
voorzitter van het College voor Promoties,
in het openbaar te verdedigen op
woensdag 5 december 2018 om 10:00 uur

door

Rakesh SARMA

Master of Science, Indian Institute of Technology Jodhpur, India
geboren te Guwahati, Assam.

Dit proefschrift is goedgekeurd door de promotoren.

Samenstelling promotiecommissie bestaat uit:

| | |
|------------------------|---|
| Rector magnificus, | voorzitter |
| Prof. dr. ir. H. Bijl, | Universiteit Leiden, promoter |
| Dr. R.P. Dwight, | Technische Universiteit Delft, copromoter |

Onafhankelijke leden::

| | |
|-----------------------------------|--|
| Dr. S. Marques, | University of Surrey, UK |
| Prof. Dr. M.H. Hansen, | University of Southern Denmark |
| Prof. Dr. W. Zhang, | Northwestern Polytechnical University, China |
| Prof. dr. ir. J.W. van Wingerden, | Technische Universiteit Delft |
| Prof. dr. S. Hickel, | Technische Universiteit Delft, reservelid |

Overig lid:

| | |
|-----------------|-------------------------------|
| Dr. A.C. Viré , | Technische Universiteit Delft |
|-----------------|-------------------------------|

This work is part of the Industrial Partnership Programme "Computational Sciences for Energy Research" of the Foundation for Fundamental Research on Matter, which is now part of the Netherlands Organisation for Scientific Research (NWO-I). This research program is cofinanced by Shell Global Solutions International B.V. under project number 12CSER080. The research was conducted at the Delft University of Technology.



Nederlandse Organisatie voor Wetenschappelijk Onderzoek

Keywords: Aeroelasticity, ROMs, Uncertainty quantification

Printed by: Rijnja Repro

Front: Vortex shedding from wind turbine blade obtained in this dissertation.

Copyright © 2018 by R. Sarma

ISBN 978-94-6366-107-2

An electronic version of this dissertation is available at
<http://repository.tudelft.nl/>.

মোৰ গান হওঁক বহু আস্থাহীনতাৰ বিপৰীতে এক গভীৰ আস্থাৰ গান

মোৰ গান হওঁক কল্পনাবিলাসৰ বিপৰীতে এক সত্য প্ৰশস্তিৰ ধ্যান

ড: ভূপেন হাজৰিকা

CONTENTS

| | |
|--|-------------|
| Summary | xi |
| Samenvatting | xiii |
| 1 Introduction | 1 |
| 1.1 Background | 1 |
| 1.2 State-of-the-art - Wind turbine aeroelastics | 3 |
| 1.3 Aim of the dissertation | 5 |
| 1.4 Novelty and approach | 6 |
| 1.5 Outline | 7 |
| References | 7 |
| 2 Background - Aeroelasticity and uncertainty | 13 |
| 2.1 Aeroelasticity | 13 |
| 2.1.1 Navier-Stokes equations | 14 |
| 2.1.2 Structural equations - vibration theory | 17 |
| 2.1.3 Aeroelastic solver | 18 |
| 2.2 Instabilities in aeroelasticity | 21 |
| 2.2.1 Flight instabilities | 21 |
| 2.2.2 Wind turbine aeroelastic failure | 22 |
| 2.3 Reduced order modelling in aeroelasticity | 23 |
| 2.4 Uncertainties in aeroelasticity | 27 |
| 2.4.1 Uncertainty propagation | 29 |
| 2.4.2 Inverse UQ - Bayesian perspective | 29 |
| 2.5 Summary of methods | 30 |
| References | 31 |
| 3 Development of an aeroelastic solver | 39 |
| 3.1 Structural solver | 39 |
| 3.1.1 Sensitivity Analysis | 40 |
| 3.1.2 NACA 0012 airfoil and Goland Wing | 40 |
| 3.1.3 Wind turbine blade | 42 |

| | | |
|----------|--|------------|
| 3.2 | Mesh generation and fluid solver | 46 |
| 3.3 | Aeroelastic equations | 49 |
| 3.4 | Aeroelastic predictions. | 50 |
| 3.4.1 | Flutter boundary - NACA0012 airfoil and Goland wing | 50 |
| 3.4.2 | Validation of wind turbine dynamics by the aeroelastic code | 50 |
| 3.5 | Summary | 61 |
| | References | 61 |
| 4 | Aeroelastic predictions with ROMs | 65 |
| 4.1 | ARX model | 66 |
| 4.2 | LPV-ARX model formulation | 67 |
| 4.3 | Stability analysis of the aeroelastic system | 70 |
| 4.4 | Verification of ROM and aeroelastic estimates | 72 |
| 4.4.1 | Two-Degree-of-Freedom NACA 0012 Airfoil | 73 |
| 4.4.2 | Goland Wing | 75 |
| 4.4.3 | Computational gain with LPV-ARX | 78 |
| 4.5 | Wind turbine aeroelastic reconstructions | 78 |
| 4.5.1 | Verification of ARX - Reconstruction of forced motion | 80 |
| 4.5.2 | Verification of ARX for aeroelastics - Estimation of blade forcing | 80 |
| 4.6 | Summary | 83 |
| | References | 83 |
| 5 | Reduction of uncertainties employing Bayes' theorem | 85 |
| 5.1 | Uncertainty propagation and Bayesian updating | 85 |
| 5.1.1 | Defining and propagating priors on the structure | 87 |
| 5.1.2 | Bayesian uncertainty reduction using data. | 88 |
| 5.1.3 | Explicit expression for posterior of flutter density | 88 |
| 5.2 | UQ and Bayesian updating - Goland wing | 89 |
| 5.3 | UQ and Bayesian updating - Wind turbine. | 91 |
| 5.3.1 | Propagation of input uncertainties | 91 |
| 5.3.2 | Reduction of uncertainties. | 95 |
| | References | 105 |
| 6 | Conclusion | 107 |
| 6.1 | Contributions of the dissertation | 107 |
| 6.1.1 | Aeroelastic modelling | 107 |
| 6.1.2 | Data-driven ROMs | 109 |
| 6.1.3 | Uncertainty reduction | 110 |

| | | |
|----------|---|------------|
| 6.2 | Directions for future research | 111 |
| 6.2.1 | Aeroelastic modelling | 111 |
| 6.2.2 | Data-driven ROMs | 112 |
| 6.2.3 | Uncertainty reduction | 113 |
| 6.3 | Summary | 114 |
| | References | 114 |
| | Acknowledgements | 115 |
| A | Confidence intervals of blade moment | 117 |
| B | Infinite Plate Spline | 121 |
| C | Implementation of ARX | 125 |
| | Biography | 127 |
| | List of Publications | 129 |

SUMMARY

The growing demand for energy worldwide has resulted in the exploration and development of sustainable forms of energy, such as wind energy. Wind turbines are typically used to extract power from the wind through the rotational motion of blades, which are aeroelastic structures. Among other practical examples, aircraft wings are also aeroelastic in nature. Aeroelastic structures suffer from inherent instabilities and fatigue, and hence their design process requires characterisation of safe operating regimes in order to prevent failure. In this dissertation, we present a methodology for predicting dynamic aeroelastic behaviour, and additionally employing data from experiments to improve predictions. The methodology is demonstrated on three test-cases: a 2-DoF airfoil, the Golland wing and an experimental, downwind, wind turbine. The presented method is generic in terms of applicability to any aeroelastic problem, however considering the engineering and societal relevance, the wind turbine problem is extensively investigated. The dissertation contributes to three broad scientific domains - aeroelasticity, reduced order modelling and uncertainty quantification.

The first part of the dissertation presents the development of a high-fidelity aeroelastic solver based on Reynolds-averaged-Navier-Stokes equations, employing turbulence models based on the Boussinesq hypothesis. The solver simulates an experimentally tested 3-bladed wind turbine, which is of downwind orientation and the aeroelastic model considers all structural details of the turbine, such as the blade, nacelle and tower. The aeroelastic characteristics are validated by comparing the dynamic blade moment to experimental measurements of the wind turbine. Experimental results for the wind turbine are available in terms of variation in blade moment with respect to azimuthal position of the blade. The aeroelastic predictions of blade moment closely match the trend observed in experiments, and quantitatively, the computational estimates lie within the bounds of the experimental measurements at most azimuthal positions.

The second part of the dissertation concerns with the development of reduced order models (ROM) for predicting the aeroelastic characteristics. Since the high fidelity computational models are expensive for most practical dynamic problems, the ROM is intended to replace the fluid solver, which is responsible for bulk of the computational costs. The data-driven ROMs are based on a recurrence relation, mapping input displacements to output force distribution, where

the data for training is obtained from forced-motion simulations. Two types of models namely: Auto Regressive with eXogenous (ARX) model and Linear Parameter Varying (LPV) ARX model are developed. In order to train the model, chirp signals are employed to estimate the expansion coefficients utilising the data from the developed aeroelastic solver. For the wind turbine, the ARX model is augmented with a localised forcing term in order to account for the forcing introduced by the tower wake. The trained models are initially used to reconstruct test signals, and thereafter employed for flutter boundary and blade moment predictions, which are verified with the full solver estimates. Accurate reconstructions are obtained for all parametric investigations performed. These results are obtained with significant gain in the computational costs with respect to the full order solver.

The third part of this dissertation deals with the uncertainty quantification problem. The presence of uncertainties may significantly change the stability characteristics of the system. Also experimental measurements of the wind turbine confirm that uncertainties exist in the rotational speed of the turbine. In order to take into account effect of these parametric uncertainties on the dynamic aeroelastic behaviour, the most sensitive parameters are initially identified. Thereafter, these are propagated through the low-cost ROM, and a probabilistic estimate of the flutter boundary or blade moment is obtained. It is observed that the effect of the assumed uncertainties on the aeroelastic behaviour is significant. Finally, Bayesian updating of the identified uncertain parameters is performed. Experimental data from the wind turbine experiment is employed for the parameter estimation, where both structural and rotational parameters are considered. The parameter identification is able to clearly reveal correlation between structural parameters after updating with data, while the rotational parameter uncertainty is clearly reduced. The identified parameters are finally propagated through the ROM again in order to reduce the uncertainties in the aeroelastic characteristics. The framework is also tested for predicting transonic aeroelasticity in Goland wing, where it is established that data recorded from pre-flutter conditions can be utilised to reduce the uncertainty in the flutter density. The research presented in the three parts can be utilised and implemented for any industrial problem to obtain probabilistic aeroelastic predictions utilising real world data.

SAMENVATTING

De wereldwijde groeiende vraag naar energie heeft geleid tot de exploratie en ontwikkeling van duurzame vormen van energie, zoals windenergie. Windturbines zijn ontworpen om energie uit de wind te onttrekken door de rotationele beweging van de bladen, wat aero-elastische constructies zijn. Een ander voorbeeld zijn vliegtuigvleugels, welke van nature ook aero-elastisch zijn. Aero-elastische constructies lijden aan inherente instabiliteit en vermoeidheid, waardoor het genoodzaakt is dat het ontwerpproces een karakterisatie van veilige operationele regimes bevat om storingen te voorkomen. In deze dissertatie presenteren we een methodologie voor de voorspelling van dynamisch aeroelastisch gedrag, en het gebruik van experimentele data ten behoeve van de verbetering van de voorspellingen. De methodologie wordt gepresenteerd middels drie testgevallen: een vliegtuig profiel met twee vrijheidsgraden, de Goland vleugel, en een experimentele benedenwindse windturbine. De gepresenteerde methode is algemeen toepasbaar op elk aero-elastisch probleem, maar gezien de bouwkundige en sociale relevantie wordt het windturbine probleem intensief bestudeerd. De dissertatie voegt toe aan drie brede wetenschappelijke domeinen – aero-elasticiteit, modellering van gereduceerde orde en de kwantificatie van onzekerheid.

Het eerste deel van deze dissertatie presenteert de ontwikkeling van een aero-elastisch model van hoge betrouwbaarheid gebaseerd op de zogeheten Reynolds-Averaged Navier-Stokes vergelijkingen, welke turbulentiemodellen toepassen gebaseerd op de hypothese van Boussinesq. Het computermodel simuleert een experimenteel geteste benedenwindse windturbine met drie bladen, waarin een aero-elastische model alle structurele details van de turbine in overweging neemt, zoals de bladen, gondel en de toren. Experimentele resultaten voor de windturbine zijn beschikbaar in de vorm van de variatie van het bladmoment ten opzichte van de azimuthale positie van het blad. De aero-elastische voorspellingen van het bladmoment komen goed overeen met de trend van het experiment, en kwantitatief liggen de computervoorspellingen tussen de grenzen van de experimentele onzekerheid bij de meeste azimuthale posities.

Het tweede deel van de dissertatie houdt zich bezig met de ontwikkeling van Modellen van geReduceerde Orde (MRO) voor het voorspellen van aero-elastische kenmerken. Aangezien de referentie computermodellen te duur zijn voor de meeste praktische toepassingen, is het MRO bedoeld om het vloeistofmo-

del te vervangen, welke verantwoordelijk is voor het merendeel van de computationele kosten. De door gegevensgestuurde MRO zijn gebaseerd op een recursie-relatie welke invoerverplaatsingen naar een uitvoer krachtdistributie mappen, waar de trainingsdata uit simulaties met geforceerde beweging komen. Twee modellen worden ontwikkeld, namelijk een AutoRegressief model met eXogene variabelen (ARX) en een Linear Parameter Variërend (LPV) model. Om het model te trainen worden zogeheten 'chirp' signalen gebruikt om de expansiecoëfficiënten te schatten met behulp van data komende uit het onwikkelde aero-elastisch model. Voor de windturbine, wordt het ARX model aangevuld met een gelocaliseerde drijvingsterm om rekening te houden met drijving geïntroduceerd door het torenzorg. De getrainde modellen worden in eerste plaats gebruikt om de testsignalen te reproduceren, en daarna voor het voorspellen van de fluttergrens en het bladmoment, welke geverifieerd worden met voorspellingen van het volledige computermodel. Nauwkeurige reconstructies zijn verkregen voor alle uitgevoerde parameterstudies. Deze resultaten zijn verkregen met een significante winst in de computationele kosten ten opzichte van het volledige model.

Het derde deel van deze dissertatie heeft betrekking op het kwantificeren van onzekerheid. De aanwezigheid van onzekerheden kan leiden tot een significant andere stabiliteit van het systeem. De experimentele meetwaarden bevestigen ook dat er onzekerheden bestaan in de rotationele snelheid van de turbine. Om het effect van deze parameteronzekerheden op het dynamisch aero-elastisch gedrag in overweging te nemen, worden in eerste instantie de meest gevoelige parameters geïdentificeerd. Daarna worden deze gepropageerd door het MRO, waarna een probabilistische schatting van het bladmoment wordt verkregen. Het effect van de aangenomen parameteronzekerheid op het aeroelastische gedrag is significant. Tenslotte wordt Bayesiaanse inferentie van de geïdentificeerde parameters uitgevoerd. Experimentele data van het windturbine experiment wordt gebruikt voor de parameter schatting, waarbij zowel de structurele als de rotationele parameters in overweging worden genomen. De parameteridentificatie is in staat om duidelijk de correlatie tussen structurele parameters te duiden na het observeren van de data, en de rotationele parameteronzekerheid is sterk verminderd. Daarna worden deze variabelen door het MRO gepropageerd om ook de onzekerheid in het aero-elastisch gedrag te verminderen. Deze methode is ook getest op de voorspellingen van transsone aero-elasticiteit in een Goland vleugel, waarbij het vastgesteld wordt dat de data van pre-flutter condities gebruikt kan worden om de onzekerheid in de flutterdichtheid terug te brengen. Het onderzoek gepresenteerd in de drie delen kan gebruikt en geïmplementeerd worden voor elk industrieel probleem om probabilistische aero-elastische voorspellingen te verkrijgen middels reële data.

1

INTRODUCTION

It is a truth very certain that when it is not in our power to determine what is true we ought to follow what is most probable.

René Descartes - Discourse on the Method

1.1. BACKGROUND

Aeroelastic systems (e.g. aircraft and wind turbines), also known as fluid structure interaction (FSI) systems, suffer from inherent instabilities and structural fatigue, which can lead to failure. For example, flutter is a form of dynamic instability in aircraft occurring as a result of unfavourable coupling of structural modes, which can ultimately lead to structural failure of the system. The instabilities arise for certain values of bifurcation parameters - notably, Mach number (ratio of speed of aircraft to speed of sound) and the altitude of flight. Thus an aircraft during flight must be operated away from the unstable Mach number - altitude regime. This prompts the requirement of characterising the stability of aeroelastic systems for all possible operating conditions.

This process of characterisation can be performed experimentally as well as numerically. Experimental techniques can provide accurate estimates, but may incur large costs, and failure tests are potentially dangerous. As such, numerical techniques are preferred, at least in the preliminary design phase. Although there have been substantial developments in simulation codes for complex aeroelastic systems such as wind turbines [1–3], significant discrepancies still exist between

numerical and experimental results. Thus there exists the challenge to numerically predict the behaviour of these systems with acceptable error. Numerical investigations also have errors for implementation in aeroelastic problems. Firstly, the numerical codes of aeroelastic systems are generally very computationally expensive. For example, the computation time for a converged simulation of the NREL rotor [4] for 5 rotor revolutions using 128 CPUs and a RANS-based solver (high fidelity) was about 1080 hours, dominated by the fluid component [5]. Design/optimisation in these systems can be intractable without significant computational resources. As such, industrial design procedures mostly employ simpler low fidelity models, which result in significant differences with respect to experimental results and missing physics. In this dissertation, high-fidelity solvers are employed to model the aerodynamics. The goal of this dissertation is cost-reduction of the high fidelity solvers using reduced order models in a data-driven framework.

One of the numerical solvers that will be developed in this dissertation is for a wind turbine of downwind configuration, in which case the rotor is placed on the lee side of the tower. Most popular industrial wind turbines are of upwind configuration, however the downwind orientation provides many advantages. The blade-to-tower clearance is a major design consideration in upwind turbines, which is completely eliminated in downwind configuration. This will enable designers to use flexible blades, which provides opportunities to reduce blade material and consequent reduction in transmitted loads to tower, hub and gearbox. Also downwind configuration can utilise the centrifugal forces during operation to reduce blade root bending moments. The reader is referred to [6] for further details about the advantages of downwind configuration. However, a major problem with downwind wind turbines is the tower shadow effect, which is caused by the tower wake in the form of impulsive forcing on the blade at every rotation. This phenomenon has not been extensively characterised with high-fidelity aeroelastic solvers owing to the numerical complexity and high computational costs, hence most of the numerical developments are based on empirical solvers to reduce the simulation time. Other disadvantages include identification of proper control strategies, details of which can be accessed from [6]. In this dissertation, the tower shadow effect of a downwind, wind turbine will be characterised through a high-fidelity solver and then subsequently, reduced order models will be trained to predict this effect.

A secondary, separate issue affecting the accuracy of simulations are the inherent parametric uncertainties in aeroelasticity. Important parameters are often imprecisely known such as the structural parameters, e.g. stiffness of wing and the imposed boundary conditions, e.g. inlet Mach number. Wind turbines specially suffer from varying flow conditions as a result of the intermittent nature

of the wind [7, 8] and due to turbulence in the atmospheric boundary-layer. This is mostly not taken into account during the blade design process as stochastic analysis requires multiple runs of the expensive computational solver to obtain acceptably accurate statistics. Thus there is a clear deficiency in current design practice. Simultaneously, the increased amount of instrumentation associated with modern wind turbines leads to the availability of large data-sets (of e.g. lidar/accelerometer/strain gauge data) from experimental systems. There is an opportunity to use this information to update the computational models as well as to reduce the associated uncertainties in the flow conditions using statistical techniques [9, 10], which will be performed in this dissertation.

1.2. STATE-OF-THE-ART - WIND TURBINE AEROELASTICS

In order to obtain physically accurate solutions, a high fidelity computational model is unavoidable for some complex aeroelastic systems. Specifically with respect to downwind wind turbines, only Navier-Stokes provides solutions with acceptable error, including all physics of the rotor-tower interaction. A comprehensive review of the development of aeroelastic studies of wind turbine blades has been presented in [11]. For modelling the aerodynamics of wind turbines, four types of models have been used: the BEM (blade element momentum) model, vortex models, actuator type models and finite-difference or finite-volume based high-fidelity CFD (computational fluid dynamics) models [11]. BEM is the most extensively used in wind turbine engineering since it is fast and provides accurate forces when reliable aerodynamic force data is available. However because of quasi steady and 2D flow assumptions, it is not able to predict accurate blade loads close to the boundaries of the operating regime. The vortex model on the other hand, ignores viscous effects which limits its application. The actuator model provides more information on wake dynamics, but is computationally more expensive. Moreover, being reliant on the aerodynamic measurement data, it does not generally predict more accurate load estimates, compared to BEM. The "CFD" model considers the full Navier-Stokes equations, is capable of modelling complex 3D flows and providing accurate estimates of blade moments, which is essential in order to predict instabilities. The high computational costs of CFD simulations limits their use in industrial applications. However, in some problems, e.g. downwind wind turbines, Navier-Stokes is the only one of the above models that accurately accounts for tower-blade interactions.

In the published literature, 3D Navier-Stokes aerodynamic/aeroelastic simulations for wind turbines with structural details of the wind turbine such as tower and nacelle have been considered in only a few studies [12–16]. Multiple investigations have been performed considering only the aerodynamics [17–20], while structural analysis of rotor blades with complex geometry and material compo-

sitions has also been performed [21–23]. The aerodynamic computations have mostly been performed with some limitations, e.g. consideration of a simplified geometric representation. One of the first 3-D simulations of wind turbine rotors at full scale was reported in [24] for fluid structure interaction (FSI) modelling of the NREL 5MW offshore rotor, however the effect of the tower and nacelle was ignored. This study was followed up with a more detailed representation of the rotor-tower interaction in [25] and then demonstrated in a Windspire Vertical Axis Wind Turbine (VAWT) [15]. The type of coupling between the CFD and structural solvers in aeroelastic simulations determines the consistency in forces and accelerations. In this regard, there have been developments based on loose coupling [26] and tightly coupled methods [5]. All these aeroelastic simulations consider an upwind configuration of the wind turbine. In this dissertation, we consider for the first time a downwind configuration, that has to deal with more complex flow features, since the blades are subjected to the tower wake at each rotation.

As already discussed, the other aspect that needs consideration is the probabilistic treatment for design and development of wind turbines, in order to prevent analyses and designs that are valid only at a single condition. One of the first probabilistic treatments of parameters in wind energy was performed in [27, 28] for estimating the uncertainty in wind turbine power output and annual energy production using the Weibull distribution. The uncertainty in wind direction to model wind speed was shown to be a major source of discrepancy in assessment of wind farm power output obtained from numerical simulations, when compared to experimental data-sets [29]. Monte-Carlo based approaches have been used to sample the effect of multiple parameters on the wind power output [30–32]. A reliability based design optimization of wind turbine blades under wind load uncertainty was carried out in [33], based on 249 groups of wind data to consider the variation in wind. Common UQ propagation techniques such as polynomial chaos expansions and stochastic collocation methods have also been used to propagate uncertainties in wind turbine applications [34, 35].

Most of the probabilistic studies in the field of wind turbine simulations have been based on simplified aerodynamics. More recently in [36], an aerodynamic shape optimization of wind turbine blades using a RANS-based fluid model and an adjoint method was presented, however unsteady effects were not considered due to computational limitations. An aerodynamic design optimization for a HAWT under geometric uncertainty was studied in [37] using the univariate reduced quadrature (UEQ) approach, but the aerodynamics was based on BEM and a single airfoil shape was employed for the entire length of the blade. A stochastic analysis of flow-induced instabilities due to uncertainties in fluid forces as well as structural properties was performed in [38], using a linear sta-

bility analysis and modelling the aerodynamics based on Theodorsen's theory. The effect of this randomness on the onset of instability is clearly observed, including observance of coupled-mode flutter at speeds below the designed operational speed. However, a detailed study considering high-fidelity aerodynamics and incorporating all uncertainties is required.

As already mentioned, the computational expense of high-fidelity or Navier-Stokes aeroelastic models makes uncertainty propagation intractable. As such, data-driven techniques are being increasingly explored in order to obtain reliable estimates at low costs. Calibration of simpler models (RANS, Jensen wake models) using LES data has been implemented to build physics-informed reduced order models [39, 40]. In [41], the model parameters of a simplified finite element based structural model are calibrated using Bayesian inference in order to predict the blade dynamics. Modal decomposition methods have also been applied to high fidelity simulation data in order to obtain simplified models for studying wake dynamics [42]. Dynamic mode decomposition has been used in [43] to build a reduced order model (ROM), which was then embedded in a Kalman filter to produce a time-marching algorithm. This dynamic model could also use new data to dynamically update the ROM to provide real-time estimates. Building on the data-driven approach, in this dissertation, we explore the development of aeroelastic reduced order models based on training data from high fidelity solvers and employ them to propagate uncertainties.

In view of the gaps in current practise, a high fidelity solver for a downwind configuration wind turbine is required. Once a good-enough model is achieved, a reduced order model of the computational system is required to build a cheap solver, in order to alleviate the computational requirements and to propagate the many uncertainties existing in the system cheaply. Further for parameter estimation, we use stochastic tools, in particular a Bayesian framework. This framework allows us to use experimental information (e.g. data-sets from sensors) in order to reduce the uncertainties and reconstruct the likely behaviour of the entire system. Within the scope of this approach, we are able to utilise the measurement data obtained from a downwind wind turbine experiment.

1.3. AIM OF THE DISSERTATION

The overall aim of this dissertation is:

To develop a technique to predict – with uncertainties – the dynamic behaviour of a complex aeroelastic system (such as wind turbines) undergoing instabilities or fatigue, based on unsteady RANS simulations and data recorded from the real system.

Based on the state-of-the-art in this field, it is evident that there are many significant gaps with regard to treatment of uncertainties in the design, development and characterisation of the aeroelastic behaviour of wind turbines. The Bayesian framework can be applied in this regard to utilise information available from experimental measurements. The available data, although rich in volume, is mostly limited to stable conditions. This dissertation will explore these challenges and develop methods which are general in the sense that they can be applied to any aeroelastic problem. The downwind wind turbine test case will be explored in detail, primarily because of availability of experimental data and the inherent complexity necessitating RANS solvers. Also this problem has engineering relevance and societal significance.

In order to obtain a solution, the first numerical challenge is to build an FSI model of the full wind turbine taking into account the blades, nacelle and the tower, that reproduces the experiment. The next challenge is to obtain a time-domain ROM, which is valid for varying operating conditions (aeroelastic dynamics across a wide spectrum of operating conditions) and also for varying input parameters (e.g the uncertain structure). Finally, we require a Bayesian framework in order to assimilate the information obtained from experiments into the ROM in order to provide a holistic estimate of the behaviour of the system.

1.4. NOVELTY AND APPROACH

The contribution of this dissertation is in terms of development of a technique to predict unsteady characteristics - with uncertainties - of a computationally expensive aeroelastic system - cheaply, based on limited data or information. In terms of aeroelastic simulation of wind turbines, this is among the few simulations of a complete wind turbine considering all structural components in the fluid model. To the knowledge of the author, a downwind configuration wind turbine has been considered here for the first time. The aeroelastic solver is validated by findings of the wind turbine experiment, and accurate estimates of the blade moment variation with azimuthal position is provided by the solver. For the ROM, the work utilises ideas from the domain of system identification in order to build cheap time-domain aeroelastic models. The distinguishing approach, compared to the developments in the control community in developing ROMs for aeroelastics, is in decoupling the aerodynamic and structural solvers, where the ROM is trained only to predict the aerodynamics. Finally, a framework to use this model in the Bayesian setting is proposed, in order to predict and then reduce uncertainties of the system. We successfully demonstrate the application of this methodology across multiple test cases for inviscid as well as viscous flow solvers.

For the aeroelastic simulation, a RANS-based fluid structure interaction solver is built and a sliding mesh scheme is implemented to simulate the interface conditions between the moving and stationary domains. For the experimental wind turbine system, structural components such as the blade, nacelle and tower are considered. For the ROM, a system identification based model is developed which provides a recurrence relation between input and output data of the system obtained from high fidelity simulations. This model is further parametrised based on the operating condition (e.g. Mach number in wind turbines) in order to obtain a ROM valid over the entire flow regime, which is known as a parameter varying framework used e.g. in gain scheduling. The ROM is extensively verified for aeroelastic predictions, first for deterministic conditions and then under uncertainty. For the Bayesian identification, experimental data is used to update the uncertainties, and the posteriors are sampled using a Markov Chain Monte Carlo (MCMC) algorithm.

1.5. OUTLINE

The dissertation is laid out as follows: In Chapter 2, theoretical background of aeroelastic solvers, ROMs and UQ techniques are discussed along with their mathematical framework. A brief review of the methods existing in the literature is provided. Chapter 3 details the development of the aeroelastic solver for the experimental wind turbine model. Also two other test cases: a 2-D airfoil system and the 3-D Goland wing, are discussed. In Chapter 4, development of the ROMs for the aeroelastic solver is discussed, namely a linear AutoRegressive with eXogenous (ARX)-based ROM and a linear parameter varying (LPV) model. The stability bounds of the underlying systems are obtained employing the ROMs in state-space form and they are verified with either experimental or numerical estimates. Also the ROM for predicting wind turbine blade forcing is developed. In Chapter 5, the uncertainty quantification part of the thesis is explored. The ROMs are used to propagate the uncertainties and the details about the Bayesian framework are discussed. Finally Chapter 6 concludes the dissertation with a summary of the achieved results and list of recommendations and directions for future research.

REFERENCES

- [1] M. Borg, A. Shires, and M. Collu, *Offshore floating vertical axis wind turbines, dynamics modelling state of the art. part I: Aerodynamics*, [Renewable and Sustainable Energy Reviews](#) **39**, 1214 (2014).
- [2] F. Vorpahl, M. Strobel, J. M. Jonkman, T. J. Larsen, P. Passon, and J. Nichols,

- Verification of aero-elastic offshore wind turbine design codes under IEA Wind Task XXIII*, *Wind Energy* **17**, 519 (2014).
- [3] J. Thé and H. Yu, *A critical review on the simulations of wind turbine aerodynamics focusing on hybrid RANS-LES methods*, *Energy* **138**, 257 (2017).
- [4] M. M. Hand, D. A. Simms, L. J. Fingersh, D. W. Jager, J. R. Cotrell, S. Schreck, and S. M. Larwood, *Unsteady Aerodynamics Experiment Phase VI: Wind Tunnel Test Configurations and Available Data Campaigns*, Tech. Rep. (National Renewable Energy Laboratory, 2001).
- [5] M. Carrión, R. Steijl, M. Woodgate, G. N. Barakos, X. Munduate, and S. Gomez-Iradi, *Aeroelastic analysis of wind turbines using a tightly coupled CFD-CSD method*, *Journal of Fluids and Structures* **50**, 392 (2014).
- [6] J. H. Koh and E. Y. K. Ng, *Downwind offshore wind turbines : Opportunities , trends and technical challenges*, *Renewable and Sustainable Energy Reviews* **54**, 797 (2016).
- [7] E. Ela and B. Kirby, *ERCOT Event on February 26, 2008 : Lessons Learned*, Tech. Rep. (National Renewable Energy Laboratory, 2008).
- [8] IEA ETSAP and IRENA, *Renewable Energy Integration in Power Grids*, Tech. Rep. (IRENA and IEA-ETSAP, 2015).
- [9] T. Peng, J. He, Y. Liu, A. Saxena, J. Celaya, and K. Goebel, *Fatigue damage diagnosis and prognosis using Bayesian updating*, in *54th AIAA/ASME/ASCE/AHS/ASC Structures, Structural Dynamics, and Materials Conference* (American Institute of Aeronautics and Astronautics, 2013) pp. 1–11.
- [10] H. Xiao, J. L. Wu, J. X. Wang, R. Sun, and C. J. Roy, *Quantifying and reducing model-form uncertainties in Reynolds-averaged Navier–Stokes simulations: A data-driven, physics-informed Bayesian approach*, *Journal of Computational Physics* **324**, 115 (2016).
- [11] L. Wang, X. Liu, and A. Kolios, *State of the art in the aeroelasticity of wind turbine blades: Aeroelastic modelling*, *Renewable and Sustainable Energy Reviews* **64**, 195 (2016).
- [12] S. Goómez-Iradi, R. Steijl, and G. N. Barakos, *Development and Validation of a CFD Technique for the Aerodynamic Analysis of HAWT*, *Journal of Solar Energy Engineering* **131**, 031009 (2009).

- [13] F. Zahle, N. N. Sørensen, and J. Johansen, *Wind turbine rotor-tower interaction using an incompressible overset grid method*, *Wind Energy* **12**, 594 (2009).
- [14] M.-C. Hsu, I. Akkerman, and Y. Bazilevs, *Finite element simulation of wind turbine aerodynamics: validation study using NREL Phase VI experiment*, *Wind Energy* **17**, 461 (2014).
- [15] Y. Bazilevs, A. Korobenko, X. Deng, J. Yan, M. Kinzel, and J. O. Dabiri, *Fluid-Structure Interaction Modeling of Vertical-Axis Wind Turbines*, *Journal of Applied Mechanics* **81**, 081006 (2014).
- [16] F. Balduzzi, J. Drofelnik, A. Bianchini, G. Ferrara, L. Ferrari, and M. S. Campobasso, *Darrieus wind turbine blade unsteady aerodynamics: a three-dimensional Navier-Stokes CFD assessment*, *Energy* **128**, 550 (2017).
- [17] N. N. Sørensen, J. A. Michelsen, and S. Schreck, *Navier-Stokes predictions of the NREL phase VI rotor in the NASA Ames 80 ft × 120 ft wind tunnel*, *Wind Energy* **5**, 151 (2002).
- [18] A. Le Pape and J. Lecanu, *3D Navier-Stokes computations of a stall-regulated wind turbine*, *Wind Energy* **7**, 309 (2004).
- [19] Y. Bazilevs, M.-C. Hsu, I. Akkerman, S. Wright, K. Takizawa, B. Henicke, T. Spielman, and T. E. Tezduyar, *3D simulation of wind turbine rotors at full scale. Part I: Geometry modeling and aerodynamics*, *International Journal for Numerical Methods in Fluids* **65**, 207 (2011).
- [20] A. Bechmann, N. N. Sørensen, and F. Zahle, *CFD simulations of the MEXICO rotor*, *Wind Energy* **14**, 677 (2011).
- [21] E. Lund and J. Stegmann, *On structural optimization of composite shell structures using a discrete constitutive parametrization*, *Wind Energy* **8**, 109 (2005).
- [22] Y. Bazilevs, M.-C. Hsu, J. Kiendl, and D. Benson, *A computational procedure for prebending of wind turbine blades*, *International Journal for Numerical Methods in Engineering* **89**, 323 (2012).
- [23] D. Cárdenas, A. A. Escárpita, H. Elizalde, J. J. Aguirre, H. Ahuett, P. Marzocca, and O. Probst, *Numerical validation of a finite element thin-walled beam model of a composite wind turbine blade*, *Wind Energy* **15**, 203 (2012).

- [24] Y. Bazilevs, M.-C. Hsu, J. Kiendl, R. Wüchner, and K.-U. Bletzinger, *3D simulation of wind turbine rotors at full scale. Part II: Fluid–structure interaction modeling with composite blades*, *International Journal for Numerical Methods in Fluids* **65**, 236 (2011).
- [25] M.-C. Hsu and Y. Bazilevs, *Fluid–structure interaction modeling of wind turbines: simulating the full machine*, *Computational Mechanics* **50**, 821 (2012).
- [26] D. O. Yu and O. J. Kwon, *Time-accurate aeroelastic simulations of a wind turbine in yaw and shear using a coupled CFD-CSD method*, *Journal of Physics: Conference Series* **524**, 012046 (2014).
- [27] M. A. Lackner, A. L. Rogers, and J. F. Manwell, *Uncertainty Analysis in Wind Resource Assessment and Wind Energy Production Estimation*, in *45th AIAA Aerospace Sciences Meeting and Exhibit* (2007) pp. 1–16.
- [28] M. A. Lackner, A. L. Rogers, and J. F. Manwell, *Uncertainty Analysis in MCP-Based Wind Resource Assessment and Energy Production Estimation*, *Journal of Solar Energy Engineering* **130**, 031006 (2008).
- [29] M. Gaumond, P.-E. Réthoré, S. Ott, A. Peña, A. Bechmann, and K. S. Hansen, *Evaluation of the wind direction uncertainty and its impact on wake modeling at the Horns Rev offshore wind farm*, *Wind Energy* **17**, 1169 (2014).
- [30] C. M. Engelen, *The nonlinear effect of combining uncertainties on the energy yield of an offshore wind farm*, Ph.D. thesis, Delft University of Technology (2015).
- [31] T. Jin and Z. Tian, *Uncertainty analysis for wind energy production with dynamic power curves*, in *2010 IEEE 11th International Conference on Probabilistic Methods Applied to Power Systems* (IEEE, 2010) pp. 745–750.
- [32] S.-D. Kwon, *Uncertainty analysis of wind energy potential assessment*, *Applied Energy* **87**, 856 (2010).
- [33] W. Hu, K. K. Choi, and H. Cho, *Reliability-based design optimization of wind turbine blades for fatigue life under dynamic wind load uncertainty*, *Structural and Multidisciplinary Optimization* **54**, 953 (2016).
- [34] J. P. Murcia, P. E. Réthoré, A. Natarajan, and J. D. Sørensen, *How Many Model Evaluations Are Required To Predict The AEP Of A Wind Power Plant?* *Journal of Physics: Conference Series* **625**, 012030 (2015).

- [35] J. M. Rinker, *Calculating the sensitivity of wind turbine loads to wind inputs using response surfaces*, *Journal of Physics: Conference Series* **753**, 032057 (2016).
- [36] T. Dhert, T. Ashuri, and J. R. R. A. Martins, *Aerodynamic shape optimization of wind turbine blades using a Reynolds-averaged Navier-Stokes model and an adjoint method*, *Wind Energy* **20**, 909 (2017).
- [37] M. S. Campobasso, E. Minisci, and M. Caboni, *Aerodynamic design optimization of wind turbine rotors under geometric uncertainty*, *Wind Energy* **19**, 51 (2016).
- [38] P. Pourazarm, L. Caracoglia, M. Lackner, and Y. Modarres-Sadeghi, *Stochastic analysis of flow-induced dynamic instabilities of wind turbine blades*, *Journal of Wind Engineering and Industrial Aerodynamics* **137**, 37 (2015).
- [39] P. M. Gebraad, F. W. Teeuwisse, J. W. van Wingerden, P. A. Fleming, S. D. Ruben, J. R. Marden, and L. Y. Pao, *A data-driven model for wind plant power optimization by yaw control*, in *Proceedings of the American Control Conference* (2014) pp. 3128–3134.
- [40] G. V. Iungo, F. Viola, U. Ciri, M. A. Rotea, and S. Leonardi, *Data-driven RANS for simulations of large wind farms*, *Journal of Physics: Conference Series* **625**, 012025 (2015).
- [41] K. L. Van Buren, M. G. Mollineaux, F. M. Hemez, and S. Atamturktur, *Simulating the dynamics of wind turbine blades: part II, model validation and uncertainty quantification*, *Wind Energy* **16**, 741 (2013).
- [42] D. Foti, *Quantification and reduction of uncertainty of model predictions of wind turbines and plants via high-fidelity simulations*, Ph.D. thesis, University of Minnesota (2016).
- [43] G. V. Iungo, C. Santoni-Ortiz, M. Abkar, F. Porté-Agel, M. A. Rotea, and S. Leonardi, *Data-driven Reduced Order Model for prediction of wind turbine wakes*, *Journal of Physics: Conference Series* **625**, 012009 (2015).

2

BACKGROUND - AEROELASTICITY AND UNCERTAINTY

Throughout this dissertation, three scientific domains are explored: aeroelasticity, reduced order modelling and uncertainty quantification. In this chapter, a brief overview of the theoretical and mathematical background of these domains is presented. Only the theory relevant to this dissertation is provided; further details can be accessed from the references. Section 2.1 outlines the mathematical framework of the fluid and structural solvers for development of the aeroelastic model, along with a discussion of the common instabilities occurring in such systems. In Section 2.2, instabilities occurring in aircraft and wind turbines are discussed. In Section 2.3, a review of different reduced-order models that have been applied to aeroelastic predictions is provided. Finally, uncertainty quantification methods along with basic theory on Bayesian data assimilation is discussed in Section 2.4.

2.1. AEROELASTICITY

Aeroelasticity is a physical phenomena arising out of mutual interaction of inertial, elastic and aerodynamic forces [1]. This interaction can lead to instabilities in aeroelastic systems, and safe operating regimes of aircraft in terms of parameters such as altitude and Mach number, have to be obtained during design. Aeroelastic behaviour is schematically depicted through the Collar triangle [2], shown in Figure 2.1, where a linear instability known as flutter is shown. The three types of forces are represented by the three vertices of the triangle, so called as the ‘triangle of forces’. The instabilities occur as a result of the interaction of these forces and flutter is influenced by all the three types of forces and hence it is

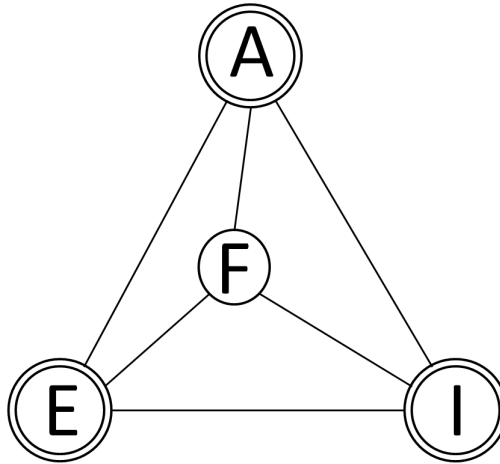


Figure 2.1: Collar triangle depicting aeroelastic interactions [2]; A: aerodynamic forces, E: elastic forces, I: inertial forces, F: flutter.

positioned within this triangle. Other forms of instability, such as control reversal, lie outside the triangle, since they do not involve inertial forces. The reader is referred to [2] for further details. Flutter occurs as a result of unfavourable coupling of modes and is observed in bridges, aircraft wings and wind turbines.

In order to predict instabilities such as flutter, both experimental as well as numerical methods exist. However, experiments are generally very expensive and also potentially dangerous, in case of flutter. In practise, it is convenient to estimate the instability limits numerically and then perform verification experiments for a reduced and non-destructive set of operating conditions. Robust aeroelastic solvers are required in order to provide reliable predictions. In the computational setting, these solvers generally involve coupling of separate fluid and structural solvers. A brief theoretical discussion of the governing equations is provided here.

2.1.1. NAVIER-STOKES EQUATIONS

The dynamics of a fluid are described by the Navier-Stokes equations, independently derived by Claude-Louis Navier in 1822 and George Gabriel Stokes in 1845. The flow equations are derived based on the conservation of three quantities - mass, momentum and energy in fluid parcels, which lead to the continuity, momentum and energy equations respectively. For a compressible fluid with veloc-

ity $\mathbf{u}(x, t)$ and density $\rho(x, t)$ in a domain $\Omega \subset \mathbb{R}^3$, they are given by:

$$\partial_t(\rho) + \operatorname{div}(\rho \mathbf{u}) = 0 \quad (2.1a)$$

$$\partial_t(\rho \mathbf{u}) + \operatorname{div}(\rho \mathbf{u} \otimes \mathbf{u}) + \nabla p = \rho \mathbf{f} + \operatorname{div} \mathcal{S}(\mathbf{u}) \quad (2.1b)$$

$$\partial_t E + \operatorname{div}((E + p)\mathbf{u}) = \operatorname{div}(\mathcal{S}(\mathbf{u})\mathbf{u}) + \operatorname{div}(\kappa \nabla \vartheta) + (\rho \mathbf{f}) \cdot \mathbf{u} + \rho Q, \quad (2.1c)$$

where \mathbf{f} is a body forcing term such as gravity, Q is the intensity of the external energy flux and \mathcal{S} is the viscous stress tensor. E is the energy density, κ is the heat conduction coefficient, while p and ϑ are the pressure and temperature of the fluid respectively. A detailed derivation of these equations can be found in e.g. [3].

In many flows of interest and for the test-cases to be investigated in this dissertation, turbulent flow conditions must be simulated. The numerical solution of (2.1) can be performed by employing different modelling techniques: with Direct Numerical Simulation (DNS) where all scales of turbulence are resolved; or using Large Eddy Simulation (LES) where only large scales are resolved, and a filter is used to remove the smallest scales, which are then typically modelled with a subgrid-scale model; or using the Reynolds-averaged Navier-Stokes (RANS) equations, which are obtained by time-averaging the governing equations. DNS results are accurate, but computational costs scale by Re^3 , where Re is the Reynolds number and is mostly computationally intractable for engineering problems. LES is being increasingly used with the growth in computing power, however it is also impractically expensive for many industrial problems, especially when uncertainty quantification is needed. The RANS equations are by far the most commonly used due to the acceptable accuracy for many interesting flows and relatively cheap computational costs. RANS equations are derived by the Reynolds decomposition, while for the compressible case, a density weighted time-averaging is performed known as Favre decomposition. An instantaneous flow variable ϕ is decomposed into a mean $\tilde{\phi}$ and fluctuating component ϕ'' as given by:

$$\phi = \tilde{\phi} + \phi''. \quad (2.2)$$

Favre averaging leads to:

$$\overline{\rho \phi} = \overline{\rho(\tilde{\phi} + \phi'')} = \overline{\rho} \tilde{\phi}, \quad (2.3)$$

where $\overline{\rho \phi''} = 0$. Following the decomposition and averaging, the Navier-Stokes equations are reduced to Reynolds-averaged-Navier-Stokes (technically, Favre-averaged) equations: a detailed derivation can be found in e.g. [4]. Averaging results in almost identical equations with additional terms, notably $\tau_{ij} = -\rho u_i'' u_j''$,

known as the Reynolds stresses, which need to be approximated with a turbulence model to close the system of the RANS equations. This tensor is commonly modelled with the use of so-called eddy-viscosity models, which originate from a hypothesis provided by Boussinesq in 1877 [5]. The hypothesis assumes that τ_{ij} is proportional to the mean strain rate tensor S_{ij} , which can be written as:

$$\tau_{ij} = 2\mu_t S_{ij} - \frac{2}{3}\rho k \delta_{ij}, \quad (2.4)$$

where, μ_t is the eddy viscosity and δ_{ij} is the Kronecker delta. Here k is the turbulent kinetic energy, which is used as a transported variable in the turbulence models. Two-equation models are most commonly used, in which case k is the one of the variables. The other transported variable depends on the turbulence model being used and could be the rate of dissipation of turbulence energy, ϵ or the specific dissipation rate, ω leading to $k - \epsilon$ and $k - \omega$ models. Accuracy of different turbulence models depends on the specific flow conditions existing in the test cases.

In this dissertation, unsteady flows are investigated for rotating bodies - downwind wind turbines. For time-dependent flows, unsteady RANS (URANS) equations are employed, where time derivatives in the governing equations are retained and the time-stepping should be sufficient to capture the unsteady effects, e.g. vortex shedding frequency can be used as a measure for minimum time-step employed. URANS requires separation between unsteady time-scales and turbulent time-scales. Moreover, for rotating bodies such as wind turbines, the flow equations must be described in the rotating frame of reference. If \mathbf{v} is the velocity field relative to the system rotating at angular velocity ω and position vector \mathbf{r} from the axis of rotation, the velocity field in the absolute frame of reference is given by:

$$\mathbf{u} = \mathbf{v} + \omega \times \mathbf{r}. \quad (2.5)$$

The equations are expressed in the rotating frame of reference. The entrainment velocity $\omega \times \mathbf{r}$ does not add mass to the system, hence the continuity equation is unchanged:

$$\partial_t(\rho) + \text{div}(\rho\mathbf{v}) = 0. \quad (2.6)$$

However, for the momentum equations, two terms representing the Coriolis forces per unit mass \mathbf{F}_{co} and the centrifugal force \mathbf{F}_{ce} are to be added, which are given by:

$$\mathbf{F}_{co} = -2\omega \times \mathbf{v} \quad \mathbf{F}_{ce} = -\omega \times (\omega \times \mathbf{r}). \quad (2.7)$$

The momentum conservation equation then becomes:

$$\partial_t(\rho\mathbf{v}) + \text{div}(\rho\mathbf{v} \otimes \mathbf{v}) + \nabla p = \rho\mathbf{f} - 2\rho(\omega \times \mathbf{v}) - \rho\omega \times (\omega \times \mathbf{r}) + \text{div}\mathcal{S}(\mathbf{v}). \quad (2.8)$$

For the energy conservation, the work done by the centrifugal force is added to the energy equation, which results in:

$$\partial_t E_v + \text{div}((E_v + p)\mathbf{v}) = \text{div}(\mathcal{L}(\mathbf{v})\mathbf{v}) + \text{div}(\kappa\nabla\vartheta) + (\rho\mathbf{f}) \cdot \mathbf{v} + \rho Q, \quad (2.9)$$

where energy density E_v is now defined in the rotating frame of reference.

2.1.2. STRUCTURAL EQUATIONS - VIBRATION THEORY

Structural analysis is required in order to predict the dynamic behaviour of the system under external loading. The dynamics of the structure are analysed based on the theory of vibration under free or forced loading condition. Free vibration is the natural response of a system due to an initial disturbance, resulting in vibration of the system in its natural frequencies. Under forced vibration, the system is subjected to an external loading, which can be periodic, transient or random.

Vibrating systems are also classified based on their linear or nonlinear behaviour. The classification can be based on the nature of the governing differential equation, but typically, it is governed by the range of operation of the system. For example, in case of a pendulum with an amplitude θ , the restoring torque is proportional to $\sin\theta$, where for small amplitudes, $\sin\theta \approx \theta$, while for large amplitudes, this reduction is not possible. In the context of this dissertation, linear stability analysis is of interest, hence structural nonlinearity is not explored due to the assumption of small deformations of the structure. However for limit-cycle oscillations, large deformations are possible, but in the context of this research, only aerodynamic nonlinearities are considered, which will be justified in subsequent chapters. The reader is referred to [6] and [7] for further details about structural analysis for both linear and nonlinear systems.

The governing equations can be typically represented in the form:

$$M\ddot{\mathbf{u}}(x, t) + K\mathbf{u}(x, t) = \mathbf{F}_s(x, t), \quad (2.10)$$

where \mathbf{u} is the displacement of the system and \mathbf{F}_s is the external loading, while M and K are the mass and stiffness matrices. In the absence of analytical solutions, the response of the structure is estimated computationally, where various discretisations of the governing equations are possible, such as the finite difference or finite element method. The numerical techniques involve discretisation of the system into elements and formation of elemental M and K matrices. Equation (2.10) is analogous to that of a spring-mass system and the problems discussed in this dissertation (for example, wind turbine blade) can all be reduced to this form. Additionally a damping term is used for some problems, which will be discussed in more detail in Section 4.5.

Under the assumption of a linear system, the mass and stiffness matrices in (2.10) are constant under any dynamic load \mathbf{F}_s , and then a modal form can be used. For deriving the modal form of equations of motion, the natural modes of the system $\mathbf{X}_i(x)$ are determined. The deformation of the system is then defined by:

$$\mathbf{u}(x, t) = \sum_{i=1}^{\infty} f_i(t) \mathbf{X}_i(x), \quad (2.11)$$

where $f_i(t)$ are the modal amplitudes, which are functions of time. In the context of the reduced-order model developed in this dissertation, these modal amplitudes are utilised for temporal updating of the structure, while keeping the original modes of the system unchanged, which will be explained in more detail later. In the dynamic modal equation, the first $N \ll m$ modes are considered, where m is the (finite) number of degrees of freedom of the system after discretisation. These N modes are selected such that they approximately represent the dynamic behaviour of the system by containing most of the energy. The mode shapes $\mathbf{X}_i(x)$ are determined by solving an eigenvalue problem and they are generally orthogonal. The mode shapes can be scaled in various ways - commonly mass normalisation is performed in modal analysis such that:

$$\mathbf{X}_i^T \mathbf{M} \mathbf{X}_j = \delta_{ij}, \quad (2.12)$$

where δ_{ij} is a delta function. Substitution of (2.11) into (2.10) and multiplication of resulting equation by \mathbf{X}_j^T gives:

$$\sum_{i=1}^N \mathbf{X}_j(x) \mathbf{M} \mathbf{X}_i(x) \ddot{f}_i(t) + \sum_{i=1}^N \mathbf{X}_j(x) \mathbf{K} \mathbf{X}_i(x) f_i(t) = \mathbf{X}_j(x) \mathbf{F}_s(x, t). \quad (2.13)$$

Due to (2.12), (2.13) is reduced to N decoupled modal equations given by:

$$\ddot{f}_i(t) + \omega_i^2 f_i(t) = F_q(t), \quad i = 1, \dots, N, \quad (2.14)$$

where $F_q(t)$ is the modal force and ω_i^2 are the modal frequencies of the system. The system of equations (2.14) are uncoupled and each of these differential equations can be solved independently. Further details about incorporation of non-uniform material properties in this framework with a 1-D finite difference model will be discussed in Section 3.1.3, where an additional term for rotating wind turbine blade will be introduced in the governing equations.

2.1.3. AEROELASTIC SOLVER

Numerical estimation of aeroelasticity involves coupling of CFD and structural dynamics equations. Broadly speaking, there are two methods for solving the

coupled FSI problem - the monolithic and partitioned approaches. In the monolithic approach, both fluid and structural equations are solved simultaneously at each time-step, requiring a reformulation of the governing equations. As such, the monolithic approach is intrusive, since redevelopment of numerical code of the system is required. In the partitioned approach, the fluid and structural equations are solved independently, and the two solvers are coupled by exchanging information at the interface. The distinct solvers allow the use of customised iterative methods for the fluid and structural equations, however development of stable and robust coupling techniques at the interface requires special consideration.

At the interface, the structural mesh displacements are transferred onto the fluid mesh, while the fluid loads are transformed into equivalent structural loads. Typically, the fluid and structural grids differ in resolution and hence the meshes will be non-conforming at the interface. The structural model usually is relatively simple and is often represented by a geometries such as plate, 1-D beam or box. Hence it is computationally cheap due to lower number of degrees-of-freedom and requires few operations if linearity is assumed. On the other hand, the fluid model requires more resolution, for example a wind turbine model would have the blade surface as the interface, which normally requires very fine resolution in order to estimate the blade loads accurately, e.g. in the wind turbine blade considered in this dissertation, each blade has ~ 18000 mesh nodes, which is much higher than the structural mesh. Due to this non-conformity, interpolation techniques involving projection or extrapolation are required. This is typically achieved by construction of a transformation operator; a discussion on the existing techniques can be found in [8, 9].

The complexity of the aeroelastic model is an important consideration in order to obtain realisable models in terms of computational expense. It is common practise in aeroelasticity to replace the structural model with a modal solver, as introduced in the previous section. The computational challenge in the aeroelastic model arises entirely due to the fluid solver. To alleviate the computational challenge, time-linearised models have been developed, which are based on the principle of obtaining a steady-flow field known as the base-flow, about which small perturbations are considered for estimating the dynamic behaviour. For mathematical simplicity, only linear terms in the perturbation analysis are included in the final model and as such these class of models are known as time-linearised. For the base flow, fully nonlinear steady-state solutions of the Navier-Stokes equations are obtained. The steady flow solution hence has a spatial structure and can also include complex features such as shock waves, if present. The linear perturbation for the dynamic solution thus assumes that the shock wave or other flow quantities vary *linearly* about this nonlinear field. Time-

linearisation reduces computational costs significantly and is also sufficient to estimate interesting flow features.

Typically, industrial designers perform optimisation of the structural model parameters, in which case the full nonlinear model is computationally expensive. As a result, time-linearisation is employed extensively both for research and industrial practise. The time-linearised model also provides a framework for incorporating reduced order models in the aeroelastic solver. This idea is however limited to steady base flows. It has been employed for the test cases of airfoil and Goland wing in this dissertation and a detailed discussion will follow in the subsequent chapters.

To develop a mathematical notation for coupled solvers, the equations can be written on the basis of aeroelastic operators, for details see [10]. In aeroelasticity, displacements and forces are commonly expressed in a generalised form. The relationship between generalised force F_q and displacement u_q can be written as:

$$F_q = \mathcal{L}(u_q), \quad (2.15)$$

where \mathcal{L} is the structural operator. The inverse of \mathcal{L} is assumed to exist and can also be represented in a functional form as:

$$u_q = \mathcal{L}^{-1}(F_q). \quad (2.16)$$

As introduced in Figure 2.1, forces in aeroelastic systems could be aerodynamic F_{Aq} , inertial F_{Iq} or elastic F_{Eq} . Combination of these forces lead to different aeroelastic instabilities, and (2.15) can be decomposed as:

$$F_{Aq} + F_{Iq} + F_{Eq} = \mathcal{L}(u_q). \quad (2.17)$$

Elastic forces depend on the material properties of the structure and hence can be estimated from the structural characterisation alone. The aerodynamic forces F_{Aq} change with the movement of the structure and conversely, the orientation of the structure changes due to the aerodynamic forcing. This mutual interaction can be represented by:

$$F_{Aq} = \mathcal{A}(u_q) \quad u_q = \mathcal{A}^{-1}(F_{Aq}) \quad (2.18)$$

where \mathcal{A} is the aerodynamic operator. In dynamic aeroelasticity, inertial forces arise as a result of the change in displacement, which can be expressed with the inertial operator \mathcal{I} as:

$$F_{Iq} = \mathcal{I}(u_q) \quad u_q = \mathcal{I}^{-1}(F_{Iq}). \quad (2.19)$$

(2.18) and (2.19) can be substituted in (2.17) to give:

$$\mathcal{A}(u_q) + \mathcal{J}(u_q) + F_{Eq} = \mathcal{L}(u_q), \quad (2.20)$$

which gives the generalised displacement as:

$$u_q = \mathcal{L}^{-1}(\mathcal{A}(u_q) + \mathcal{J}(u_q) + F_{Eq}). \quad (2.21)$$

Equations (2.20) and (2.21) provide the interaction between the fluid and structure in aeroelastic problems. The operators could be linear or nonlinear, as was discussed in the earlier section. The mutual interaction of these forces results in different instabilities; a few of these are discussed in the next section.

2.2. INSTABILITIES IN AEROELASTICITY

Aeroelastic instabilities can be broadly classified as static or dynamic. A brief discussion on some instabilities is provided here.

2.2.1. FLIGHT INSTABILITIES

Divergence is a static aeroelastic phenomena, that occurs when the twisting moment of a structure is unable to sustain the moment generated by the aerodynamic lifting force. At speeds below the *divergence speed*, a static equilibrium is reached, hence this limit has to be characterised for aeroelastic structures.

Control surface reversal is the condition when the trailing-edge control surface of an aircraft becomes ineffective due to excessive elastic twist of the wing. The condition results in a zero or negative lift or roll rate at large ratio of dynamic pressure to the stiffness of wing.

Flutter is a dynamic instability, which is one of the most important aeroelastic phenomena investigated for avoiding catastrophic events. It is a self-excited oscillation in which the structure extracts energy from the fluid. There are various forms of flutter: Classical binary flutter occurs out of unfavourable coupling of two modes from the associated aerodynamic forces. It can however also occur by coupling of multiple modes. Flutter is characterised by a flutter speed and for an entire flight regime, a flutter boundary is defined, which separates the stable and unstable regimes. For systems assumed to be linear, the oscillations damp out below the flutter speed, sustain at the interface and grow above the flutter point.

For nonlinear systems, the diverging oscillations are bounded due to the nonlinearity of the system and sustained oscillations of potentially large amplitude are maintained, which are known as *Limit Cycle Oscillations* (LCO). These oscillations can lead to significant reduction in aircraft performance, increase in

airframe fatigue and also cause discomfort to the passengers in a commercial aircraft.

In this dissertation, we will be exploring and predicting the phenomena of flutter more extensively.

2

2.2.2. WIND TURBINE AEROELASTIC FAILURE

Wind turbines are increasingly prone to instabilities and fatigue with growing size and flexibility of blades. A review of instabilities in helicopters and wind turbines can be found in [11, 12]. The instabilities can occur in blades from single or multiple degrees of freedom or due to rotor-tower interaction.

Blade edgewise or flapwise vibrations have been reported [13, 14] in stall-regulated turbines, and are experienced more often in larger blades. These vibrations are caused by negative damping of edgewise or flapwise mode and the shape of the eigenmode has a strong influence on this instability. Further extensive details about examples of such instabilities in wind turbines can be found in [12].

Stall flutter, also known as stall-induced vibration may occur in wind turbines operating under stall or in separated flow conditions [13, 15]. These vibrations are characterised by the blade airfoil characteristics, effective direction of blade vibration and damping. The mechanism for these vibrations in the dynamic case is based on the effective reduction in lift at high angles of attack, and then a subsequent reduction in the torsional deformation of the blade (if aerodynamic centre is in front of centre of twist) due to smaller forces, which in turn reduces the angle of attack. The smaller angle of attack again results in an increase in lift, which eventually results in a limit-cycle instability.

The other form of instability is *classical flutter*, which can be related to pitch-regulated wind turbines. This form of instability arises out of coupling of modes and is identified with different names depending on the participating modes. For example, the torsional and flapping modes may couple unfavourably through the aerodynamic forces with a negative damping. Besides other conditions, this instability can arise due to low frequency ratio between the flapping and torsional modes, high rotor speed, low stiffness and for centre of mass being close to the aft of the blade cross section [16, 17].

Fatigue is another failure phenomena that has to be investigated in order to correctly assess the unique load spectrum during the design of wind turbines [18]. The spectrum of fatigue loads is characterised by the operating conditions of the turbine. Further details on the theory of fatigue can be found in [18]. Other instabilities can arise out of coupling of tower and rotor modes. *Lead-lag and Sideways Tower Instability* and *Whirl Flutter* are few examples, further details can be found in [12].

2.3. REDUCED ORDER MODELLING IN AEROELASTICITY

Application of aeroelasticity for industrial applications has been largely impaired due to the computational expense of the underlying system [19]. As such, Reduced Order Models (ROMs) have been emerging as a useful alternative for both the academic community as well as for industry. The ROMs can be broadly divided into projection-based and system identification-based. The reader is referred to [1] for a detailed review of the ROMs that have been used in fluid-structure interaction applications. A short discussion on a few particularly relevant ROMs is provided here.

One technique for model reduction is the *Harmonic balance method* [20, 21], which can be applied to time-periodic problems to determine the stability characteristics of dynamical systems. In this method, the unsteady solution is represented by a Fourier series in time domain, for example, density ρ is expressed as:

$$\rho(x, t) \simeq \sum_n G_n(x) \exp(i\omega n t), \quad (2.22)$$

where only the first few of the n harmonics are retained. (2.22) is substituted into the governing equations, which are solved for the Fourier coefficients G_n . In the absence of a priori knowledge of the fundamental frequency ω of the system, the frequency also needs to be estimated [22]. Use of single harmonics [23] has been shown to be sufficient for capturing instabilities in airfoils, while in [21], multiple harmonics are considered for application to turbo-machinery flows. More recently, a high-order formulation with the Euler equations has been applied for nonlinear aeroelasticity [24].

Projection-based methods have been used extensively for building ROMs, using various techniques such as the balanced truncation method [25], classical model truncation, Krylov subspaces [26], or bases obtained from snapshots [27] and Proper Orthogonal Decomposition (POD) [28, 29]. The latter method, *POD* is based on expansions obtained from bases $\phi_j : j = 1, 2, \dots, m$, also known as Karhunen-Loeve (KL) basis, constructed from snapshots $\mathbf{q}^r : r = 1, 2, \dots, n$ which are essentially multiple (n) instantaneous flow fields. The POD basis ϕ_j is a reduced set of vectors ($m \ll n$), which is the best linear basis to represent the flow field (in a least-squares sense), and they are obtained by solving an eigenvalue problem. Thus, the idea is representation of flow field as a small set of modes, and in turn reduce the degrees of freedom of the system. The magnitude of the eigenvalues attached to the modes is used to choose a sufficient number of POD modes to represent the flow accurately. The solution estimate from the POD can be written as:

$$\mathbf{u}(x, t) \simeq \sum_{j=1}^m c_j(t) \phi_j(x), \quad (2.23)$$

where $c_j(t)$ is the magnitude attached to the mode, and is the temporal term in the equation. POD was initially applied in fluid dynamics to study turbulence properties, in particular to study the coherent turbulent structures in experimental data. POD has since been used in many aeroelastic applications, including prediction of limit-cycle oscillations [30]. However, POD modes are not necessarily optimal for time-evolved or dynamic data. This has seen the development of *Dynamic Mode Decomposition* (DMD) [31, 32] to analyse the temporal dynamics of nonlinearly evolving flows.

The other class of ROMs are based on system identification. One of them is *Volterra* theory-based ROM. They have been applied to Euler and Navier-Stokes models of linear and nonlinear aeroelastic systems [33–35]. The model is based on construction of Volterra kernels identified from aerodynamic impulse responses. Thereafter, a convolution scheme is employed to create linear and nonlinear aerodynamic responses to arbitrary inputs. For a time-invariant, nonlinear system subjected to an arbitrary input $u(t)$, the system response obtained from Volterra theory is given by:

$$y(t) = h_0 + \sum_{\tau=0}^N h_1(t-\tau)u(\tau) + \sum_{\tau_1=0}^N \sum_{\tau_2=0}^N h_2(t-\tau_1, t-\tau_2)u(\tau_1)u(\tau_2) + \sum_{\tau_1=0}^N \cdots \sum_{\tau_n=0}^N h_t(t-\tau_1, \dots, t-\tau_t)u(\tau_1)\dots u(\tau_t), \quad (2.24)$$

where h_0 is the steady state term satisfying the initial condition, h_1 is the first-order kernel or the linear impulse response and h_t are the higher order kernels, which are impulse responses obtained at t number of time instances. The number of kernels retained in the model determines the complexity of the model, with inclusion of only the first kernel h_1 implying assumption of linearity, while full nonlinear behaviour can be retained if all kernels are considered. High order Volterra kernels are however expensive to compute since they are multi-dimensional convolution integrals, hence most of the applications are limited to lower-order kernels.

Another class of system identification-based ROMs are the *input/output models*, which are data-driven ROMs and are non-intrusive in nature. As mentioned in case of time-linearised models, the idea of a base nonlinear model as a steady-state solution is implemented in these models. The ROM thus provides the dynamic response of the system only. These methods are based on the generation of training data in order to identify a mapping function between the input and output. Both linear and nonlinear functions can be developed for predicting aeroelastic responses. One example of this class of models is the eigensystem realisation algorithm (ERA) employed by [35] to predict flutter, through models in

state-space form using modal impulse responses. A discrete time-domain linear ROM based on an autoregressive-moving-average (ARMA) model was proposed by [36] for aerodynamic estimations. Among others, a discrete-time state space model was used by [37] for modelling unsteady aerodynamics. Also, ROMs based on ARX model have been implemented to predict flutter [38], flutter suppression [39] and for aeroservoelastic analysis [40]. There have been developments in order to generalise such ROMs with a parameter-varying framework for applications in aerospace [41] and wind energy [42, 43] among others.

There have been many contributions towards building LPV models, particularly in the control community. LPV models originated from the idea of gain scheduling, where local linear control systems are interpolated to obtain a global solution in the entire operating regime [44]. The operating regime can be characterised by one or multiple *scheduling parameters*, depending on the dynamical system. LPV system can be represented in the input-output (IO) or a state-space (SS) form. Depending on the representation, the approaches for identification of the LPV system can be classified based on LPV-IO or LPV-SS models. In case of LPV-IO models, this could be based on interpolation [45], regression [46], set membership [47] or nonlinear optimisation [48]. While for LPV-SS models, some of the identification methods are based on gradient [49], multiple-model [50], full-measurement [51], set-membership [52] and subspace [53] approaches. The reader is referred to [54] for a detailed review of these methods.

The subspace-based approaches are advantageous in the sense that an interpolation or identification of local models is not required. During estimation, a generalised data equation of the LPV-SS model is obtained to estimate the state and state-matrices. An overview of closed-loop subspace-methods can be found in [55]. A global predictor based subspace identification algorithm for an LPV system is presented in [56, 57] for both closed-loop and open-loop systems. However this method suffers from the curse of dimensionality, the size of the state matrices increase exponentially with the dimension of the past window. To circumvent this, a kernel-based regularisation approach is proposed by the authors. It was observed that the length of the past-window influences a trade-off between bias and variance of the estimates, and hence, a smaller past window is preferable. In terms of flutter prediction, global and local identification techniques have been compared for a two degree-of-freedom airfoil assuming steady aerodynamics in [58], which showed a trade-off between bias and variance in different methods. More recently, a nuclear norm based recursive subspace identification method has been developed for flutter detection of a scaled upwind wind turbine [59]. The method is demonstrated to track the system behaviour accurately for slowly varying dynamics of the experimental turbine that is investigated, but it is observed that the method may not be optimal for highly nonlin-

ear systems due to higher computational complexity.

In this dissertation, considering the applicability of the LPV framework for varying operating conditions, it is implemented for prediction of aeroelastic characteristics such as instabilities or fatigue, and they will be discussed in further detail in Chapter 4. Contrary to the identification approaches commonly implemented in the control community, the aerodynamic and structural solvers are decoupled during training and a decoupled LPV-ARX model is obtained only for estimating the aerodynamics. This framework enables consideration of structural uncertainties without modifying the fluid model. For obtaining the model, decoupled ARX models are initially constructed at different operating conditions, and coefficient interpolation is performed. In view of the conciseness in notation, these decoupled models would be referred as ARX and LPV-ARX models in this dissertation, as they are known in the research community. In the current investigation, the scheduling parameter remains constant during each experiment or when individual LTI models are identified. The stability of the resulting LPV system is defined in a frozen sense, which is discussed in further detail in Section 4.2. In future investigations, the identification approach could be modified to incorporate other global methods such as the subspace approach, however owing to the higher complexity in the latter case, the interpolation approach is chosen here.

All the aforementioned models can be used for predicting linear dynamic responses such as flutter. However nonlinear dynamics may arise in aeroelastic systems out of large amplitude deformations or nonlinear movement of shock waves, leading to phenomena such as LCO. Prediction of such dynamics requires training of models with nonlinear architecture. Multiple strategies have been employed in order to identify the nonlinear network mapping the inputs to the outputs. One of the most frequently used techniques for identifying nonlinear terms are Neural Networks (NN). A neural network is basically an interconnection of weighted nodes for mapping inputs to outputs. A node sums the weighted inputs and passes it to the next layer. There may be many layers of nodes, referred to as hidden layers, and the intermediate connections may result in very complex networks, which are generally treated as a black-box by the user. In terms of use of neural networks in fluid mechanics, a recurrent-multi-layer-perceptron neural network was proposed by [60] to identify aerodynamic coefficients. Further, a radial-basis-function neural network (RBF-NN) was employed by [61] in order to analyse LCO with large shock motion in transonic flow. Other aeroelastic applications include use of Discrete-Time-Recurrent NN (DTRNN), Nonlinear-ARX (NARX) NN [62] and Continuous-Time-Recurrent NN (CTRNN) [63] models.

The NN approach with an implicit nonlinear function can introduce difficul-

ties in estimation of the linear stability point. Instead, the nonlinear model can be formulated such that the system response can be computed as a summation of a linear and a nonlinear part. In the case of aeroelastic stability prediction, the linear part can be used to predict the flutter point, while the nonlinear part can provide the LCO amplitude and response. In [64], this methodology has been applied using a Levenberg-Marquardt (LM) algorithm for identifying the nonlinear coefficients in the model. The method is more physically intuitive compared to a fully nonlinear approach and also lead to generation of ROMs in a shorter time, with good level of accuracy [64]. Other developments in this approach include use of a Polynomial Nonlinear State Space (PNLSS) model, proposed in [65] and successfully applied to two physical systems. PNLSS is also based on the estimation of the system state based on sum of linear and nonlinear terms in a state-space framework. The nonlinear functions are chosen from a family of monomials upto a certain degree with all distinct combinations. This approach could provide a mathematical understanding in the final optimised model. In aeroelasticity, PNLSS has been applied to perform nonlinear model reduction [66], by choosing the monomials based on a iterative, greedy algorithm. All these methods involve an extensive training procedure, which can significantly affect the quality of predictions.

2.4. UNCERTAINTIES IN AEROELASTICITY

UQ and aeroelasticity are significantly mature domains in terms of scientific developments within their respective communities. However literature is scarce when the two disciplines are considered together. In the regulatory communities such as aircraft certification, aeroelasticity has been treated deterministically until now. Among others, the reasons for non-incorporation could be the high computational costs for aeroelastic systems and large number of unknown structural parameters that might need to be considered as stochastic. Notwithstanding these difficulties, the opportunities for coupling the two disciplines are multitudinous, with the development of efficient UQ techniques, ROMs for estimating aeroelastic behaviour and also availability of computing resources. The primary facets of UQ are discussed here.

UQ is the study of behaviour of systems under uncertainties. Uncertainty can represent unknown parameters affecting the system dynamics, the inherent uncertainty in a physical process, modelling discrepancies and assumptions and many more. The theoretical foundation of UQ is in probability and statistics, but application connects strongly to disciplines of numerical analysis such as optimization and simulation, model reduction. Initial developments were mostly confined to the mathematical community, but subsequently, there have been applications in other disciplines [67, 68] with dedicated literature emerging for UQ

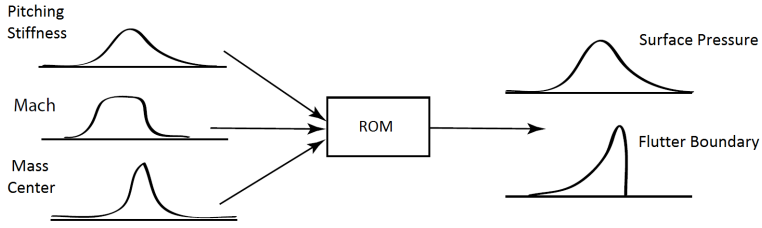


Figure 2.2: Uncertainty propagation, representative parameters from a problem in fluid mechanics.

[69, 70], in addition to journals for UQ.

Uncertainties are broadly classified into two categories: *aleatoric* and *epistemic*. Aleatoric uncertainty is an irreducible form of uncertainty that arises from natural random variations of a process. For example, the outcome of a flip of a coin is an aleatoric uncertainty, since more data or improved models cannot increase our knowledge about the outcome as it is part of the natural process of the system. On the other hand, epistemic uncertainty arises from lack of knowledge about the process, e.g. about the value of an input parameter. This uncertainty is reducible, e.g. by measuring some aspect of the system, the uncertainty in the parameter can be updated. In this dissertation, epistemic uncertainty is investigated and reduced in a Bayesian framework, where these uncertainties are represented in the probability framework.

UQ can also be categorised into two types - forward uncertainty propagation and inverse uncertainty quantification. In the forward problem, known probability distributions of uncertain input parameters are propagated through the simulation code to ascertain their effect on the output quantities, specifically to provide probabilistic estimates of the quantities of interest in terms of distribution or statistical moments. This process is shown in Figure 2.2, where the uncertain input parameters such as stiffness and Mach number are propagated through the CFD model to obtain stochastic estimates of quantities of interest such as surface pressure on the wing. On the other hand, the inverse UQ framework involves updating probability distribution of input parameters given measurement data (can be experimental or from high fidelity simulations) of the output. This process, also known as calibration, can be used to reduce uncertainties in the input parameters, which in turn can again be employed in the forward problem to provide *informed* predictions.

2.4.1. UNCERTAINTY PROPAGATION

In forward propagation, sensitivity analysis is a useful mathematical tool in order to determine a subset of input parameters that primarily influence the output quantity. Due to model complexity, uncertainty propagation must be numerical and can be performed using various numerical methods, a few important methods are briefly described in this short review:

- *Monte Carlo-based methods*: Monte Carlo methods denote a broad class of methods based on random sampling from the input probability distributions and evaluating the simulation code at each sample. These methods are versatile in the sense that their convergence is independent of the dimensionality and regularity of the problem. However they are computationally expensive due to the slow convergence rate, which is proportional to $1/\sqrt{N}$, where N is the number of sampling points.
- *Polynomial-based methods - Polynomial chaos (PC)*: This method was originally developed by [71], where Hermite polynomials were used to represent the uncertainty of a normal random variable. In a PC expansion (PCE) [72], an arbitrary random vector (quantities of interest) is represented as a function of input random field. The polynomial is uni- or multivariate depending on the dimension of the random field. The input random parameter is represented by a probability distribution, which is associated to a set of *orthogonal* polynomials, for example Legendre polynomials correspond to a uniform distribution. Also there are non-intrusive PC methods such as *Probabilistic Collocation*, based on Lagrangian polynomials which is essentially polynomial interpolation/quadrature with optimally chosen nodes based on input distribution. It has been shown to be efficient for a flow problem over an airfoil [73].

Other methods for uncertainty propagation such as multi-level Monte Carlo, Kriging, first-order reliability method and interval analysis can also be employed. The reader is referred to [70] for details about other propagation techniques.

2.4.2. INVERSE UQ - BAYESIAN PERSPECTIVE

The category of methods that are implemented in this dissertation are based on the Bayesian framework [74], which can be applied to infer information about unknown parameters through a calibration procedure using experimental data. In order to define the procedure, let θ denote the parameter about which inference is to be made and y be the observed data or experimental measurements. It is of interest to provide probability statements about θ given y , for which a joint

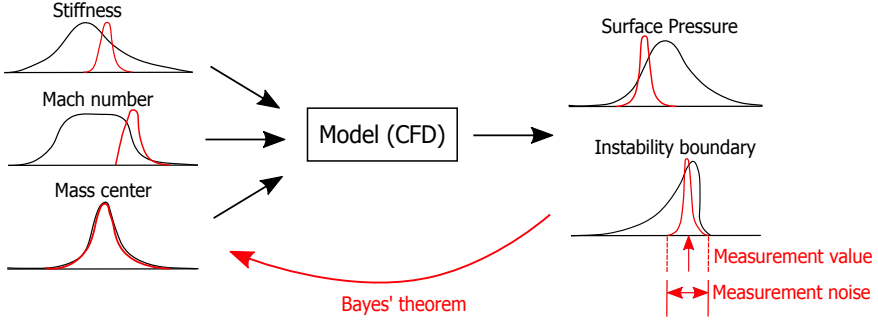


Figure 2.3: Bayesian calibration (marked in red) where measurement data on flutter boundary used to obtain posteriors on input parameters such as stiffness.

probability distribution for θ and y is written as:

$$\mathbb{P}(\theta, y) = \mathbb{P}(\theta)\mathbb{P}(y | \theta), \quad (2.25)$$

where $\mathbb{P}(\theta)$ is known as the *prior* probability and $\mathbb{P}(y | \theta)$ is the *likelihood* function. Bayes' rule can be used here in order to obtain:

$$\mathbb{P}(\theta | y) = \frac{\mathbb{P}(\theta, y)}{\mathbb{P}(y)} = \frac{\mathbb{P}(\theta)\mathbb{P}(y | \theta)}{\mathbb{P}(y)}, \quad (2.26)$$

where $\mathbb{P}(\theta | y)$ is the *posterior* distribution, which provides the update on the unknown parameter θ . In most cases, the *evidence* $\mathbb{P}(y)$ is considered a constant as it is independent of θ , which simplifies (2.26) to give the posterior density as:

$$\mathbb{P}(\theta | y) \propto \mathbb{P}(\theta)\mathbb{P}(y | \theta). \quad (2.27)$$

The posterior distribution can then be employed in the forward problem in order to provide posterior predictions of the quantities of interest. The method is demonstrated in Figure 2.3. However statistics of the posterior are not known explicitly in the form of a probability density, and hence sampling must be performed using techniques such as Markov Chain Monte Carlo (MCMC) [75]. A short review of the literature on UQ in aeroelasticity, specifically with respect to wind turbines is provided in subsequent chapters.

2.5. SUMMARY OF METHODS

From the discussion of the literature on different methods, the models/techniques that are developed/implemented in this dissertation are summarised here. The details will be further provided in the relevant chapters.

- *Aeroelastic solver and instabilities*: For the structural part, a modal solver is selected, which is based on consideration of non-uniform material properties for the case of the wind turbine. The fluid solver is based on RANS-based Navier-Stokes formulation considering compressible flow conditions. A partitioned solver is used for the aeroelastic solution, with interface treatment based on infinite-plate spline technique. In terms of instabilities, flutter is investigated in case of aircraft test case and structural fatigue is a potential application for wind turbines.
- *Reduced Order Model*: Data-driven time-domain ROMs based on input/output map-identification is implemented. While training the ROMs, the inputs are the prescribed deformation (modal displacements), while the outputs are the force/pressure distribution on the wing/blade surface. The ROM is only trained for the fluid component, and the structural solver is then coupled to the trained ROM. These ROMs are generalised across an operating regime by parametrising the training parameters. Further, for the case of reconstructing wind turbine loads, a Gaussian forcing term is included in the formulation to take into account the forcing from the tower wake.
- *UQ and Bayesian updating*: The standard Monte Carlo method is used for sampling in the forward propagation, since development of ROM makes this operation cheap. Experimental data is employed for identification of parameters and a Markov Chain Monte Carlo algorithm is used for sampling from the posterior.

REFERENCES

- [1] E. H. Dowell, *A Modern Course in Aeroelasticity*, Vol. 217 (Springer, 2015).
- [2] A. R. Collar, *The Expanding Domain of Aeroelasticity*, *Journal of the Royal Aeronautical Society* **50**, 613 (1946).
- [3] F. White, *Viscous Fluid Flow*, 3rd ed. (McGraw-Hill Education, 2005) p. 640.
- [4] C. Hirsch, *Numerical computation of internal and external flows*, Vol. 1 (John Wiley & Sons, Ltd., 2007).
- [5] J. Boussinesq, *Essai sur la théorie des eaux courantes*, *Journal de Mathématiques pures et appliquées* **3**, 335 (1878).
- [6] A. H. Nayfeh and P. F. Pai, *Linear and Nonlinear Structural Mechanics* (John Wiley & Sons, Inc., 2004).

- [7] L. Meirovitch, *Elements of Vibration Analysis* (McGraw-Hill, Inc., 1986).
- [8] R. Kamakoti and W. Shyy, *Fluid-structure interaction for aeroelastic applications*, [Progress in Aerospace Sciences](#) **40**, 535 (2004).
- [9] M. Sadeghi, F. Liu, K. L. Lai, and H. M. Tsai, *Application of Three-Dimensional Interfaces for Data Transfer in Aeroelastic Computations*, in [22nd Applied Aerodynamics Conference and Exhibit](#) (American Institute of Aeronautics and Astronautics, Providence, Rhode Island, 2004) pp. 1–30.
- [10] R. L. Bisplinghoff and H. Ashley, *Principles of Aeroelasticity* (Dover Publications, Inc., New York, 1962).
- [11] M. D. Pavel and M. M. J. Schoones, *Literature Survey on Aeromechanical Instabilities for helicopters and wind turbines*, Tech. Rep. (Delft University of Technology, Delft, 1999).
- [12] J. G. Holierhoek, *Aeroelasticity of Large Wind Turbines*, Ph.D. thesis, Delft University of Technology (2008).
- [13] H. Stiesdal, *Extreme wind loads on stall regulated wind turbines*, in [Proceedings of the 16th British Wind Energy Association Conference](#) (Mechanical Engineering Publications Ltd., Stirling, UK, 1994) pp. 101–106.
- [14] T. Møller, *Blade cracks signal new stress problem*, Tech. Rep. (WindPower Monthly, 1997).
- [15] P. Lundsager, H. Petersen, and S. Frandsen, *The dynamic behaviour of the stall-regulated a wind turbine*, Tech. Rep. (Risø National Laboratory, Denmark, 1981).
- [16] D. W. Lobitz, *Parameter Sensitivities Affecting the Flutter Speed of a MW-Sized Blade*, [Journal of Solar Energy Engineering](#) **127**, 538 (2005).
- [17] M. Hansen, *Stability Analysis of Three-Bladed Turbines Using an Eigenvalue Approach*, in [42nd AIAA Aerospace Sciences Meeting and Exhibit](#) (American Institute of Aeronautics and Astronautics, Reno, Nevada, 2004) pp. 1–11.
- [18] H. J. Sutherland, [Sandia National Laboratories](#), Tech. Rep. (Sandia National Laboratories (SNL), Albuquerque, NM, and Livermore, CA, 1999).
- [19] C. Farhat, P. Geuzaine, and G. Brown, *Application of a three-field nonlinear fluid-structure formulation to the prediction of the aeroelastic parameters of an F-16 fighter*, [Computers and Fluids](#) **32**, 3 (2003).

- [20] E. H. Dowell and T. Ueda, *Flutter analysis using nonlinear aerodynamic forces*, *Journal of Aircraft* **21**, 101 (1984).
- [21] K. C. Hall, J. P. Thomas, and W. S. Clark, *Computation of Unsteady Nonlinear Flows in Cascades Using a Harmonic Balance Technique*, *AIAA Journal* **40**, 879 (2002).
- [22] K. Ekici and K. C. Hall, *Harmonic Balance Analysis of Limit Cycle Oscillations in Turbomachinery*, *AIAA Journal* **49**, 1478 (2011).
- [23] P. Greco, C. Lan, and T. Lim, *Frequency domain unsteady transonic aerodynamics for flutter and limit cycle oscillation prediction*, 35th Aerospace Sciences Meeting and Exhibit **XXXII** (1997).
- [24] W. Yao and S. Marques, *Application of a high-order CFD harmonic balance method to nonlinear aeroelasticity*, *Journal of Fluids and Structures* **74**, 427 (2017).
- [25] B. Moore, *Principal component analysis in linear systems: Controllability, observability, and model reduction*, *IEEE Transactions on Automatic Control* **26**, 17 (1981).
- [26] A. C. Antoulas, *SVD—Krylov Methods*, in *Approximation of Large-Scale Dynamical Systems* (Society for Industrial and Applied Mathematics, 2005) pp. 365–388.
- [27] L. Sirovich, *Turbulence and the dynamics of coherent structures. II. Symmetries and transformations*, *Quarterly of Applied Mathematics* **45**, 573 (1987).
- [28] M. Rathinam and L. R. Petzold, *A New Look at Proper Orthogonal Decomposition*, *SIAM Journal on Numerical Analysis* **41**, 1893 (2003).
- [29] T. Kim, *Parametric model reduction for aeroelastic systems: Invariant aeroelastic modes*, *Journal of Fluids and Structures* **65**, 196 (2016).
- [30] E. H. Dowell, J. P. Thomas, and K. C. Hall, *Transonic limit cycle oscillation analysis using reduced order aerodynamic models*, *Journal of Fluids and Structures* **19**, 17 (2004).
- [31] P. J. Schmid, *Dynamic mode decomposition of numerical and experimental data*, *Journal of Fluid Mechanics* **656**, 5 (2010).
- [32] J. H. Tu, *Dynamic mode decomposition - theory and applications*, Ph.D. thesis, Princeton University (2013).

- [33] W. A. Silva, *Discrete-time Linear and Nonlinear Aerodynamic Impulse Responses for Efficient Cfd Analyses*, Ph.D. thesis, The College of William and Mary (1997).
- [34] D. E. Raveh, Y. Levy, and M. Karpel, *Efficient aeroelastic analysis using computational unsteady aerodynamics*, [Journal of Aircraft](#) **38**, 547 (2001).
- [35] W. A. Silva and R. E. Bartels, *Development of reduced-order models for aeroelastic analysis and flutter prediction using the CFL3Dv6.0 code*, [Journal of Fluids and Structures](#) **19**, 729 (2004).
- [36] T. J. Cowan, A. S. Arena, and K. K. Gupta, *Accelerating Computational Fluid Dynamics Based Aeroelastic Predictions Using System Identification*, [Journal of Aircraft](#) **38**, 81 (2001).
- [37] D. E. Raveh, *Identification of computational-fluid-dynamics based unsteady aerodynamic models for aeroelastic analysis*, [Journal of Aircraft](#) **41**, 620 (2004).
- [38] W. Zhang and Z. Ye, *Reduced-Order-Model-Based Flutter Analysis at High Angle of Attack*, [Journal of Aircraft](#) **44**, 2086 (2007).
- [39] W. Zhang and Z. Ye, *Control law design for transonic aeroservoelasticity*, [Aerospace Science and Technology](#) **11**, 136 (2007).
- [40] W. Zhang, Z. Ye, and C. Zhang, *Aeroservoelastic Analysis for Transonic Missile Based on Computational Fluid Dynamics*, [Journal of Aircraft](#) **46**, 2178 (2009).
- [41] G. J. Balas, *Linear, parameter-varying control and its application to a turbofan engine*, [International Journal of Robust and Nonlinear Control](#) **12**, 763 (2002).
- [42] F. D. Bianchi, H. de Battista, and R. J. Mantz, *Modelling of Variable-speed Variable-pitch Wind Energy Conversion Systems*, in [Wind Turbine Control Systems](#) (Springer-Verlag London, London, 2007) 1st ed., p. 208.
- [43] J. W. van Wingerden, I. Houtzager, F. Felici, and M. Verhaegen, *Closed-loop identification of the time-varying dynamics of variable-speed wind turbines*, [International Journal of Robust and Nonlinear Control](#) **19**, 4 (2009).
- [44] W. J. Rugh, *Analytical Framework for Gain Scheduling*, in [American Control Conference](#) (IEEE, 1990) pp. 1688–1694.

- [45] Y. Bolea, R. Martinez-Gonzalez, A. Grau, and H. Martinez-Garcia, *An LPV Fractional Model for Canal Control*, in *15th IFAC Symposium on System Identification* (IFAC, 2009) pp. 1786–1791.
- [46] X. Wei and L. Del Re, *On persistent excitation for parameter estimation of quasi-LPV systems and its application in modeling of diesel engine torque*, in *14th IFAC Symposium on System Identification* (IFAC, 2006) pp. 517–522.
- [47] G. Belforte and P. Gay, *Optimal Worst Case Estimation for LPV-FIR Models with Bounded Errors*, in *39th IEEE Conference on Decision and Control* (IEEE, 2000) pp. 4573–4577.
- [48] F. Previdi and M. Lovera, *Identification of Nonlinear Parametrically Varying Models Using Separable Least Squares*, *IFAC Proceedings Volume 36*, 1531 (2003).
- [49] L. Lee and K. Poolla, *Identification of linear parameter-varying systems via LFTs*, in *35th IEEE Conference on Decision and Control* (IEEE, 1996) pp. 1545–1550.
- [50] M. Groot, M. V. D. Wal, C. Scherer, and O. Bosgra, *LPV control for a wafer stage : beyond the theoretical solution*, *Control Engineering Practice* **13**, 231 (2005).
- [51] M. Nemani, R. Ravikanth, and B. A. Bamieh, *Identification of linear parametrically varying systems*, in *34th IEEE Conference on Decision and Control* (IEEE, 1995) pp. 2990–2995.
- [52] M. Sznaier and M. Mazzaro, *An LMI approach to control-oriented identification and model (In) validation of LPV systems*, *IEEE Transactions on Automatic Control* **48**, 1619 (2003).
- [53] V. Verdult and M. Verhaegen, *Kernel methods for subspace identification of multivariable LPV and bilinear systems*, *Automatica* **41**, 1557 (2005).
- [54] R. Tóth, *Lecture Notes in Control and Information Sciences*, Vol. 403 (Springer-Verlag Berlin Heidelberg, 2010) pp. 2–3.
- [55] G. V. D. Veen, J.-W. V. Wingerden, M. Bergamasco, M. Lovera, and M. Verhaegen, *Closed-loop subspace identification methods : an overview*, *IET Control Theory and Applications* **7**, 1339 (2013).
- [56] J.-W. van Wingerden, *Control of wind turbines with 'Smart' rotors: Proof of concept & LPV subspace identification*, Ph.D. thesis, Delft University of Technology (2008).

- [57] J.-W. van Wingerden and M. Verhaegen, *Subspace identification of Bilinear and LPV systems for open- and closed-loop data*, *Automatica* **45**, 372 (2009).
- [58] M. Visser, S. T. Navalkar, and J. W. van Wingerden, *LPV Model Identification for Flutter Prediction: Comparison of Methods Prediction*, *IFAC-PapersOnLine* **48**, 121 (2015).
- [59] S. T. Navalkar and J.-W. van Wingerden, *Nuclear Norm-Based Recursive Subspace Identification for Wind Turbine Flutter Detection*, *IEEE Transactions on Control Systems Technology* **26**, 890 (2018).
- [60] W. E. Faller, S. J. Schreck, U. S. A. Force, B. Air, and F. Base, *Unsteady Fluid Mechanics Applications of Neural Networks Introduction*, *Journal of Aircraft* **34**, 48 (1997).
- [61] W. Zhang, B. Wang, Z. Ye, and J. Quan, *Efficient Method for Limit Cycle Flutter Analysis Based on Nonlinear Aerodynamic Reduced-Order Models*, *AIAA Journal* **50**, 1019 (2012).
- [62] W. Yao and M.-S. Liou, *Reduced-Order Modeling for Flutter/LCO Using Recurrent Artificial Neural Network*, in *14th AIAA/ISSMO Multidisciplinary Analysis and Optimization Conference* (American Inst. of Aeronautics and Astronautics, 2012).
- [63] A. Mannarino and P. Mantegazza, *Nonlinear aerodynamic reduced order modeling by discrete time recurrent neural networks*, *Aerospace Science and Technology* **47**, 103 (2015).
- [64] A. Mannarino and E. H. Dowell, *Reduced-Order Models for Computational-Fluid-Dynamics-Based Nonlinear Aeroelastic Problems*, *AIAA Journal* **53**, 2671 (2015).
- [65] J. Paduart, L. Lauwers, J. Swevers, K. Smolders, J. Schoukens, and R. Pintelon, *Identification of nonlinear systems using Polynomial Nonlinear State Space models*, *Automatica* **46**, 647 (2010).
- [66] M. Ripepi, *Model order reduction for computational aeroelasticity*, [Ph.D. thesis](#), Politecnico Di Milano (2014).
- [67] D. Xiu, *Numerical Methods for Stochastic Computations: A Spectral Method Approach* (Princeton University Press, Princeton, NJ, USA, 2010).
- [68] O. L. Maitre and O. M. Knio, *Spectral Methods for Uncertainty Quantification* (Springer Netherlands, 2010).

- [69] R. C. Smith, *Uncertainty Quantification: Theory, Implementation, and Applications* (Society for Industrial and Applied Mathematics, Philadelphia, PA, USA, 2013).
- [70] T. Sullivan, *Introduction to Uncertainty Quantification* (Springer International Publishing, 2015) p. 342.
- [71] N. Wiener, *The Homogeneous Chaos*, *American Journal of Mathematics* **60**, 897 (1938).
- [72] R. G. Ghanem and P. D. Spanos, *Stochastic Finite Elements: A Spectral Approach* (Springer, New York, 1991).
- [73] G. Loeven, J. Witteveen, and H. Bijl, *Probabilistic Collocation: An Efficient Non-Intrusive Approach for Arbitrarily Distributed Parametric Uncertainties*, in *45th AIAA Aerospace Sciences Meeting and Exhibit* (American Institute of Aeronautics and Astronautics, Reno, Nevada, 2007) pp. 1–14.
- [74] A. Gelman, J. B. Carlin, H. S. Stern, and D. B. Rubin, *Bayesian Data Analysis*, 3rd ed. (Chapman & Hall/CRC, 2004) pp. 6–7.
- [75] W. Hastings, *Monte Carlo sampling methods using Markov chains and their applications*, *Biometrika* **57**, 97 (1970).

3

DEVELOPMENT OF AN AEROELASTIC SOLVER

This dissertation considers multiple aeroelastic systems and the computational models for each of them are inherently complex. In particular, the downwind wind turbine system, including all the structural components (namely blade, nacelle and tower), demonstrates complicated flow physics - e.g. interaction of tower wake and blades. In order to model the aeroelastic behaviour accurately, a high-fidelity unsteady fluid-structure interaction solver is required. This chapter discusses the development of such a solver. The aeroelastic solver requires coupling of structural and aerodynamic models. For the structural part, a modal solver is developed, discussed in Section 3.1. Details about the mesh and treatment of mesh interfaces are in Section 3.2. The basic aeroelastic equations and the coupling method that is implemented is mentioned in Section 3.3. Finally the solver is used to obtain aeroelastic predictions, including flutter boundary reconstructions for airfoil and wing and wind turbine unsteady characteristics in Section 3.4. The developed solver will be used to train Reduced Order Models (ROM) in Chapter 4.

3.1. STRUCTURAL SOLVER

The three test cases that are investigated in this dissertation are: a two-Degree-of-Freedom NACA 0012 airfoil, the Golland Wing and a downwind wind turbine system. The airfoil and wing are widely investigated aeroelastic problems and details about them are plentiful in the literature. Therefore few details are mentioned here, whereas the wind turbine model is explained in more detail.

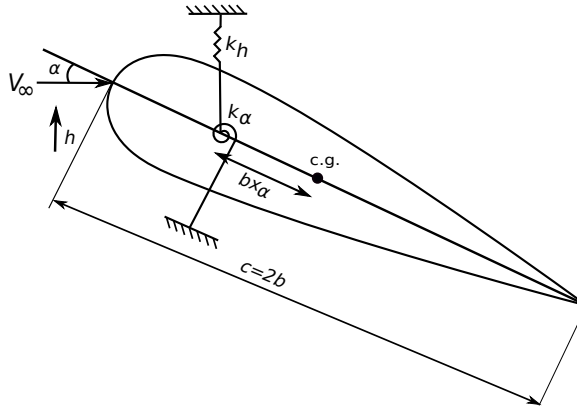


Figure 3.1: NACA 0012 airfoil with pitch and plunge degrees of freedom.

3.1.1. SENSITIVITY ANALYSIS

The structural model is described by many geometrical and physical parameters. In order to perform operations such as structural uncertainty propagation, it may be unnecessary to consider all the structural parameters as the aeroelastic response of interest may not be influenced by the change in certain parameters. Sensitivity analysis can be a useful preprocessing step to identify the parameters which most influence the aeroelastic response.

The idea for the sensitivity analysis is adopted from [1], where the most influential structural parameters for flutter in the Goland wing problem are identified. The methodology includes identification of a function relating the uncertain structural parameters and the output quantity of interest (aeroelastic response such as flutter). Thereafter, a sensitivity vector (gradient) and a Hessian matrix are estimated by differentiating the aeroelastic response function with respect to the structural parameters. The method returns these sensitivity values, which are used to identify the parameters that influence the output quantity of interest. For example, in case of the Goland wing, 7 out of 32 structural parameters were identified to be responsible for 99.5% of the response in the sensitivity analysis.

3.1.2. NACA 0012 AIRFOIL AND GOLAND WING

The NACA 0012 airfoil is a well-investigated test case, both experimentally as well as numerically, with plentiful information on the flutter boundary. The geometrical parameters are based on experiments performed by the Structural Dynamics Division at NASA Langley Research Center, referred to as the Benchmark Models Program (BMP) [2, 3]. A three-dimensional rigid semi-span wing model with a constant-chord NACA 0012 section was used in the experiment. The tests

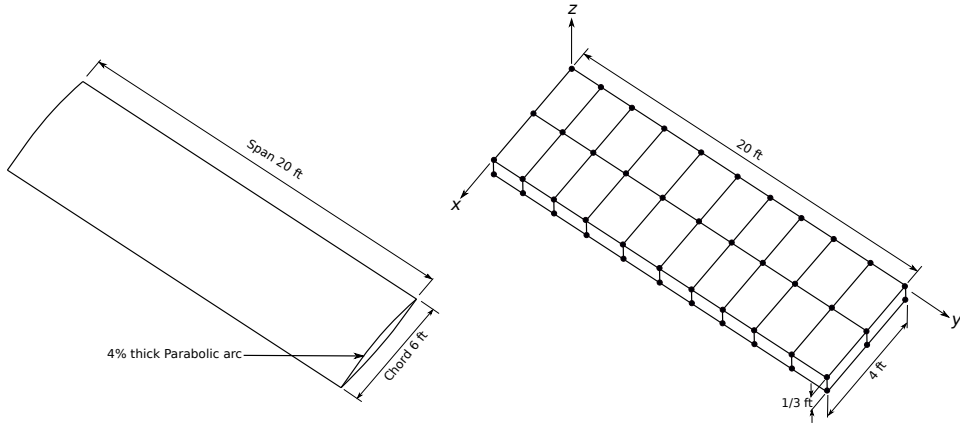


Figure 3.2: Geometry of Goland wing (left) and structural model of the Goland wing with dots representing the structural grid points (right).

were performed on a flexible mount system, referred to as the pitch and plunge apparatus, allowing the 2-DOF movement of the system. The governing equations for the plunge and pitch degrees of freedom of the structural system (shown in Figure 3.1) in non-dimensional form considering damping are given by:

$$\ddot{h} + \frac{x_\alpha}{2} \ddot{\alpha} + \frac{4\zeta_h}{\bar{U}} \frac{\omega_h}{\omega_\alpha} \dot{h} + \left(\frac{2}{\bar{U}} \frac{\omega_h}{\omega_\alpha} \right)^2 h = \frac{2}{\mu\pi} C_L \quad (3.1)$$

$$x_\alpha \ddot{h} + \frac{r_\alpha^2}{2} \ddot{\alpha} + \frac{2\zeta_\alpha r_\alpha^2}{\bar{U}} \dot{\alpha} + \frac{2r_\alpha^2}{\bar{U}^2} \alpha = \frac{4}{\mu\pi} C_m, \quad (3.2)$$

where h and α are the plunge-displacement and pitch-rotation respectively, ζ_h and ζ_α are the damping coefficients in plunge and pitch directions, $\bar{U} = U_\infty / b\omega_\alpha$ is the non-dimensional free stream velocity, where b is the half chord length of the airfoil. The structural parameters of the airfoil are mass $m_a = 87.067$ kg, non-dimensional distance from elastic axis to the centre of gravity $x_\alpha = 0$, length or span of blade $l = 0.8128$ m, chord length $c = 0.4064$ m, radius of gyration $r_\alpha = 1.012$, ratio of plunge to pitch natural frequencies $\omega_h/\omega_\alpha = 0.646$. Stiffness $k_h = m\omega_h^2$ and $k_\alpha = I_\alpha\omega_\alpha^2$, where I_α is the moment of inertia, are non-dimensionalised. The inverse mass ratio is defined by $\mu^{-1} = \pi\rho l(c^2/4)/m_a$, C_L and C_m are the lift and moment coefficients, obtained from the aerodynamic solution. The fourth-order Runge Kutta algorithm is used to advance the solution forward in time, with the force coefficients updated with the change in flow field.

The Goland wing is a three-dimensional numerical test case (experiments don't exist), which is a rectangular and cantilevered beam, shown in Figure 3.2. It is a widely studied aeroelastic test case, also with respect to structural uncertainty [4]. In this dissertation, the clean configuration of the Goland wing is con-

sidered, that is, without tip store (which is intended to model missile mounted to wing-tip). The Goland wing has a chord length of 6 feet with a span of 20 feet, and the wing cross section is bounded with 4%-thick parabolic arcs, defined by $z = \pm 0.08x(1 - x/c)$ for $0 \leq x \leq c$, where c is the chord length. The structural model of the wing is box-type, as shown in Figure 3.2. All the elements have a Young's modulus of 1.4976×10^9 slugs/ft², shear modulus of 5.616×10^8 slugs/ft² and density of 0.0001 slugs/ft³. It is made up of upper and lower skins, 3 spars, 11 ribs and 33 posts. Lumped masses are placed at each grid point of the model with rotational inertia centred at centre of gravity of each section. At internal rib locations, masses of 22.496 slugs were used, with rotational inertia of 50.3396 slug-ft². At the external rib locations, these masses were halved. The reader is referred to [5] for further details about the structural parameters.

As mentioned in the discussion on sensitivity analysis, the Goland wing is defined by 32 structural parameters; however, based on a sensitivity analysis, 7 parameters were identified as responsible for $\sim 99.5\%$ of the sensitivity in the stability eigenvalue. The identified parameters were thicknesses of the upper and lower skin elements; leading- and trailing-edge spars; and the areas of leading-, center-, and trailing-edge spar caps, which are considered uncertain in this paper. The structural solver to be used in the aeroelastic analysis is a modal solver, as introduced in Chapter 2, which requires the estimation of the mode shapes and frequencies. This is obtained using a normal mode analysis with the commercial finite element package NASTRAN [6]. Figure 3.3 shows the first four structural modes of the Goland wing clean configuration. These mode shapes are used in the structural equation to formulate the modal solver.

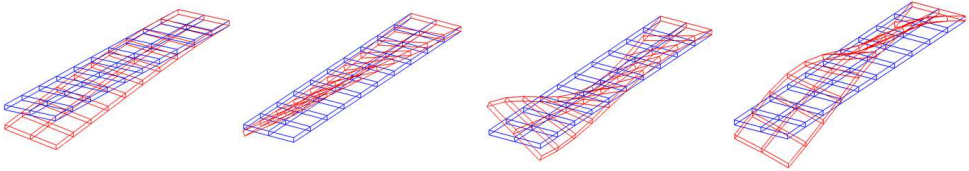


Figure 3.3: First four modes of the Goland wing with frequencies 1.98, 4.05, 9.68 and 13.28 Hz.

3.1.3. WIND TURBINE BLADE

The wind turbine model is a 3-bladed experimental wind turbine of downwind orientation developed by Verelst [7]. The experiments were performed at the Open Jet Facility of the Delft University of Technology, shown in Figure 3.4. The blade tip radius was 0.8 m with NREL S823 and S822 airfoils at inboard and outboard sections respectively. There were 2 blade-types: flexible and stiff. This is based on the number of layers of glass fibre of which the blades were con-

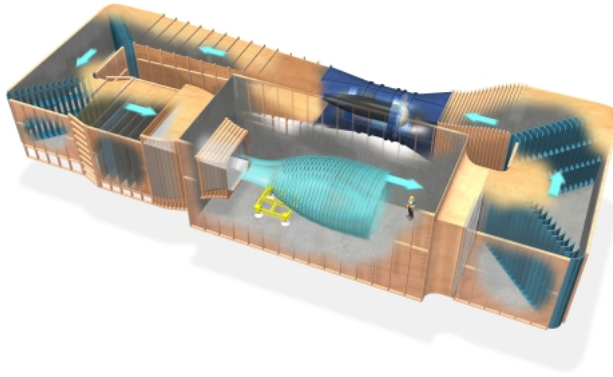


Figure 3.4: Schematic of the open jet facility.

structed, which was two and eight layers in the flexible and stiff set respectively. The reader is referred to [7] for further details. Due to the internal glass fibre and foam based structure, in addition to the twist and chord variation along the span of the blade, there is a non-uniform distribution of mass and stiffness properties.

The structural model of the blade must take into account the non-uniform structural properties of the blade, which will be treated as uncertain in Chapter 5. A modal structural solver is developed using an ODE model of the wind turbine blade undergoing rotation. Approximate sectional mass and stiffness properties are obtained from the experimental measurements, which were based on an optimisation procedure with the measured eigenfrequencies as objective function [7].

VERIFICATION OF STRUCTURAL SOLVER

The equation of motion of a rotating beam (assembly shown in Figure 3.5) with non-uniform sectional properties is given by [8]:

$$\begin{aligned} \frac{d^2}{dz^2} \left[E(z) I_y(z) \frac{d^2 u}{dz^2} \right] - \frac{d}{dz} \left[\frac{d}{dz} (u + r_y \psi) \int_z^L m(z) \Omega^2 (R + z) dz \right] \\ = m(z) \frac{d^2 u}{dt^2} + m(z) r_y \frac{d^2 \psi}{dt^2}, \quad (3.3) \end{aligned}$$

$$\begin{aligned} \frac{d^2}{dz^2} \left[E(z)I_x(z) \frac{d^2 v}{dz^2} \right] - \frac{d}{dz} \left[\frac{d}{dz} (v + r_x \psi) \int_z^L m(z)\Omega^2 (R+z) dz \right] \\ = m(z) \frac{d^2 v}{dt^2} + m(z)r_x \frac{d^2 \psi}{dt^2}, \quad (3.4) \end{aligned}$$

$$\begin{aligned} \frac{d}{dz} \left[G(z)J(z) \frac{d\psi}{dz} \right] + r_y \frac{d}{dz} \left[\frac{d}{dz} (u + r_y \psi) \int_z^L m(z)\Omega^2 (R+z) dz \right] \\ + r_x \frac{d}{dz} \left[\frac{d}{dz} (v + r_x \psi) \int_z^L m(z)\Omega^2 (R+z) dz \right] \\ = -m(z)r_y \frac{d^2 u}{dt^2} - m(z)r_x \frac{d^2 v}{dt^2} - I_\alpha(z) \frac{d^2 \psi}{dt^2}, \quad (3.5) \end{aligned}$$

where, u and v are the edgewise and flapwise displacements in x and y respectively, while ψ is the torsional deflection about z -axis. E and G are the Young's modulus and shear modulus, I_x and I_y are the moments of inertia, J is the polar moment of area. r_x and r_y are the distances between centre of flexure and centre of gravity in x and y , m is the mass per unit length of the beam, while R is the distance from centre of rotation to the root of blade and Ω is the rotational speed of blade. The reader is referred to [9] for further details about the derivation of (3.3 - 3.5).

Flapwise, edgewise and torsional modal frequencies and mode shapes are obtained from (3.3 - 3.5) for the wind turbine blades. The frequencies of vibration ω are validated with the experimentally obtained natural frequencies, see Table 3.1. It can be seen that the first (ω_1) and second frequencies (ω_2) are close to the experimental values. However, for the flexible blades, the third frequency ω_3 does not correspond to the experimental observations. This is attributed to the fact that the third frequency in the simulation is from an edgewise mode, which is not reported in the experiment. Note that on the other hand, ω_4 is a good match with the experimental ω_3 . Based on this, we consider the structural model validated and the estimated modes are used to build the modal structural solver.

NORMAL MODES SOLVER

The structural equations (3.3 - 3.5) are expressed in modal form to reduce dimensionality of model. Assuming zero offset between the centre of flexure and gravity and with an external forcing $F(z, t)$, (3.3) can be written as:

$$\frac{d^2}{dz^2} \left[E(z)I_y(z) \frac{d^2 u}{dz^2} \right] - \frac{d}{dz} \left[\frac{du}{dz} \mathcal{R}(z) \right] = m(z) \frac{d^2 u}{dt^2} + F(z, t), \quad (3.6)$$

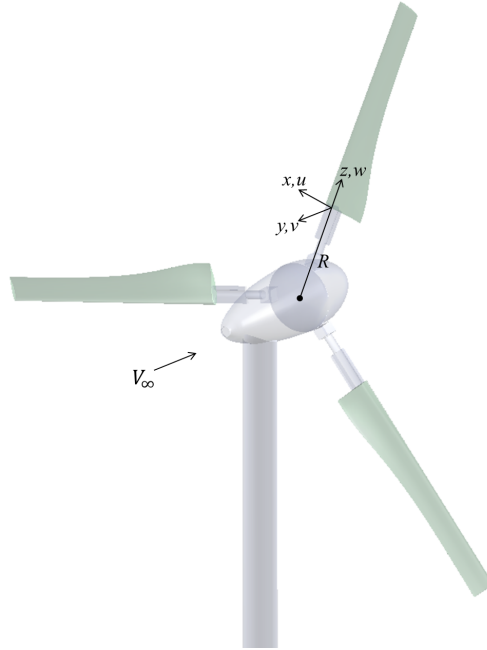


Figure 3.5: Schematic of the 3-bladed downwind wind turbine with nacelle and tower of [7].

| Blades | ω_1 | | ω_2 | | ω_3 | | ω_4 | |
|---------|------------|------|------------|------|------------|------|------------|-------|
| | Expt | Code | Expt | Code | Expt | Code | Expt | Code |
| Stiff 1 | 17.0 | 16.9 | 74.0 | 80.9 | 91.0 | 86.3 | 184.0 | 200.7 |
| Stiff 2 | 17.0 | 16.7 | 72.0 | 77.8 | 89.0 | 86.0 | 182.0 | 194.2 |
| Flex 1 | 11.0 | 11.0 | 54.0 | 55.1 | 135.0 | 56.9 | - | 136.1 |
| Flex 2 | 12.0 | 12.1 | 54.0 | 56.5 | 135.0 | 61.9 | - | 136.5 |

Table 3.1: Comparison of experimental [7] and numerical structural frequencies (in Hz) for two flexible and two stiff blades.

where $\mathcal{R}(z) = \int_z^L m(z)\Omega^2(R+z)dz$. The solution of (3.6) is assumed to be given by:

$$u(z, t) = \sum_{n=1}^{\infty} U_n(z) f_n(t). \quad (3.7)$$

If we assume that the basis $f_n(t)$ is harmonic and orthonormal, the characteristic functions satisfy the differential equation:

$$\frac{d^2}{dz^2} \left[E(z) I_y(z) \frac{d^2 U_n(z)}{dz^2} \right] - \frac{d}{dz} \left[\frac{dU_n(z)}{dz} \mathcal{R}(z) \right] = -m(z) \omega_n^2 U_n(z), \quad (3.8)$$

where, ω_n is the natural frequency of vibration of the system. Now substituting (3.7) in (3.6), we obtain:

$$\begin{aligned} \sum_{n=1}^{\infty} \left[\frac{d^2}{dz^2} \left[E(z) I_y(z) \frac{d^2 U_n(z)}{dz^2} \right] - \frac{d}{dz} \left[\frac{dU_n(z)}{dz} \mathcal{R}(z) \right] \right] f_n(t) \\ = \sum_{n=1}^{\infty} m(z) \frac{d^2 f_n(t)}{dt^2} U_n(z) + F(z, t). \end{aligned} \quad (3.9)$$

Equation (3.8) is substituted in (3.9) to obtain:

$$\sum_{n=1}^{\infty} U_n(z) \frac{d^2 f_n(t)}{dt^2} + \sum_{n=1}^{\infty} \omega_n^2 U_n(z) f_n(t) = -\frac{1}{m} F(z, t). \quad (3.10)$$

Now both sides of (3.10) are multiplied by $U_m(z)$ and integrated between 0 and L , the length of the beam.

By orthonormality of $U_m(z)$, (3.10) reduces to:

$$\frac{d^2 f_n(t)}{dt^2} + \omega_n^2 f_n(t) = Q_n(t), \quad (3.11)$$

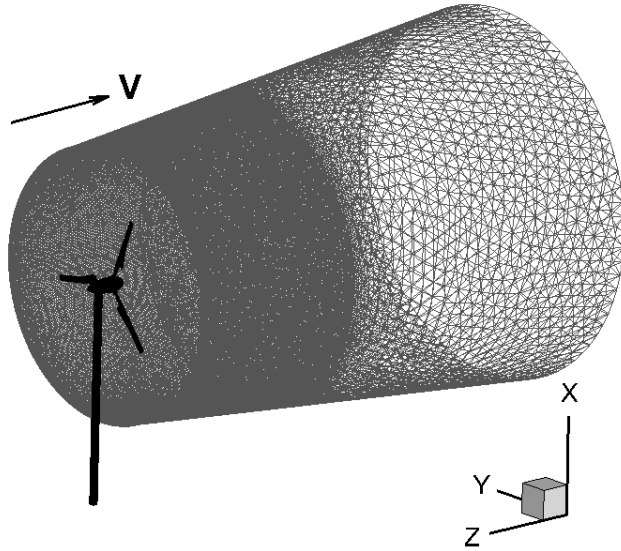
where $Q_n(t)$ is given by:

$$Q_n(t) = -\frac{1}{m_n} \int_0^L F(x, t) U_n(z) dz. \quad (3.12)$$

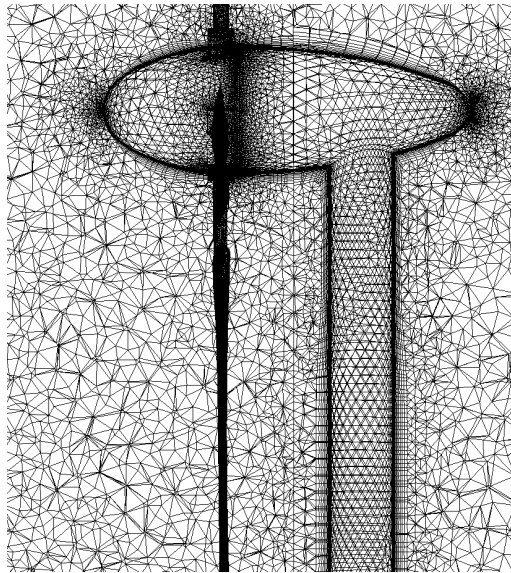
Equation (3.11) is the modal structural equation, where the modal forcing $Q_n(t)$ is the aerodynamic forcing term, to be interpolated from the fluid to the structural mesh.

3.2. MESH GENERATION AND FLUID SOLVER

For the NACA 0012 airfoil, a structured C-mesh is used, while in case of Golland wing, a fully unstructured mesh is employed. In the case of the wind turbine,



(a) Full mesh of the computational domain - only rotating part.



(b) Boundary layer resolution of tower and nacelle.

Figure 3.6: Mesh generation in downwind wind turbine system including all structural components - nacelle, tower and blade.

Table 3.2: Computational domain in millions of cells and CPU hours consumed per rotation of the wind turbine.

| Mesh size | $\Delta t(\theta)$ | CPUs (hours) |
|-----------|--------------------|--------------|
| 13 M | 1.12° | 80 (362 h) |

3

we use a standard hybrid mesh with a structured mesh for resolving the boundary layer and an unstructured mesh for the rest of the domain as shown in Figures 3.6a and 3.6b. Such hybrid meshes are known to be able to provide accurate results for wind turbine flows [10, 11]. The unsteady compressible Navier-Stokes equations are discretised using cell-centered finite volume method. A second-order upwind scheme [12] is used for spatial discretisation and temporal terms are discretised with a second-order implicit time-stepping scheme with dual time formulation. The solver employs a low-Mach number time-derivative unsteady preconditioner, where physical time-derivatives march the unsteady terms, while the preconditioned time-derivatives are used for numerical discretisation and iterative solution [13, 14]. For the rotating domain, the Navier Stokes equations are written in the moving frame of reference in the relative velocity formulation, with addition of a Coriolis and a centrifugal force term [15]. The details of the mesh and computational resources are mentioned in Table 3.2, where the time step Δt is stated in terms of the rotation angle θ of the wind turbine blades.

For the airfoil and wing problems, the RANS turbulence closure, Launder-Spalding $k-\epsilon$ model [16] is employed. In case of the wind turbine, we use the SST $k-\omega$ model [17], which has been previously employed for wind turbine applications [18–20]. The boundary layer is resolved on the walls of the blades, nacelle, tower and all the blade attachments, ensuring $y^+ < 1$. For the near wall treatment in the standard $k-\epsilon$ model [21], the solver implements a two-layer approach for enhanced wall treatment, dividing the domain into a viscosity-affected near wall and fully turbulent region, which is demarcated by a wall-distance based turbulent Reynolds number. In the near-wall region, the one-equation model of Wolfshtein [22] is used, where momentum and k equations are retained as per the standard model, while turbulent viscosity has a two-layer formulation. A blending function is used to smoothly blend the turbulent viscosities in the two regions [23]. Due to the presence of the tower, the computational domain consists of a rotating and a non-rotating zones. A sliding mesh technique based on virtual polygon approach, is employed for the interface treatment between the two zones. In most problems, the mesh in the stationary and rotating zones are non-conforming. In order to compute the flux across the interface of these

zones, the solver forms an interior zone at the intersection of these zones, using a periodic repeats option. This interior zone is dynamically updated according to the relative movement between the stationary and rotating zones.

3.3. AEROELASTIC EQUATIONS

The aeroelastic codes are developed by coupling a linear modal structural solver with Euler/Navier-Stokes flow solver. The coupled solver deforms the fluid mesh according to the structural displacement at every time-step. The full order coupled discrete system can be solved for estimation of stability characteristics by integration of the system forward in time. The coupled system can be also expressed as:

$$\frac{d\mathbf{u}_a}{dt} + \mathbf{R}_a(\mathbf{u}_a; T\mathbf{u}_s^\Gamma, M_\infty) = 0, \quad (3.13)$$

$$\frac{d\mathbf{u}_s}{dt} + \mathbf{R}_s(\mathbf{u}_s; T^T F(\mathbf{u}_a^\Gamma), \mathbf{s}) = 0, \quad (3.14)$$

where \mathbf{R}_a and \mathbf{R}_s are residuals from fluid and structural discretisation, including all boundary conditions; $\mathbf{u}_a \in \mathbb{R}^{N_a}$ and $\mathbf{u}_s \in \mathbb{R}^{N_s}$ are the fluid and structural degrees of freedom, while $\mathbf{u}_a^\Gamma \in \mathbb{R}^{N_a^\Gamma}$ and $\mathbf{u}_s^\Gamma \in \mathbb{R}^{N_s^\Gamma}$ are restricted to the fluid-structure interface Γ . Here $M_\infty \in \mathbb{R}^+$ denotes the Mach number, which plays the role of the *scheduling parameter* (terminology explained in Section 4.2), $\mathbf{s} \in \mathbb{R}^P$ are structural parameters (such as stiffness of individual elements), and $T \in \mathbb{R}^{N_a^\Gamma \times \mathbb{R}^{N_s^\Gamma}}$ is the transformation matrix mapping the structural boundary displacements to the fluid boundary. The flutter point for every Mach number is obtained by performing time-integration of the coupled system.

The fluid and the structural mesh are generally non-conforming, hence the need for the interpolation operator T . Here, we use the Infinite Plate Spline (IPS) method (derived in Appendix B) developed by Harder and Desmarais [24]. IPS identifies a linear map to transform the structural mesh displacement to the fluid mesh. The principle of virtual work implies use of the operator T^T to transform forces from fluid to structural mesh, ensuring conservation of energy. In order to avoid instability due to sudden forcing at the beginning of simulation in (3.11), an initial damping term is introduced for about quarter revolution of the turbine through a damping coefficient, which is gradually reduced to zero. Computation of (3.14) (given \mathbf{w}_a) is inexpensive and involves solution of low-degree of freedom (~ 6) 1st-order ODEs. However the fluid force $\mathbf{F} := F(\mathbf{w}_a)$ must be obtained from the fluid solver at every time step. The flow solution of (3.13), dominates the overall computational cost of the aeroelastic solution. This problem is alleviated in the next chapter with the use of ROMs to approximate the aerodynamic forces.

3.4. AEROELASTIC PREDICTIONS

In this section, the aeroelastic solver introduced in the earlier sections is used to predict dynamic aeroelastic characteristics in the three test cases. In case of airfoil and wing, the flutter boundary is estimated, while blade moment history is the quantity of interest for wind turbine as relevant for fatigue. The flutter point calculation is based on recursive bisection with a tolerance of 10^{-4} on the predicted flutter density.

3

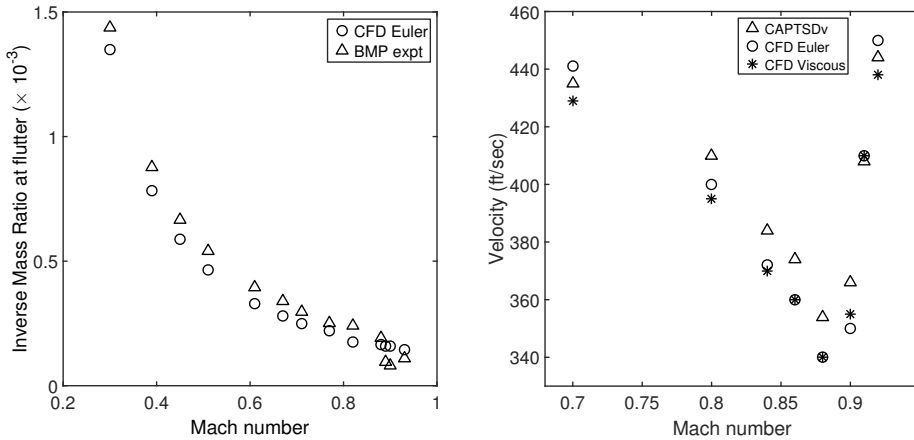
3.4.1. FLUTTER BOUNDARY - NACA0012 AIRFOIL AND GOLAND WING

Figure 3.7 shows the aeroelastic estimates and a comparison to experimental/numerical measurements/ estimates is presented. For the Goland wing, experimental data is not available since it is a numerical test case. Hence the aeroelastic Euler/ Navier–Stokes solvers in case of the wing are validated by comparing the stability bounds obtained in [5], where the flutter boundary is plotted on the $V_\infty - M_\infty$ plane. CAPTSDv [25, 26] couples boundary layer equations with the CAPTSD code [27, 28], which solves the three-dimensional, transonic, small-disturbance, potential-flow equations. The solver was employed to estimate stability boundary of the Goland wing [5].

Figure 3.7a shows the flutter boundary for the NACA 0012 airfoil compared to the Benchmark Models Program (BMP) experimental results [2]. The flutter boundary is plotted in terms of the change in the inverse mass ratio at flutter with the Mach number. It can be seen that the results are in close agreement throughout the Mach number range that is investigated. The flutter boundary for the Goland wing is plotted in Figure 3.7b with both Euler and Navier-Stokes solvers. It is observed that the aeroelastic solvers are able to predict the trend of the transonic dip well. The Navier–Stokes predictions are close to the Euler values with a maximum relative error of less than 3%. In comparison to CAPTSDv, the predictions have a maximum relative error of less than 5%, and hence we consider our model validated.

3.4.2. VALIDATION OF WIND TURBINE DYNAMICS BY THE AEROELASTIC CODE

The aeroelastic characterisation of the wind turbine model is now presented. The experiment of the downwind system that is investigated was performed at varying operating conditions - wind speed, Tip Speed ratio (TSR) of the turbine, temperature and pressure of incoming wind. Additionally for each experiment, the RPM was fluctuating slightly for each revolution. In order to obtain better match between experiments and aeroelastic approximations, we select data with minimal variation in rotation speed, which remains $\sim 3\%$ for the investigated cases. Motivated by this, this rotation parameter will be treated as uncertain in



(a) NACA 0012 airfoil.

(b) Goland wing.

Figure 3.7: Comparison of flutter boundary predicted by aeroelastic code to BMP experiment (left) and CAPTSDv code [5] (right).

Chapter 5. In this section, we provide a detailed analysis of the performance of the aeroelastic solver in estimating the flow physics for a downwind turbine. Parametric effects on the wind turbine performance are also assessed and agreement of the aeroelastic code with experimental data is established.

AGREEMENT WITH EXPERIMENT

In the experiment [7], strain gauges were fixed to the glass fibre-reinforced beam on the blade at the root and at 30%-radial position. They were calibrated by statically loading the beam at different radial positions, and a linear function relating the output of the strain gauge to the bending moment in the blade was defined. In this regard, we can represent the blade moment in two forms:

- (1) Instantaneous aerodynamic moment derived from the blade pressure distribution and,
- (2) Structural moment derived from blade deformation, which is smoother due to the inertia of blade.

It can be said that (2) is a filtered version of (1), where the forcing from the tower wake is represented with a smoother curve without large spikes. In the experiment [7], the blade moments are reported in the form (2). Furthermore, [7] reports significant reservations with respect to the reliability of the absolute values of strain gauge measurements, whereas the moment trend with change in azimuthal angle is expected to be meaningful [7]. With this background, we present the validation of the aeroelastic code in terms of (2) above.

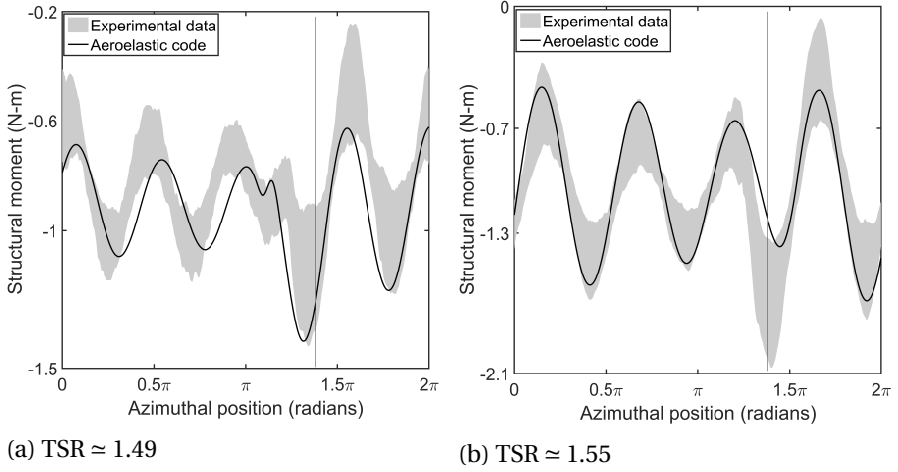


Figure 3.8: Comparison of structural moment estimated at 30%-span location by aeroelastic code to experimental measurement.

Firstly, we record the blade deformations at the root and 30%-locations, which provides us with a parameter closely resembling the strain gauge. Secondly, as an analogous step to the linear function introduced in the calibration step of the experiment, we *scale* the bending moment estimated by the aeroelastic code. We record these for multiple blade rotations. Typically, the data from the first 5 revolutions of the blade is not considered, and a mean blade moment history for each azimuthal position for the remaining data-set is obtained. The azimuthal position is established by recording the initial blade positions (leading edge orientation) in the static position with respect to the tower.

In Figure 3.8, the structural moment variation with azimuthal position is shown for two different experimental data-sets at varying inlet wind velocity V and speed of rotation of the turbine N . Both the experiments were conducted at a low value of Tip Speed Ratio, TSR \approx 1.5 given by,

$$\text{TSR} = \frac{\text{Rotor tip speed}}{\text{Wind speed}} = \frac{\omega R}{V}, \quad (3.15)$$

where, ω and R are the angular velocity and blade tip radius respectively. However, both were conducted at a fixed yaw angle and flexible set of blades were used. The motivation for this choice is the simplification of the flow condition with a fixed yaw angle and also flexible blade measurements are more interesting for this research, since we are investigating aeroelastic effects. In both cases, the experimental structural moment measurements for each rotation of the rotor is plotted, ignoring the data from the first few rotations, shown by the grey area

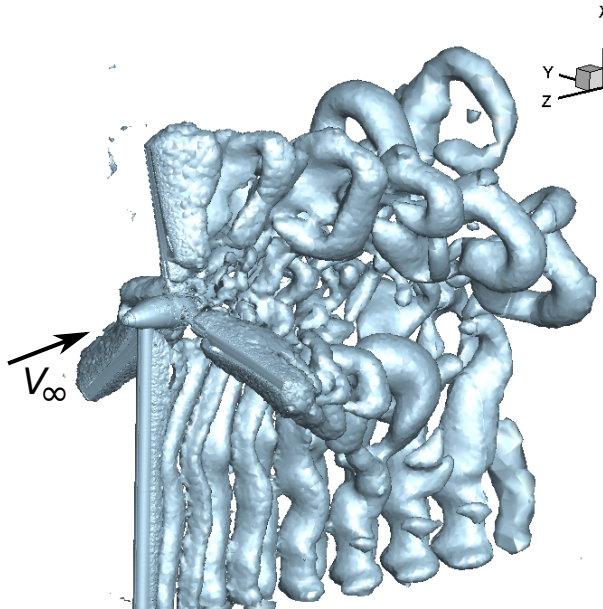
in Figure 3.8. As is clearly evident, the spread in the measurements is considerable with more than 50% variation for certain azimuthal positions. In particular there is large spread in the moment when the blade is in front of the tower, which is near the 1.5π azimuthal position (marked by red line in figure), which is likely due to dependence on phase of shedding. However, a trend can clearly be observed for both the cases. The mean aeroelastic estimate follows the trend quite well, with domain frequencies and amplitudes being reproduced. Significantly, the influence of the tower can clearly be observed in both cases.

ROTOR AND TOWER WAKE VISUALISATION

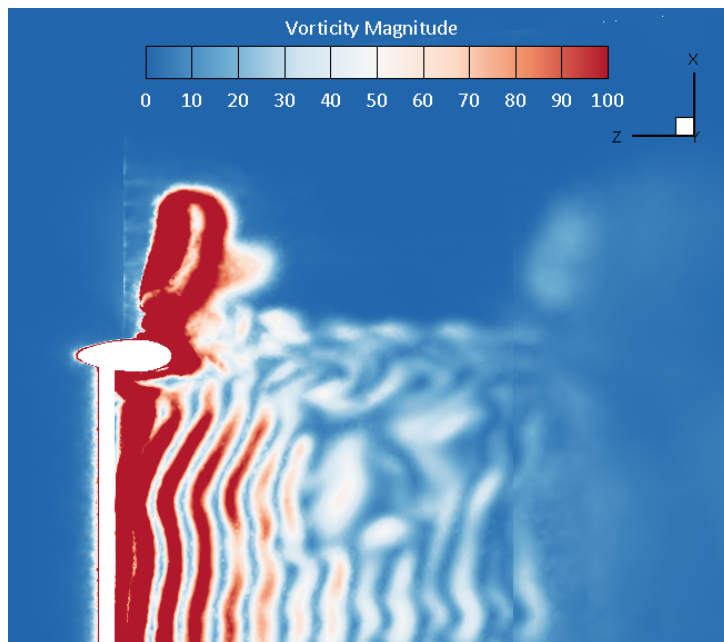
The interaction of tower wake with blades leads to peaks in the generated moment as seen in Figure 3.8, which could lead to structural fatigue. This interaction leads to complex flow features as shown in Figures 3.9-3.11, where inlet flow velocity and speed of rotation are adjusted to obtain a $TSR \approx 6.3$ in Figure 3.11a. The experiments with low rotational fluctuations were conducted at lower TSR values, which results in wind turbine operating in stalled regime. At a higher TSR, the tip vortices are more compactly arranged, which can be captured more effectively due to higher mesh resolution in the near wake region. Figures 3.9a and 3.10a are vortex visualisations at $TSR \approx 0.7$ and 1.7 respectively, which are experimental test conditions. The isosurfaces are plotted with Q -criterion [29] of 55.

For the higher $TSR \approx 6.3$, the tip vortices are distinct and are preserved up to 1.5 revolutions, after which the resolution in the mesh is not sufficient to capture the wake clearly further downstream. Aeroelastic influences are captured due to the higher resolutions in the near wake. While in case of $TSR \approx 0.7$, the tip vortices disintegrate quickly and cannot be clearly identified. This was also observed in [19, 30] and was attributed to the large pitch in the later case, which results in the vortex reaching the coarser mesh region earlier. However in the present investigation, the wind turbine is of downwind orientation, in which case the interaction of the tower wake with tip vortices is even more significant. For $TSR \approx 6.3$, it can be seen that the tower wake influences the disintegration of tip vortices in the lower half of the blade sweep area (below the nacelle), resulting in weakening of vortices in the region. The tower wake growth is not entirely evident in this region at this value of Q , and is attributed to the lower inlet velocity, as a result tower vortices are much weaker than tip.

On the other hand, the tower wake in case of Figure 3.9a can be clearly observed. In Figure 3.10a, the inlet flow velocity is close to that in case of $TSR \approx 0.7$. It can be seen that the tower wake in Figure 3.10a is prominent and is in agreement with Figure 3.9a. It can be concluded from these observations that the tower vortices are much more influential at lower TSRs. Another interesting ob-

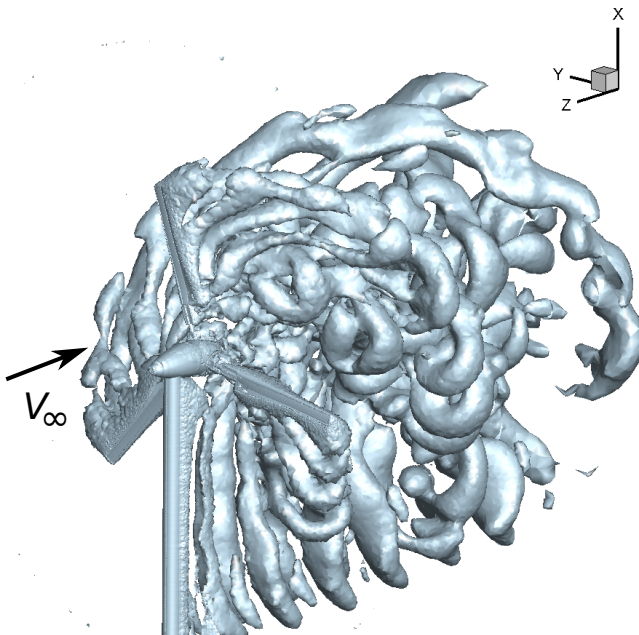


(a) Vortex shedding - plotted with Q -criterion of 55.

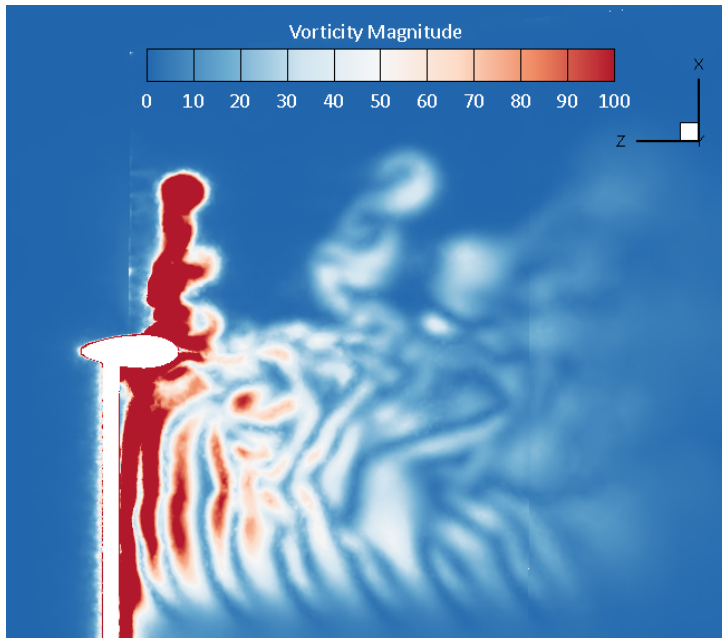


(b) Contours of vorticity magnitude (1/s).

Figure 3.9: Vortex from blade tip, root and nacelle of wind turbine at $TSR \approx 0.7$.



(a) Vortex shedding - plotted with Q -criterion of 55..



(b) Contours of vorticity magnitude (1/s).

Figure 3.10: Vortex from blade tip, root and nacelle of wind turbine at $TSR \approx 1.6$.

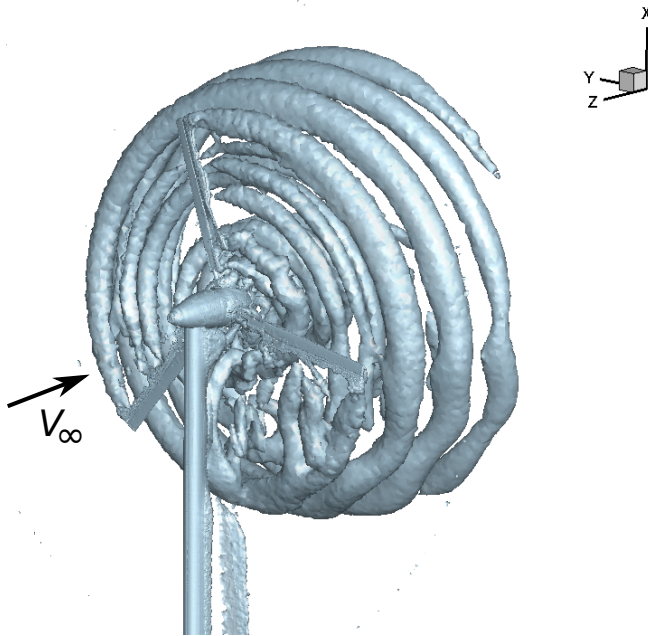
servation from the vortex visualisation in Figure 3.11a is the production of large-scale vortices from multiple locations in the mid-span of the blade. This was also observed in [31] and is attributed to the large change in angle of attack in the trailing edge at that location. Also there are large vortices developed from the nacelle and a strong interaction with the root vortex in the downstream of the axis of the turbine is observed.

The difference in the growth of the vortices in the three test conditions can clearly be observed in Figures 3.9-3.11, where the vorticity magnitude contour is plotted in a plane parallel to the flow direction and bisecting the tower along its length. For $TSR \approx 6.3$, the shedding of the tip vortices can be observed distinctly for approximately 2 (two) revolutions, after which it disintegrates. The root vortex, nacelle and mid-span blade shedding are also clearly visible. Close to the tower, a strong circulation is observed, and the interaction of tower wake with the tip and root vortices can be clearly seen. In Figure 3.9b, the lowest $TSR \approx 0.7$ is plotted, where stronger tower vortices are observed, and as observed with the 3-D visualisation, the tip vortices are not distinct. Similarly, for $TSR \approx 1.6$, strong tower vortices are clearly observed, with a comparable inlet flow velocity. However in this case, it is interesting to note that the tip vortex shedding can be seen for about 1 (one) revolution. Due to the higher rotational speed of the blade, the pitch of the tip vortices is smaller compared to $TSR \approx 0.7$, due to which the mesh resolution is still fine enough to capture the wake.

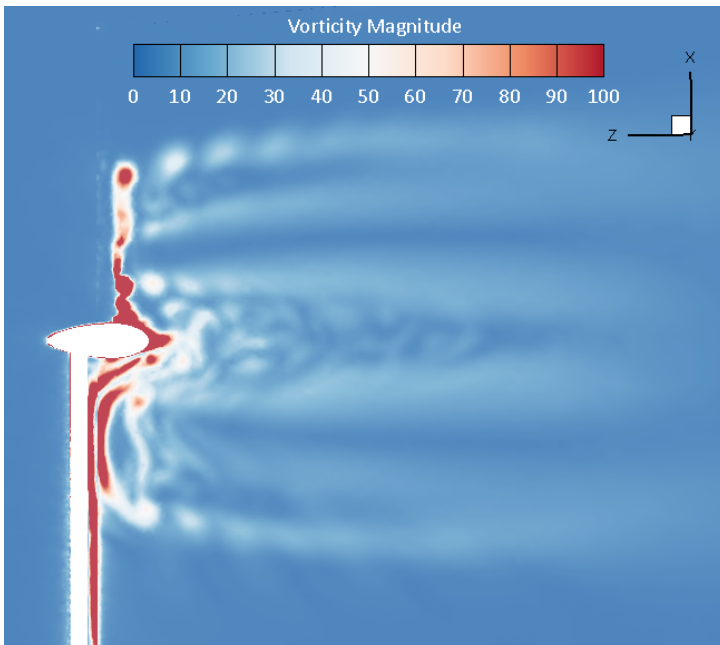
LOW FREQUENCY VARIATIONS IN BLADE MOMENT

For further investigations, we consider $TSR \approx 1.6$ and 6.3 to compare the flow field characteristics, since they demonstrated significantly different wake regions. In Figure 3.12, the aerodynamic moment at 30%-span location is plotted for 12 rotations of the turbine at these two TSR values. The peaks in the moment history correspond to the instants when the blade is in front of the tower. At $TSR \approx 6.3$, the blade is subjected to slightly higher mean moment (that is the moment when it is not in front of the tower). An interesting observation is identification of a low-frequency unsteadiness in the moment peaks for both the cases. For the lower $TSR \approx 1.6$, the amplitude of this low-frequency unsteadiness is observed to be significantly higher with a lower frequency of about 0.37 Hz compared to 1.22 Hz at $TSR \approx 6.3$.

Spontaneous low-frequency modes are not uncommon in fluid dynamics, even in simple geometries, for example in flat plate [32] and circular cylinder [33], where they are attributed to the shrinkage and enlargement of the recirculation region. Both these studies classify the wake formation temporal history into a high-energy mode H and a low-energy mode L, which are characterised by higher and weaker fluctuations in the shear layer respectively. In [32], the modulation in



(a) Vortex shedding - plotted with Q -criterion of 55.



(b) Contours of vorticity magnitude (1/s).

Figure 3.11: Vortex from blade tip, root and nacelle of wind turbine at $TSR \approx 6.3$.

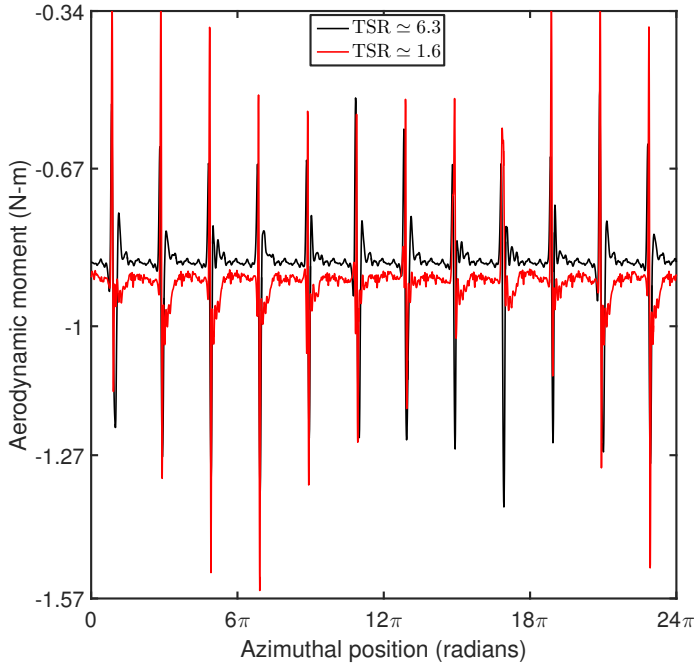
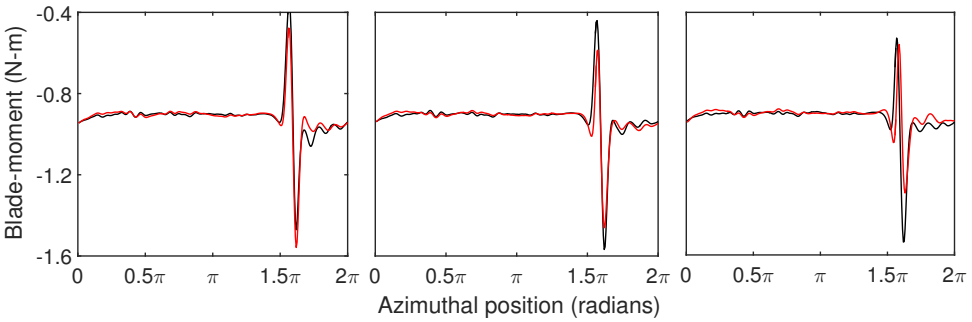


Figure 3.12: Comparison of aerodynamic moment histories at $\text{TSR} \approx 1.6$ and 6.3 .

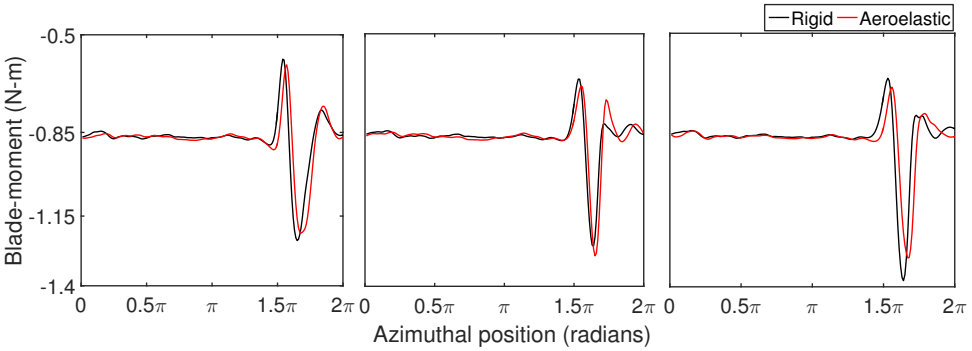
the amplitude is associated with the compact spanwise vortices close to the wall, resulting in shorter recirculation region. This can be associated to the difference in the low-frequency characteristics at the two TSRs. Stronger vortex strength is observed at $\text{TSR} \approx 1.6$ compared to $\text{TSR} \approx 6.3$, which may be attributed to the formation of an analogous H regime as in [32]. This complex phenomena can also be influenced by the rotation speed of the turbine, as the low-frequency in both the TSR cases are also different. Since the objective of this investigation is not to characterise this low-frequency behaviour, it is not pursued further here.

EFFECT OF BLADE ELASTICITY

The change in the blade forcing due to inclusion of blade aeroelasticity is interesting since the nature of the forcing could lead to structural fatigue. Multiple simulations are carried out considering rigid, rotating blades (referred as rigid) and then with flexible rotating blade (referred as aeroelastic). The simulations are allowed to run for around 5 rotor revolutions in order to eliminate effects of the initial condition. In Figure 3.13, comparison of aerodynamic moments obtained at 30%-span location with rigid and aeroelastic codes is shown for $\text{TSR} \approx 1.6$ and 6.3 . The aeroelastic effect slightly varies for each rotation cycle, and hence a dominant pattern is not explicitly observable. This is possible since



(a)



(b)

Figure 3.13: Comparison of aerodynamic moment histories from rigid and aeroelastic calculations for three different rotation cycles at (a) $TSR \approx 1.6$ and (b) $TSR \approx 6.3$.

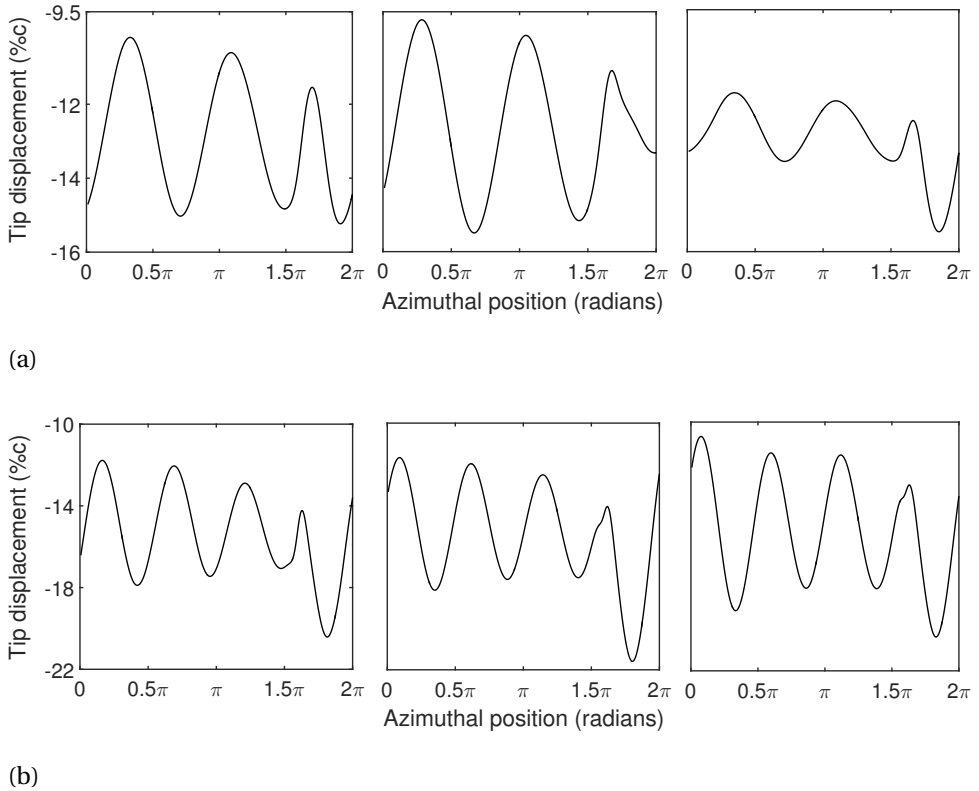


Figure 3.14: Blade tip displacement in flapping direction for three different cycles of rotation in terms of percentage of chord length at (a) $\text{TSR} \approx 1.6$ and (b) $\text{TSR} \approx 6.3$.

the aeroelastic interaction with the wake of the blade can give rise to complicated flow structures and also depends on the phase of the aeroelastic mode and the direction of the tower vortex. In Figure 3.13, we choose three different rotation instances to show the variation in the aeroelastic effect. It can be observed that aeroelasticity introduces a slight delay in the onset of the aerodynamic moment peak due to the tower wake. Also the peaks and range of aerodynamic moment are reduced especially in Figure 3.13a, while the smaller peaks introduced after the blade passes the tower is observed to be higher. In general, it can be said blade flexibility results in smoother variation in the aerodynamic moment, which is more physically intuitive. However the aeroelastic effect for the investigated cases is not very large, as the effect of the structural oscillations on the blade forcing is not significant in comparison to the effect of the tower wake.

In the discussion of Figure 3.8, we mentioned the use of the scaled blade moment in order to obtain comparisons with experimental measurements. It is now

interesting to observe the displacement history of the blades at which the moments are plotted in Figure 3.13. This is shown in Figure 3.14, where the flapping displacement of the blade is plotted, which is normalised with respect to the chord length at the tip of the blade. It can be seen that response in blade displacement around 1.5π -azimuthal position corresponding to the moment peak in Figure 3.13, is not linearly proportional. In case of blade displacement, there is a change in the trend of the curve in both the cases, however the structure does not respond abruptly corresponding to the change in forcing. In case of $TSR \approx 1.6$, the effect of the tower wake on the blade displacement is seen to be more pronounced compared to the higher TSR; the change is however not linearly scalable with respect to the change in the blade forcing. It is also interesting to note the blade displacement is either increased or decreased, when it is in front of the tower. Physically, this can be attributed to the difference in phase between the aeroelastic mode and the shedding vortex.

3.5. SUMMARY

The developed aeroelastic solver is able to provide accurate reconstructions in the flutter boundary for airfoil and Goland wing. For the wind turbine model, the aeroelastic investigations provided many interesting insights into the complex dynamic behaviour. The aeroelastic code is able to reconstruct complex flow features and we have demonstrated the ability of the code to match experimental measurements reasonably well. However owing to the high computational costs as elaborated in Table 3.2, this technique is impractical for performing uncertainty quantification and data assimilation. In the next chapter, we employ the code in a data-driven framework to develop reduced order models in order to perform uncertainty quantification.

REFERENCES

- [1] H. H. Khodaparast, J. E. Mottershead, and K. J. Badcock, *Propagation of structural uncertainty to linear aeroelastic stability*, *Computers and Structures* **88**, 223 (2010).
- [2] J. A. Rivera Jr., B. E. Dansberry, M. H. Durham, R. M. Bennett, and W. A. Silva, *Pressure measurements on a rectangular wing with a NACA0012 airfoil during conventional flutter*, Tech. Rep. (NASA Langley Research Center, Hampton, VA, 1992).
- [3] J. A. Rivera Jr., B. E. Dansberry, R. M. Bennett, M. H. Durham, and W. A. Silva, *NACA 0012 benchmark model experimental flutter results with unsteady pressure distributions*, in *AIAA/ASME/ASCE/AHS/ASC Structures, Structural*

- Dynamics and Materials Conference* (American Institute of Aeronautics and Astronautics, Dallas, TX, United States, 1992) pp. 1898–1908.
- [4] S. Marques, K. J. Badcock, H. H. Khodaparast, and J. E. Mottershead, *Transonic Aeroelastic Stability Predictions Under the Influence of Structural Variability*, *Journal of Aircraft* **47**, 1229 (2010).
- [5] P. S. Beran, N. Khot, E. F.E., R. Snyder, J. Zweber, L. Huttzell, and J. Scott, *The Dependence of Store-Induced Limit-Cycle Oscillation Predictions on Modelling Fidelity*, U.S. Dept. of Defense, *Defense Technical Information Center ADA415759*, 44 (2002).
- [6] MSC Software, *Real Eigenvalue Analysis*, in *MSC Nastran 2014 Dynamic Analysis User's Guide* (MSC Software Corporation, 2014) pp. 43–132.
- [7] D. R. S. Verelst, *Numerical and Experimental Results of a Passive Free Yawing Downwind Wind Turbine*, Ph.D. thesis, Technical University of Denmark (2013).
- [8] K. B. Subrahmanyam and K. R. V. Kaza, *Vibration Analysis of Rotating Turbomachinery Blades By an Improved Finite Difference Method*, *International Journal for Numerical Methods in Engineering* **21**, 1871 (1985).
- [9] W. Carnegie, *Vibrations of Rotating Cantilever Blading: Theoretical Approaches to the Frequency Problem based on Energy Methods*, *Journal Mechanical Engineering Science* **1**, 235 (1959).
- [10] H. Bijl, A. H. van Zuijlen, and A. van Mameren, *Validation of adaptive unstructured hexahedral mesh computations of flow around a wind turbine airfoil*, *International Journal for Numerical Methods in Fluids* **48**, 929 (2005).
- [11] T. J. Carrigan, B. H. Dennis, Z. X. Han, and B. P. Wang, *Aerodynamic Shape Optimization of a Vertical-Axis Wind Turbine Using Differential Evolution*, *ISRN Renewable Energy* **2012**, 1 (2012).
- [12] T. J. Barth and D. C. Jespersen, *The design and application of upwind schemes on unstructured meshes*, Tech. Rep. (AIAA, 1989).
- [13] E. Turkel and V. N. Vatsa, *Choice of Variables and Preconditioning for Time Dependent problems*, in *16th AIAA Computational Fluid Dynamics Conference*, June (American Inst. of Aeronautics and Astronautics, Orlando, Florida, 2003).

- [14] S. A. Pandya, S. Venkateswaran, and T. H. Pulliam, *Implementation of Pre-conditioned Dual-Time Procedures in OVERFLOW*, in *41st Aerospace Sciences Meeting & Exhibit*, January (American Inst. of Aeronautics and Astronautics, Reno, Nevada, 2003).
- [15] C. Hirsch, *Numerical computation of internal and external flows*, Vol. 1 (John Wiley & Sons, Ltd., 2007).
- [16] B. Launder and D. Spalding, *The numerical computation of turbulent flows*, *Computer Methods in Applied Mechanics and Engineering* **3**, 269 (1974), [arXiv:1204.1280v1](https://arxiv.org/abs/1204.1280v1) .
- [17] F. Menter, *Two-equation eddy-viscosity turbulence models for engineering applications*, *AIAA Journal* **32**, 1598 (1994).
- [18] S. Kalvig, E. Manger, and B. Hjertager, *Comparing different CFD wind turbine modelling approaches with wind tunnel measurements*, *Journal of Physics: Conference Series* **555**, 012056 (2014).
- [19] M. Carrión, R. Steijl, M. Woodgate, G. N. Barakos, X. Munduate, and S. Gomez-Iradi, *Aeroelastic analysis of wind turbines using a tightly coupled CFD-CSD method*, *Journal of Fluids and Structures* **50**, 392 (2014).
- [20] S. C. Cakmakcioglu, I. O. Sert, O. Tugluk, and N. Sezer-Uzol, *2-D and 3-D CFD Investigation of NREL S826 Airfoil at Low Reynolds Numbers*, *Journal of Physics: Conference Series* **524**, 012028 (2014).
- [21] B. E. Launder and D. Spalding, *Lectures in Mathematical Models of Turbulence* (Academic Press, London, 1972).
- [22] M. Wolfshtein, *The Velocity and Temperature Distribution in one-dimensional flow with turbulence augmentation and pressure gradient*, *International Journal of Heat and Mass Transfer* **12**, 301 (1969).
- [23] T. Jongen, *Simulation and modeling of turbulent incompressible fluid flows*, Ph.D. thesis, EPFL Switzerland (1998).
- [24] R. Harder and R. Desmarais, *Interpolation using surface splines*, *Journal of Aircraft* **9**, 189 (1972).
- [25] J. T. Howlett, *Efficient self-consistent viscous-inviscid solutions for unsteady transonic flow*, *Journal of Aircraft* **24**, 737 (1987).

- [26] J. Edwards, *Transonic shock oscillations calculated with a new interactive boundary layer coupling method*, in *31st Aerospace Sciences Meeting* (American Institute of Aeronautics and Astronautics, Reno, Virginia, 1993) pp. AIAA-93-0777.
- [27] J. T. Batina, *Efficient algorithm for solution of the unsteady transonic small-disturbance equation*, *Journal of Aircraft* **25**, 598 (1988).
- [28] J. T. BATINA, *Unsteady transonic algorithm improvements for realistic aircraft applications*, *Journal of Aircraft* **26**, 131 (1989).
- [29] J. Hunt, A. Wray, and P. Moin, *Eddies, streams, and convergence zones in turbulent flows*, in *Studying Turbulence Using Numerical Simulation Databases, 2* (Center for Turbulence Research, Proceedings of the Summer Program 1988, 1988).
- [30] Y. Li, K. J. Paik, T. Xing, and P. M. Carrica, *Dynamic overset CFD simulations of wind turbine aerodynamics*, *Renewable Energy* **37**, 285 (2012).
- [31] Y. Zhang, T. Gillebaart, A. H. van Zuijlen, G. J. W. van Bussel, and H. Bijl, *Experimental and numerical investigations of aerodynamic loads and 3D flow over non-rotating MEXICO blades*, *Wind Energy* **20**, 585 (2017), [arXiv:arXiv:1006.4405v1](https://arxiv.org/abs/1006.4405v1) .
- [32] F. M. Najjar and S. Balachandar, *Low-frequency unsteadiness in the wake of a normal flat plate*, *Journal of Fluid Mechanics* **370**, 101 (1998).
- [33] O. Lehmkuhl, I. Rodríguez, R. Borrell, and A. Oliva, *Low-frequency unsteadiness in the vortex formation region of a circular cylinder*, *Physics of Fluids* **25**, 085109 (2013).

4

AEROELASTIC PREDICTIONS WITH ROMs

In Chapter 3, a high fidelity aeroelastic solver has been developed and applied to the three test cases - the NACA 0012 airfoil, the Goland wing and a wind turbine system. However, such solvers are computationally expensive and require long simulation times for predicting aeroelastic behaviour, for example, the wind turbine system considered here requires 362 CPU hours for each rotation of the turbine. As such, the solver cannot be used for applications such as design optimization and uncertainty quantification, since they require hundreds to thousands of runs of the simulation code, depending on the dimension of the system. To alleviate this problem, this chapter discusses the development of Reduced Order Models (ROM) to replace the expensive aerodynamic solver, which is then used to predict dynamic aeroelastic phenomena such as instabilities in aeroelastic systems. The single ROM derived to replace the aerodynamic solver can then be used for propagating uncertainties in the structural parameters. In this chapter, we discuss the development of ROMs - an ARX model and an LPV - ARX model in Sections 4.1 and 4.2. The aeroelastic solvers developed in Chapter 3 are used to generate data used to train the models, employing forced motion signals. Initially the ROMs are validated against the full CFD solver by reconstructing test signals. Further, the ROMs are expressed in the linear stability framework (Section 4.3) in order to obtain flutter boundary reconstructions (Section 4.4). Verification of the ROMs with test signals is also shown in Section 4.4. The wind turbine problem requires specific treatment for building accurate ROMs, hence the theoretical part and the results for wind turbine reconstructions are discussed separately in Section 4.5. These linear ROMs will be further employed in Chap-

ter 5 to propagate uncertainties and perform identification of the structural and rotational parameters of the wind turbine.

4.1. ARX MODEL

The ARX model is a time-marching method to predict the output of a system given observations and inputs affecting the system response, represented in the form of a recurrence relation. Details about the implementation of the algorithm are given in Appendix C. A Multi-Input-Multiple-Output (MIMO) system in terms of a generalized ARX model for an output quantity F_j and *exogenous* inputs q_1, q_2, \dots, q_{N_q} at time $t \in \mathbb{N}$ can be written as:

$$F_j^{(t)} = \sum_{i=0}^m a_1^{(i,j)} \ell^{-i} F_1^{(t-1)} + \sum_{i=0}^m a_2^{(i,j)} \ell^{-i} F_2^{(t-1)} + \dots + \sum_{i=0}^m a_{N_F}^{(i,j)} \ell^{-i} F_{N_F}^{(t-1)} \\ + \sum_{i=0}^n b_1^{(i,j)} \ell^{-i} q_1^{(t)} + \sum_{i=0}^n b_2^{(i,j)} \ell^{-i} q_2^{(t)} + \dots + \sum_{i=0}^n b_{N_q}^{(i,j)} \ell^{-i} q_{N_q}^{(t)}, \quad (4.1)$$

$\forall j \in \{1, \dots, N_F\}$, where a, b are model coefficients to be trained. The *lag* operator ℓ is introduced to time-shift the quantities, defined such that $q^{(t)} = \ell^h q^{(t-h)}$ for any time-dependent quantity. For all N_F output quantities, the system can be written in the vector form:

$$\mathbf{F}^{(t)} = \mathcal{A}_F(\ell) \mathbf{F}^{(t-1)} + \mathcal{A}_q(\ell) \mathbf{q}^{(t)}, \quad (4.2)$$

where $\mathbf{F} \in \mathbb{R}^{N_F}$ and $\mathbf{q} \in \mathbb{R}^{N_q}$ are the N_F outputs and N_q inputs respectively. The operators $\mathcal{A}_F(\ell)$, $\mathcal{A}_q(\ell)$ define the recurrence relation; their coefficient tensors A_F and A_q are defined by:

$$[A_F]_{ijk} = a_k^{(i,j)}, \quad i \in \{0, \dots, m\}, \quad j, k \in \{1, \dots, N_F\}, \\ [A_q]_{ijk} = b_k^{(i,j)}, \quad i \in \{0, \dots, n\}, \quad j \in \{1, \dots, N_F\}, \quad k \in \{1, \dots, N_q\}, \quad (4.3)$$

and are chosen by training the model against reference time-series data. The model orders m, n correspond to the number of past outputs and inputs considered. Under the assumption that the outputs are mutually independent, then many terms in A_F are zero, in particular:

$$a_k^{(i,j)} \equiv 0, \quad \text{if } j \neq k.$$

The model is entirely determined by the coefficient tensors A_F and A_q , which are estimated by training against input–output data obtained from CFD solver. Geometric motion is prescribed as $\mathbf{q}^{\dagger(t)} \in \mathbb{R}^{N_q}$ (exogenous inputs), and aerodynamic

forces $\mathbf{F}^{\dagger(t)} \in \mathbb{R}^{N_F}$ (outputs) are obtained. The \dagger terms represent the training data, which should be sufficiently plentiful and diverse to identify A_F , A_q . Training is based on the statistical model:

$$\hat{\mathbf{F}}^{(t)} = \mathcal{A}_F(\ell)\mathbf{F}^{\dagger(t-1)} + \mathcal{A}_q(\ell)\mathbf{q}^{\dagger(t)} + \epsilon^{(t)}, \quad (4.4)$$

where $\hat{\mathbf{F}}^{(t)} \in \mathbb{R}^{N_F}$ is the predicted output at time instant t . A Gaussian error term $\epsilon^{(t)} \in \mathbb{R}^{N_F}$ is introduced, assuming a white noise model and a least-squares problem is formulated to minimize $\epsilon^{(t)}$:

$$A_F, A_q = \underset{A_F, A_q}{\operatorname{argmin}} \sum_t \left(\mathbf{F}^{\dagger(t)} - \hat{\mathbf{F}}^{(t)} \right)^2. \quad (4.5)$$

The training signal \mathbf{q}^{\dagger} should excite a broad frequency range of the system. Here we employ *chirp* signals for training the dARX model - a representative chirp is shown in Figure 4.1, given by:

$$\alpha = \alpha_0 \sin(\omega(\tau)\tau), \quad (4.6)$$

where $\tau = \Delta t \cdot t$ (the symbol t in this chapter is always used as an index). Parameter α_0 is the amplitude, and $\omega(\tau) = \frac{\omega_1 - \omega_0}{\Delta t} \tau$, is known as the chirp rate with ω_1 , ω_0 and Δt as the final frequency, initial frequency and time-step respectively. The excitation frequency is based on the dominant structural frequencies obtained from a modal analysis. Thereafter, independent modal excitations for each mode are performed to obtain generalized aerodynamic forces.

The stability of the ARX system is based on the stability theory for recurrence relations. Equation (4.2) can be rearranged in terms of $\mathbf{F}^{(t)}$ to give the transfer function form:

$$\begin{aligned} \mathbf{F}^{(t)} &= \frac{\mathcal{A}_q(\ell)}{1 - \ell^{-1}\mathcal{A}_F(\ell)} \mathbf{q}^{(t)} \\ \mathbf{F}^{(t)} &= \mathcal{G}(\ell) \mathbf{q}^{(t)}. \end{aligned} \quad (4.7)$$

If and only if the poles of the transfer function $\mathcal{G}(\ell)$ lie within a unit circle in the z-plane, the system is stable. Once the stability of individual ARX models is assessed, the ARX theory can be used for defining a LPV model considering time varying coefficients. The stability of the LPV-ARX system is discussed further after introduction of the method in Section 4.2.

4.2. LPV-ARX MODEL FORMULATION

The ARX model is valid for the *scheduling parameter* at which it is trained. The scheduling parameter here refers to any operating parameter that may influence the response of the system, for example, Mach number can be considered

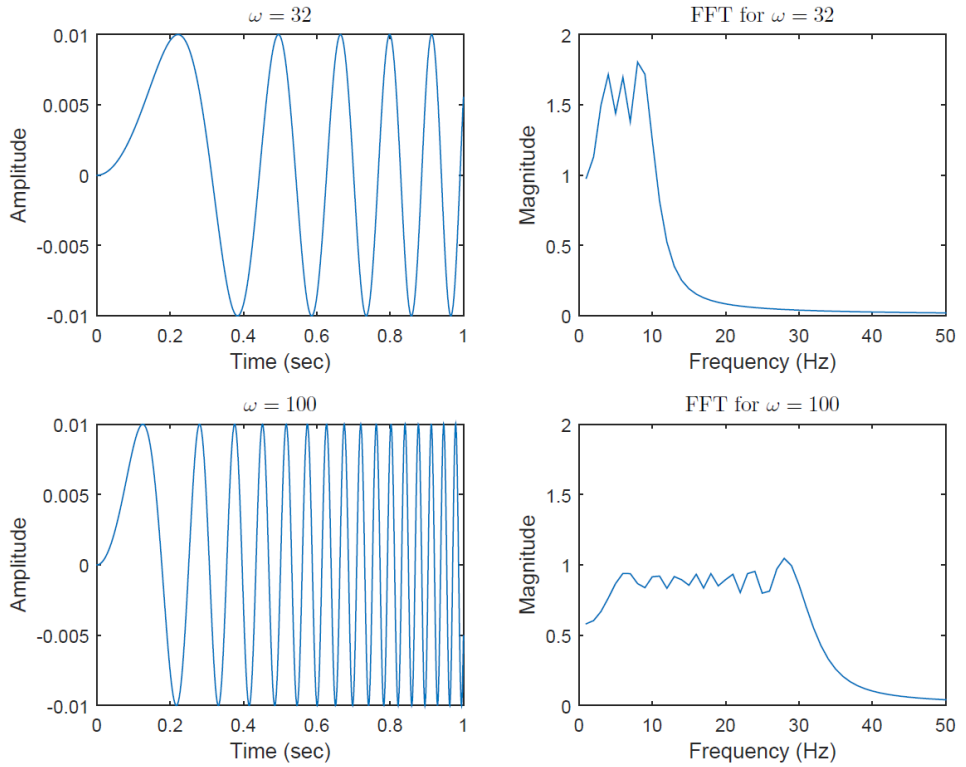


Figure 4.1: Two different chirp signals with their Fourier Transforms; power spectral density is checked to excite wide frequencies.

as scheduling parameter in case of flow problems. Due to change in this parameter, a new model has to be trained. This is particularly inconvenient for performing UQ on this parameter. The concept of LPV is utilized in this context, which originated from an older technique called gain-scheduling [1]. The method consists of an ARX model trained at each value of scheduling parameter, whose coefficients A_F , A_q are then interpolated to form an LPV model. The LPV model is thereby parametrised by the scheduling parameter M_∞ , which governs the dynamics relating the input and the output. We choose the Mach number as scheduling parameter for the current investigation.

The identification of the LPV-ARX system can be done in a local or a global manner. Global identification involves performing a single, long-running experiment with varying scheduling parameters. Local identification is based on interpolation of local linear-time-invariant (ARX) models, obtained at fixed scheduling parameters. In this work, a local identification approach based on [2–5] is employed. The local perspective is chosen for our aeroelastic application, primarily because the flow characteristics change significantly with Mach number. The coefficient tensors of ARX models are now expressed:

$$A_F(M_{\infty,j}), \quad A_q(M_{\infty,j}) \quad \forall j \in \{1, \dots, N_p\},$$

i.e. they are functions of Mach number estimated at N_p operating points ($M_{\infty,1}, \dots, M_{\infty,N_p}$), which provide the interpolation conditions.

The location of the interpolation points in LPV can be critical for the accuracy of the identified model as observed in [4], where an optimization procedure based on a ‘true’ LPV system is performed to select these points. This procedure can improve accuracy significantly [4] and make the identification optimal in terms of computational costs. In this work, though an initial estimate of the shape of the flutter boundary is known beforehand, the interpolation points are chosen uniformly. Considering the higher complexity in the transonic range and relatively smoother profile in the subsonic range, the points could be accordingly chosen, with more points in transonic range and comparatively coarser spacing in the subsonic range. However, another critical consideration is the degree and stability of the interpolating polynomial, suggesting such a sampling strategy should be combined with a piecewise polynomial approximation, e.g. cubic splines. Since the current investigation is focused on the use of the LPV framework in UQ, we defer such details for future research.

A Lagrange basis is introduced to approximate the expansion coefficients

$\hat{A}_F(M_\infty)$ and $\hat{A}_q(M_\infty)$ in the form:

$$\begin{aligned}\hat{A}_F(M_\infty) &= \sum_{j=1}^{N_p} A_F(M_{\infty,j}) L_j(M_\infty) \\ \hat{A}_q(M_\infty) &= \sum_{j=1}^{N_p} A_q(M_{\infty,j}) L_j(M_\infty)\end{aligned}\tag{4.8}$$

where, $L_j(M_\infty)$ are the Lagrange polynomials of degree $N_p - 1$ such that $L_i(M_{\infty,j}) = \delta_{ij}$, where δ_{ij} is the Kronecker delta. The interpolated coefficients for any operating point can then be used in (4.2) to estimate forces for any Mach number.

Stability for LPV systems can be defined in a global sense (stability for arbitrarily varying scheduling parameter) or in a frozen sense (fixed scheduling parameter) [1]. Certain interpolation methods [6] are able to guarantee global stability. On the other hand, frozen stability has been widely used in the control community, also with assumption of a slowly varying scheduling parameter [7]. In control applications, the scheduling parameter is expected to vary depending on the operational conditions. And such assumptions of slow variation is dependent on the specific problem being addressed. In the current investigation, the LPV-ARX coefficients are obtained by interpolating individual ARX models. During estimation of the stability of the aeroelastic system, the interpolated LPV-ARX model would in practise behave as an ARX model since the coefficients remain constant. This allows us to assess the stability of the LPV-ARX system as in (4.7). The concept of stability preserving interpolation methods as in [6] can as well be considered. However we do not pursue this further in this work and defer it for future investigations.

4.3. STABILITY ANALYSIS OF THE AEROELASTIC SYSTEM

The LPV-ARX model is analysed to approximate the linear stability boundary of the system, specifically the flutter boundary. Time-domain responses can be predicted to check the stability at an operating point - but this is unnecessary. Rather, we employ an eigenvalue-based approach [8]. The structural equation can be written in the form:

$$[M]\ddot{\mathbf{q}} + [C]\dot{\mathbf{q}} + [K]\mathbf{q} - \mathbf{F}_s = 0,\tag{4.9}$$

where $\mathbf{F}_s := T^T \mathbf{F}$ is the generalized aerodynamic load vector acting on the structural mesh, $[M]$ is the generalized mass matrix, $[C]$ is the damping matrix, $[K]$ is the stiffness matrix and \mathbf{q} represents the displacement vector. The state space

form of (4.9) is written as:

$$\begin{bmatrix} I & 0 \\ 0 & I \end{bmatrix} \begin{bmatrix} \dot{\mathbf{q}} \\ \ddot{\mathbf{q}} \end{bmatrix} - \underbrace{\begin{bmatrix} 0 & I \\ -M^{-1}K & -M^{-1}C \end{bmatrix}}_{A_s} \underbrace{\begin{bmatrix} \mathbf{q} \\ \dot{\mathbf{q}} \end{bmatrix}}_{\mathbf{x}_s} - \underbrace{\begin{bmatrix} 0 \\ M^{-1} \end{bmatrix}}_{B_s} \mathbf{F}_s = 0 \quad (4.10)$$

or

$$\dot{\mathbf{x}}_s = A_s \mathbf{x}_s + B_s \mathbf{F}_s. \quad (4.11)$$

The corresponding output equation can be written as:

$$\mathbf{y}_s = C_s \mathbf{x}_s + D_s \mathbf{F}_s \quad (4.12)$$

where, in this case $C_s = \mathbf{I}$, $D_s = 0$, \mathbf{y}_s is the output vector. These continuous time equations are converted to the discrete form:

$$\mathbf{x}_s^{(t+1)} = G_s \mathbf{x}_s^{(t)} + H_s \mathbf{F}_s^{(t)} \quad (4.13)$$

$$\mathbf{y}_s^{(t)} = C_s \mathbf{x}_s^{(t)} + D_s \mathbf{F}_s^{(t)}, \quad (4.14)$$

where, t is the time index, $\mathbf{x}_s^{(t)}$ is the state vector and $\mathbf{y}_s^{(t)}$ is the output vector. The delay operators in aerodynamic equation (4.2) in the state space form:

$$\mathbf{F}^{(t)} = \mathcal{A}_F(\ell) \mathbf{F}^{(t-1)} + \mathcal{A}_q(\ell) \mathbf{q}^{(t)} \quad (4.15)$$

are used to time-shift the output and input in order to define a discrete state vector \mathbf{x}_a at time index t given by:

$$\mathbf{x}_a^{(t)} = [\mathbf{F}^{(t-1)} \dots \mathbf{F}^{(t-n)} \mathbf{q}^{(t-1)} \dots \mathbf{q}^{(t-m)}]^T. \quad (4.16)$$

The state space form of the aerodynamic equation can then be written as:

$$\mathbf{x}_a^{(t+1)} = G_a \mathbf{x}_a^{(t)} + H_a \mathbf{q}^{(t)} \quad (4.17)$$

$$\mathbf{F}^{(t)} = C_a \mathbf{x}_a^{(t)} + D_a \mathbf{q}^{(t)}, \quad (4.18)$$

where, G_a , H_a , C_a and D_a are the coefficient matrices with terms from the tensors A_F and A_q , given by:

$$G_a = \begin{bmatrix} [A_F]_{1jk} & [A_F]_{2jk} & \dots & [A_F]_{(m-1)jk} & [A_F]_{mjk} & [A_q]_{1jk} & [A_q]_{2jk} & \dots & [A_q]_{(n-1)jk} & [A_q]_{(njk)} \\ \mathbf{I} & \mathbf{0} & \dots & \mathbf{0} & \mathbf{0} & \mathbf{0} & \mathbf{0} & \dots & \mathbf{0} & \mathbf{0} \\ \mathbf{0} & \mathbf{I} & \dots & \mathbf{0} & \mathbf{0} & \mathbf{0} & \mathbf{0} & \dots & \mathbf{0} & \mathbf{0} \\ \vdots & \vdots & \ddots & \vdots & \vdots & \vdots & \vdots & \ddots & \vdots & \vdots \\ \mathbf{0} & \mathbf{0} & \dots & \mathbf{I} & \mathbf{0} & \mathbf{0} & \mathbf{0} & \dots & \mathbf{0} & \mathbf{0} \\ \mathbf{0} & \mathbf{0} & \dots & \mathbf{0} & \mathbf{0} & \mathbf{0} & \mathbf{0} & \dots & \mathbf{0} & \mathbf{0} \\ \mathbf{0} & \mathbf{0} & \dots & \mathbf{0} & \mathbf{0} & \mathbf{I} & \mathbf{0} & \dots & \mathbf{0} & \mathbf{0} \\ \mathbf{0} & \mathbf{0} & \dots & \mathbf{0} & \mathbf{0} & \mathbf{0} & \mathbf{I} & \dots & \mathbf{0} & \mathbf{0} \\ \vdots & \vdots & \ddots & \vdots & \vdots & \vdots & \vdots & \ddots & \vdots & \vdots \\ \mathbf{0} & \mathbf{0} & \dots & \mathbf{0} & \mathbf{0} & \mathbf{0} & \mathbf{0} & \dots & \mathbf{I} & \mathbf{0} \end{bmatrix},$$

$$H_a = [[A_q]_{0,jk} \quad 0 \quad 0 \quad \dots \quad 0 \quad \mathbf{I} \quad 0 \quad 0 \quad \dots \quad 0], \quad D_a = [A_q]_{0,jk},$$

$$C_a = [[A_F]_{1,jk} \quad [A_F]_{2,jk} \quad \dots \quad [A_F]_{(m-1),jk} \quad [A_F]_{(m),jk} \quad [A_q]_{1,jk} \quad [A_q]_{2,jk} \quad \dots \quad [A_q]_{(n-1),jk} \quad [A_q]_{n,jk}].$$

Now the output \mathbf{y}_s of the structural equation (4.14) is fed as input to the aerodynamic equation after performing the transformation T given by IPS [9], which can be expressed as:

$$\mathbf{q}^{(t)} = T\mathbf{y}_s^{(t)}, \quad \mathbf{F}_s^{(t)} = T^T\mathbf{F}^{(t)}. \quad (4.19)$$

The coupled structural and flow equations in state space form are required for the aeroelastic analysis to form a coupled matrix to ascertain the stability of the system. The aerodynamic equation in terms of the structural output can be written as:

$$\mathbf{x}_a^{(t+1)} = G_a\mathbf{x}_a^{(t)} + H_aTC_s\mathbf{x}_s^{(t)} \quad (4.20)$$

$$\mathbf{F}^{(t)} = C_a\mathbf{x}_a^{(t)} + D_aTC_s\mathbf{x}_s^{(t)}. \quad (4.21)$$

Now the aerodynamic force is applied to the structural equation to obtain the displacements for the next time step. The forces also require transformation as given by (4.19) and are to be multiplied with the density ρ . Putting (4.20) and (4.21) in (4.13) and (4.14):

$$\begin{aligned} \mathbf{x}_s^{(t+1)} &= G_s\mathbf{x}_s^{(t)} + H_sT^T\rho C_a\mathbf{x}_a^{(t)} + H_sT^T\rho D_aTC_s\mathbf{x}_s^{(t)}, \\ &= (G_s + H_sT^T\rho D_aTC_s)\mathbf{x}_s^{(t)} + H_sT^T\rho C_s\mathbf{x}_s^{(t)}. \end{aligned} \quad (4.22)$$

The coupled form of equations is expressed in matrix form as:

$$\begin{bmatrix} \mathbf{x}_s^{(t+1)} \\ \mathbf{x}_a^{(t+1)} \end{bmatrix} = \underbrace{\begin{bmatrix} G_s + H_sT^T\rho D_aTC_s & H_sT^T\rho C_a \\ H_aTC_s & G_a \end{bmatrix}}_J \begin{bmatrix} \mathbf{x}_s^{(t)} \\ \mathbf{x}_a^{(t)} \end{bmatrix}. \quad (4.23)$$

The stability of this system is given by the stability theory for discrete linear systems. If $\hat{\Lambda}$ is an eigenvalue of the matrix J , then the system is stable if and only if all $|\hat{\Lambda}| < 1$.

4.4. VERIFICATION OF ROM AND AEROELASTIC ESTIMATES

Training (chirp) signals generated from the solver are used to train the LPV-ARX model. The training signals are forced motion signals prescribed to the structure which are expected to excite a broad frequency range of the system. The inputs (forced motion or generalised displacement) and the outputs (resulting force on the structure or generalised force) are used in developing the ROM. The trained model is then verified against sinusoidal test signals for aerodynamic reconstructions. Finally, the LPV-ARX model is coupled with the modal structural solver to compare the reconstruction of the flutter boundary against the CFD-obtained and experimental (airfoil)/numerical (Goland) findings.

4.4.1. TWO-DEGREE-OF-FREEDOM NACA 0012 AIRFOIL

VERIFICATION OF ARX ON SINUSOIDAL TEST SIGNALS (AERODYNAMICS ONLY)

For the airfoil, reference flutter frequencies are known from the experiment. Hence during the training phase, it is ensured that the training signal is able to excite at least these frequencies. In a more general test case where such information is not available, the excitation frequency domain has to be broad enough to encompass possible flutter frequencies. Figure 4.2a shows a typical arrangement of distribution of frequency content of chirp signals (up to 9Hz) and the test signals which lie within this bound (multiple signals at unit interval). Both single-mode and multi-mode excitations are performed. Depending on the obtained structural frequency per mode, the frequency range of the chirp signals are accordingly adjusted. The models trained by chirp signals are employed to reproduce sinusoidal test signals within the training frequency range. A Normalised Root Mean Square Error (NRMSE) [10] given by:

$$\epsilon_{NRMS} = 1 - \frac{\|\mathbf{F} - \hat{\mathbf{F}}\|}{\|\mathbf{F} - \mathbb{E}\mathbf{F}\|} \quad (4.24)$$

is used, where $\|\cdot\|$ is the 2-norm of a vector, $\hat{\mathbf{F}}$ and \mathbf{F} are the predicted and true output respectively and $\mathbb{E}\mathbf{F}$ is the mean value of the output. This estimate varies between $-\infty$ and 1, where a value of 1 corresponds to a perfect fit. Figure 4.2b shows ϵ_{NRMS} in reconstruction of lift coefficient (C_L) and moment coefficient (C_m) with sinusoidal test frequency under single-mode excitation (pitch and plunge separately), where the excited frequencies in the training signal are shown. It is observed that $\epsilon_{NRMS} \geq 0.92$ is obtained for test signals up to 9Hz, after which the predictions are inaccurate. This is very much in agreement with the frequencies excited by the chirp signals. A multi-mode excitation is also performed to assess the validity of the ARX models for multiple inputs. The contours in Figure 4.3 show the distribution of ϵ_{NRMS} under the excitation of pitch and plunge modes simultaneously. It is observed that $\epsilon_{NRMS} \geq 0.93$ is obtained for frequencies upto 9Hz. The frequency range agrees well with the single-mode excitation case. It can be concluded that the trained models provide good reconstructions of C_L and C_m in the frequency range of interest (flutter is expected to be in the range of 4–5 Hz from the BMP experiment). It should also be noted that the training frequency range is selected pertaining to the frequencies at which flutter is expected to occur. Hence the data used here for training is limited to these frequencies.

VERIFICATION OF LPV-ARX MODEL

We are interested in predicting the linear stability characteristics of the system especially the flutter boundary. The aeroelastic solver was earlier validated with

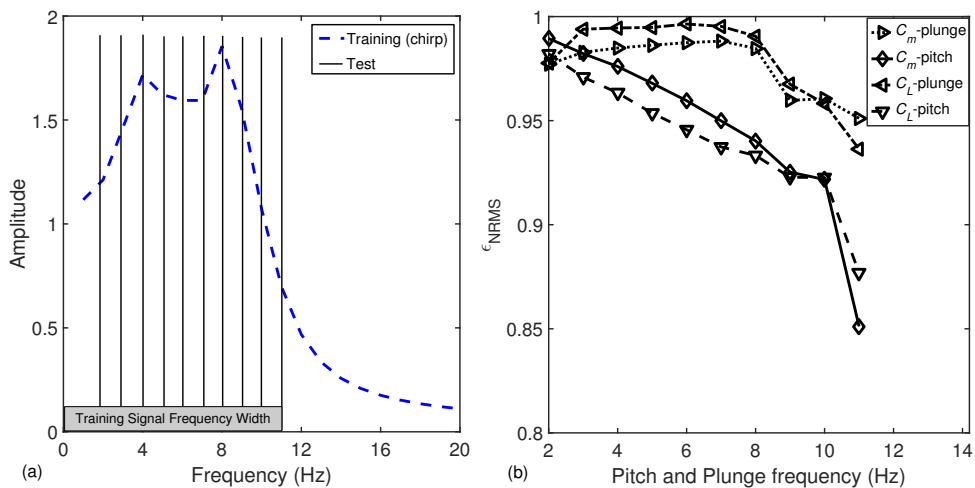


Figure 4.2: (a) Frequency overlap of training and test signals, (b) Error in reconstruction of test signals.

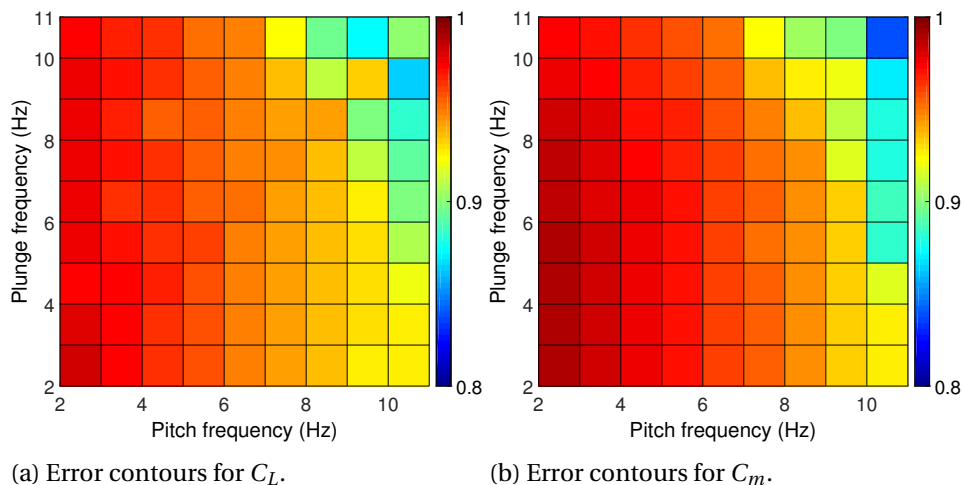
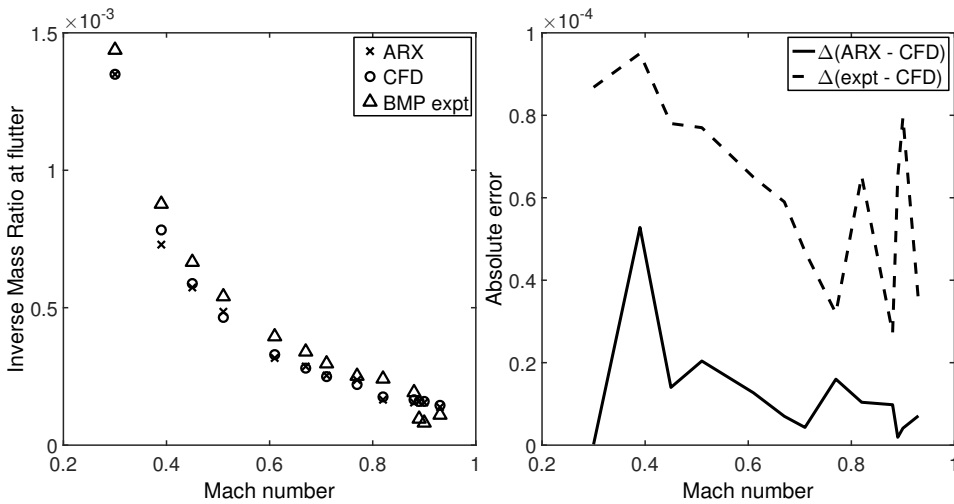


Figure 4.3: Error in reconstruction of test signals with 2-mode excitation.



(a) Comparison of estimated flutter bound- (b) Absolute error (ARX vs CFD) and (expt vs CFD).

Figure 4.4: Flutter boundary prediction for NACA0012 airfoil.

the findings in the BMP experiment (Figure 3.7a). The flutter boundary predicted by the LPV-ARX model is now added for comparing to the experimental and CFD estimations, which is shown in Figure 4.4a. The ARX models are first constructed at individual Mach numbers (inverse mass ratio at the unstable point), LPV-ARX model is interpolated from local ARX models, which is then used to predict the aeroelastic characteristics (inverse mass ratio at unstable point) of the airfoil. In terms of accuracy of the ROM, the estimations closely match the CFD results, with a maximum absolute percentage error of 7.27% within the Mach number range. The error trend of the CFD solver with the experiment is examined in Figure 4.4b, with low values of absolute errors predicted throughout the Mach number range. It is also interesting to note that absolute error between ROM and CFD is lower in comparison to that between the experiment and CFD, which show that our estimations are close to the CFD-predicted results. This validates the use of the ROM in lieu of the full CFD solver for prediction of instabilities.

4.4.2. GOLAND WING

VERIFICATION OF ARX (AERODYNAMICS ONLY)

As in the 2-DoF system, the individual modes of the Goland wing are trained independently. A normal mode decomposition of the structural model is performed to obtain the dominant modal frequencies and shapes. The first 4 struc-

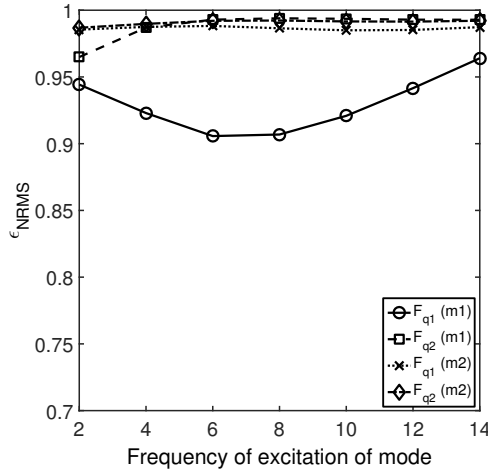


Figure 4.5: Error in reconstruction of first two modal forces F_{q1} and F_{q2} due to individual excitation of first 2 modes $m1$ and $m2$.

tural modes of the Goland Wing clean configuration were shown in Figure 3.3. The training of each of these modes is performed with chirp signals across a range of frequencies identified by the structural model.

The trained models are tested against sinusoidal test signals at overlapping frequencies with respect to the frequency content in the training (chirp) signal. All the aeroelastic results in case of Goland wing are obtained by considering the first 6 fundamental frequencies. We again report the model accuracy in terms of ϵ_{NRMS} given by (4.24). Figure 4.5 show the errors in the reconstruction of the test signals at frequencies excited by the training signal, for example $F_{q1}(m2)$ denotes the generalised force in mode 1 due to an excitation (forcing in terms of displacement) applied to mode 2. The first two generalized forces F_{q1} and F_{q2} as a result of excitation of modes $m1$ and $m2$ are shown. It is observed that the $\epsilon_{NRMS} \geq 0.9$ is obtained throughout the range of tested frequencies 2-14 Hz. Since flutter instability involves coupling of modes, the behaviour of the ROM under multiple-modal inputs should be estimated. Hence, reconstruction of modal forces due to multi-mode excitation is also investigated. Here, we discuss the first two modal forces F_{q1} and F_{q2} obtained due to excitation of first 2 modes. The sinusoidal test signals are excited at different frequency combinations in modes 1 and 2. These are plotted in the form of error contours in Figure 4.6. Normalised error $\epsilon_{NRMS} > 0.97$ is obtained throughout the training range in the reconstruction of first two modal forces F_{q1} and F_{q2} . The dynamic performance of the ROM for reconstruction of aerodynamic forces under multi-modal excitation is reasonably accurate. We now employ the model for estimating stability characteristics of

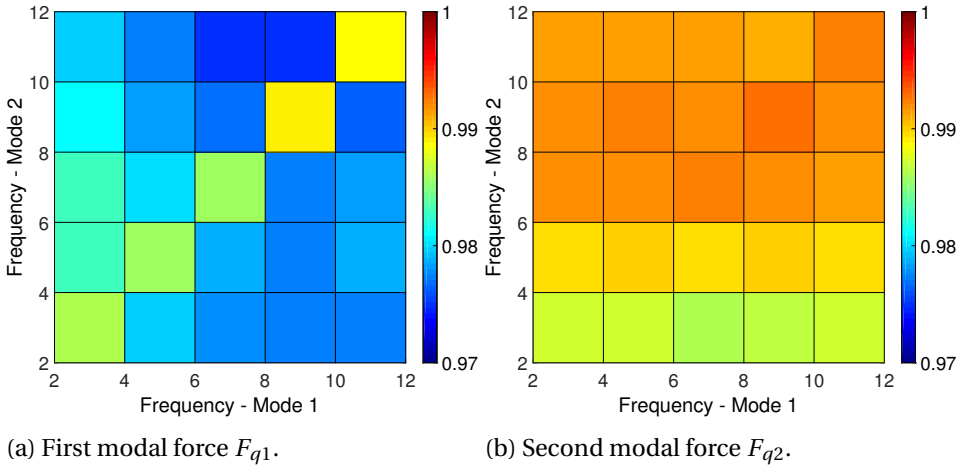


Figure 4.6: Contours of reconstruction errors of modal forces under multi-modal excitation.

Goland wing.

VERIFICATION OF LPV-ARX MODEL

The verification of the developed aeroelastic solver for estimating the flutter boundary of Goland wing is shown in Figure 3.7b by comparing to the predictions by the inviscid CAPTSDv solver used in Beran et. al. [11]. In Figure 3.7b, the flutter boundary is plotted on the $V_\infty - M_\infty$ plane. However for the current application, this would mean training the LPV-ARX for multiple scheduling parameters, namely V_∞ and M_∞ , thus necessitating more training points. Since the primary objective of the current investigation is to assess the reliability of the ROM for instability predictions, we use the ROM to predict the flutter boundary in the $\rho_\infty - M_\infty$ plane. This allows the use of a single scheduling parameter M_∞ .

Two versions of aeroelastic solvers are developed for the Goland wing problem - Euler-based and Navier-Stokes solvers. These are used to train two versions of ARX models to reconstruct the flutter boundary in the $\rho_\infty - M_\infty$ plane. The ARX models at discrete Mach numbers are interpolated to obtain LPV-ARX model for the entire operating regime as shown in Figure 4.7a. Four versions of the flutter boundary in terms of CFD and ROM solvers based on Euler and Navier-Stokes equations are shown. It can be observed that good agreement of the flutter density is obtained with respect to the CFD-predicted results for both the solvers. The relative errors in prediction are estimated for the Euler and viscous solver, which are shown in Figure 4.7b. The maximum relative error for both the cases is about 6%. Since the model is able to reconstruct aeroelastic behaviour reliably, the gain achieved in the computational costs is now assessed in the next section.

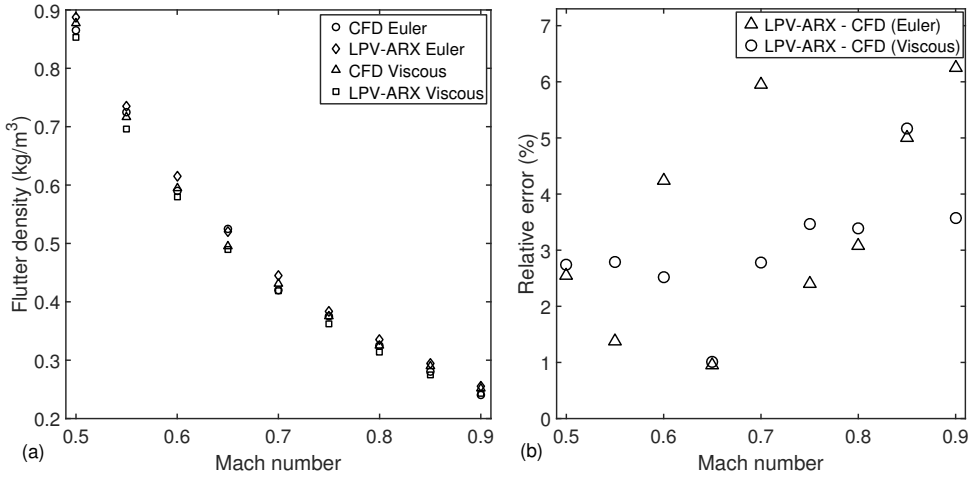


Figure 4.7: Flutter Boundary predicted by LPV-ARX models and relative error in reconstruction with respect to full solver, (a) CFD vs LPV-ARX in $\rho_\infty - M_\infty$ plane, (b) Relative error in the reconstruction by LPV-ARX with CFD.

4.4.3. COMPUTATIONAL GAIN WITH LPV-ARX

The LPV-ARX model is computationally almost free once trained. The training time is responsible for bulk of the computational expense in such models. Table 4.1 compares two approaches on the same machine. As already mentioned, the flutter point calculation with the CFD-based aeroelastic solvers is through a recursive bisection with a tolerance of 10^{-4} on the predicted flutter density. While a time integration upto 5s is performed for the CFD solver, the LPV-ARX estimation is based on an eigenvalue analysis (Section 4.3). As can be seen, the prediction phase of the LPV-ARX model is incredibly fast, since it is only based on estimation of eigenvalues. The bulk of the total expense in the presented method is attributed to the training signal generation, which is a critical phase in order to obtain reliable estimates from the ROM. With the presented methodology, the ROM needs to be trained only once for a certain Mach number, which allows us to propagate structural uncertainties cheaply. The use of the LPV-ARX framework utilises the interpolation procedure which further validates the ROM for a range of Mach numbers. We leverage this ability of the ROM in order to propagate structural/aerodynamic uncertainties in a subsequent chapter.

4.5. WIND TURBINE AEROELASTIC RECONSTRUCTIONS

The framework for the reduced order model (ROM) in the wind turbine problem is based on the same formulation as the NACA 0012 airfoil and Goland wing given by (4.2). However it is observed that the ROM used in airfoil and the Goland

Table 4.1: Computational time (in CPU-hours) required for prediction of a single flutter point for a given Mach number with Euler solver for Goland wing.

| | CFD | LPV-ARX |
|---|-----|---------|
| Training signal generation (with 6 modes) | 0 | 6 |
| Training time | 0 | 0.001 |
| Prediction of flutter point | 40 | 0.0002 |
| Total time | 40 | 6.0012 |

wing is not able to reconstruct the aeroelastic response accurately. Specifically, the mean response is reconstructed by (4.2), but the model is unable to predict the jump in moment introduced by the tower wake. This is expected since the tower wake introduces nonlinearity in the response, which is not predicted by the linear model. In order to improve the predictions, we introduce a localised forcing term $\mathbf{G}^{(t)}$ in (4.2) to form the model:

$$\mathbf{F}^{(t)} = \mathcal{A}_F(\ell)\mathbf{F}^{(t-1)} + \mathcal{A}_q(\ell)\mathbf{q}^{(t)} + \mathcal{A}_G(\ell)\mathbf{G}^{(t)}. \quad (4.25)$$

The localised forcing is in a Gaussian shape, which consists of a location parameter \mathbf{g} , which locates the tower wake position. In order to parametrise the rotation speed of the turbine, \mathbf{g} will be employed and incorporated in the UQ analysis in Chapter 5. For training the model as in the other two test cases, the blade is prescribed a motion given by $\mathbf{q}^{\dagger(t)} \in \mathbb{R}^{N_q}$ (exogenous inputs) and corresponding aerodynamic forces $\mathbf{F}^{\dagger(t)} \in \mathbb{R}^{N_F}$ (outputs) are obtained from the flow solver. The \dagger terms represent the training data, and as usual the data should be informative and plentiful in terms of frequencies and amplitudes-of-interest in order to identify A_F , A_q , A_G . One obvious choice is to employ *chirp* signals for training, given by (4.6). The excitation frequency for a particular system can be estimated based on the natural frequencies of vibration of the wind turbine blade, which can be obtained from the modal decomposition of the structure explained in Section 3.1.3. For each mode, independent modal excitations are performed to obtain corresponding generalized aerodynamic forces. A statistical model is constructed given by:

$$\hat{\mathbf{F}}^{(t)} = \mathcal{A}_F(\ell)\mathbf{F}^{\dagger(t-1)} + \mathcal{A}_q(\ell)\mathbf{q}^{\dagger(t)} + \mathcal{A}_G(\ell)\mathbf{G}^{\dagger(t)} + \epsilon^{(t)}, \quad (4.26)$$

where $\hat{\mathbf{F}}^{(t)} \in \mathbb{R}^{N_F}$ is the predicted output at time instant t . The Gaussian error term $\epsilon^{(t)} \in \mathbb{R}^{N_F}$ accounts for the discrepancy in prediction. A least-squares problem can be formulated to minimize $\epsilon^{(t)}$, given by:

$$A_F, A_q, A_G = \operatorname{argmin}_{A_F, A_q, A_G} \sum_t \left(\mathbf{F}^{\dagger(t)} - \hat{\mathbf{F}}^{(t)} \right)^2. \quad (4.27)$$

4.5.1. VERIFICATION OF ARX - RECONSTRUCTION OF FORCED MOTION

Verification of the ARX model for reconstruction of forced motion is performed, where sinusoidal test signals are used to specify the structural motion of the blades. In the coupled aeroelastic solver, the modal force, also known as the generalised force $Q_n(t)$ shown in (3.11), is used. This force is obtained by integration of the pressure throughout the blade surface, and then multiplying it with the modal matrix. During the training phase, $Q_n(t)$ is normalised as a pre-processing step. In Figure 4.8, the normalised generalised forces in blade 1 obtained from the full CFD solver and the ARX model are compared. The force reconstruction at TSR ≈ 1.6 and 6.3 for all the blades of the 3-bladed turbine is shown. The $\pi/3$ shift in the azimuthal position of the peak experienced in front of the tower can be observed in the three sets of estimations obtained from the three blades. It can be observed that the ARX solver is able to reconstruct the forces accurately close to the CFD predictions. The localised forcing term is also able to generate the trend in the peak encountered due to the tower wake. As explained in Figure 3.12, the change in TSR causes a change in the frequency and amplitude modulation of the low-frequency unsteadiness. It is seen that the localised forcing is able to reconstruct this behaviour with some discrepancy in the absolute value of the peaks, however the trend is clearly estimated.

4.5.2. VERIFICATION OF ARX FOR AEROELASTICS - ESTIMATION OF BLADE FORCING

After the verification of ARX through reconstruction of forced motion, we now employ the model to reconstruct unsteady aeroelastic forces. Several ARX models are built at fixed values of TSR and inflow conditions such as fixed velocity and air density. The ARX model is coupled to the modal structural solver and aeroelastic loads on the blades are predicted.

Figure 4.9 shows the estimation of the blade forcing at the two values of TSR and for each of the 3 blades. They are compared to the CFD-based aeroelastic results. It can be seen that the ARX model is able to reconstruct the trend of the aeroelastic forcing accurately. For the lower TSR ≈ 1.6 , we observe an offset in the absolute value of the mean forcing after the blade passes in front of the tower. However, at TSR ≈ 6.3 the offset is comparatively lower. This may be due to the introduction of the relatively stronger vortices from the tower wake (Figure 3.10b) at the reduced TSR, resulting in higher mean forcing in the CFD solver. This effect is not captured by the ARX model, since the training phase involves forced motion of the blades, which is hence unable to capture this effect which occurs only in the aeroelastic case. For an absolute agreement, the training of ARX has to be tailored by taking into account the phase shift between the forcing signal and the vortex generated by the tower. However, the model is able to

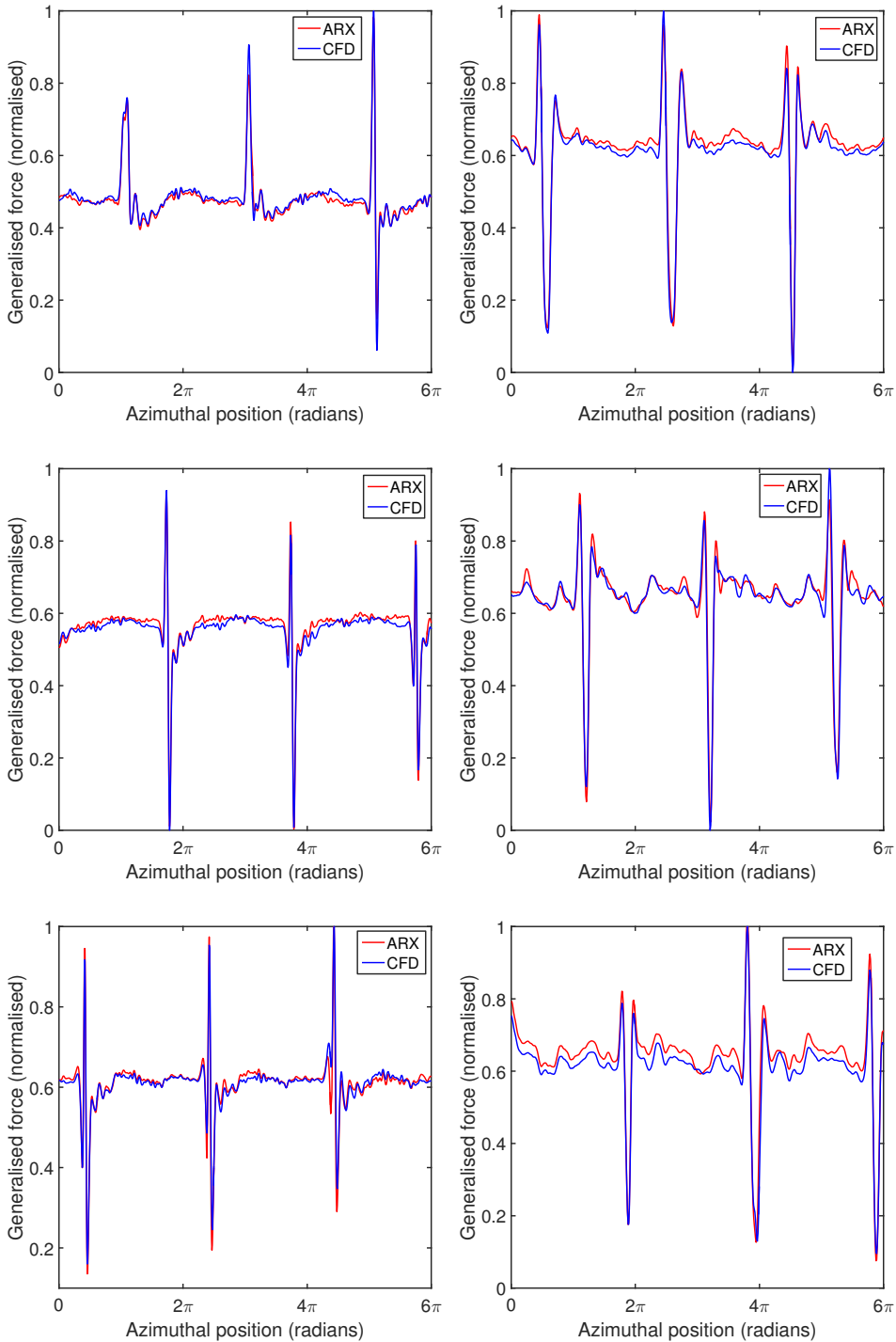


Figure 4.8: Generalised force (normalised) predicted by the ARX-based solver for sinusoidal forcing to the blades, compared to the CFD predictions for blade 1 (top), 2 (middle) and 3 (bottom) at $TSR \approx 1.6$ (left) and 6.3 (right).

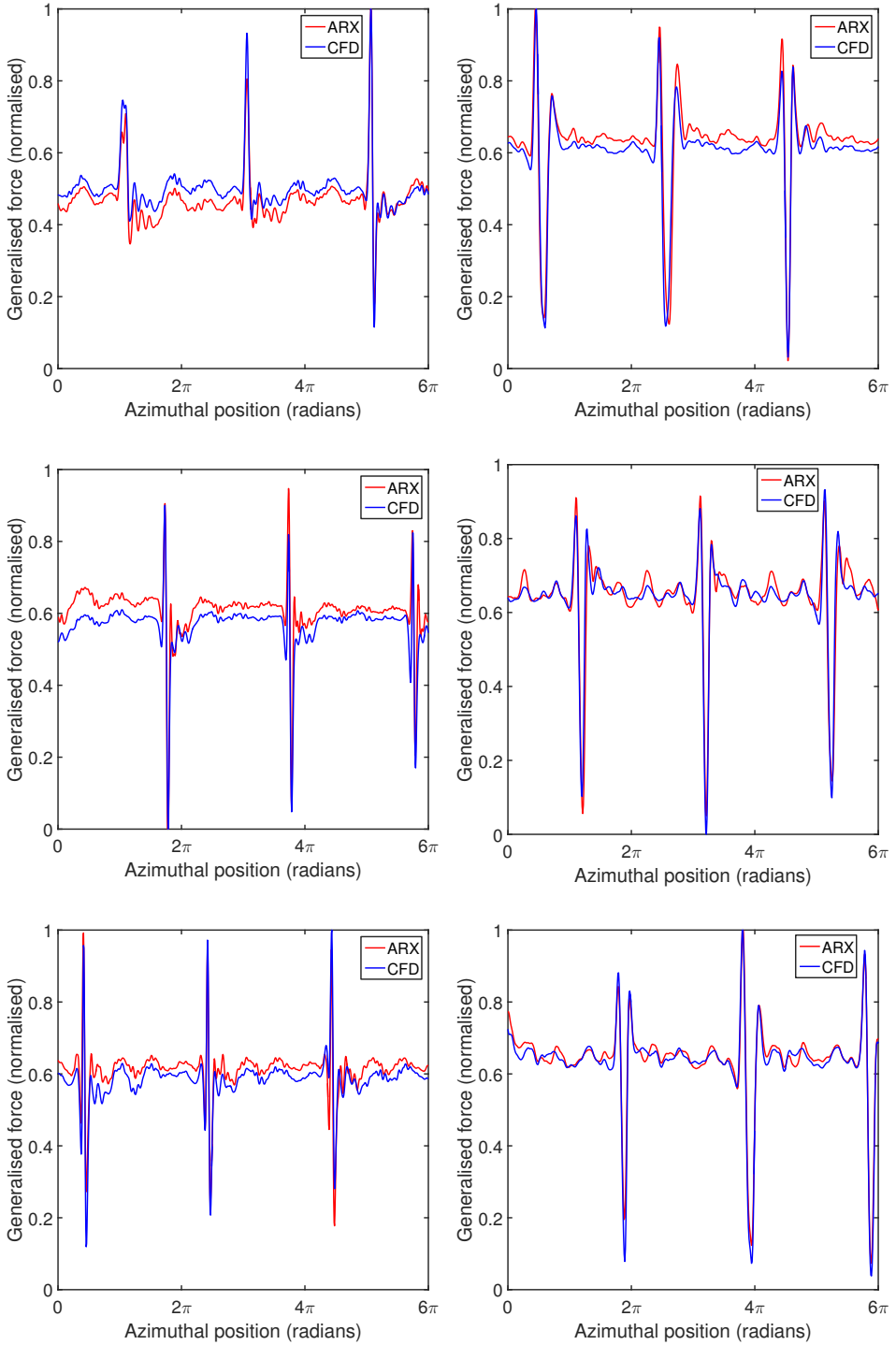


Figure 4.9: Generalised aeroelastic forces (normalised) predicted by the ARX-based solver compared to the numerical aeroelastic predictions for blade 1 (top), 2 (middle) and 3 (bottom) at TSR 1.6 (left) and 6.3 (right).

estimate the forcing introduced by the tower accurately.

4.6. SUMMARY

ROMs based on ideas of system identification have been developed for the three test cases that are investigated in this dissertation. The ROMs provide accurate unsteady aeroelastic characteristics and they have been verified based on CFD-obtained estimates. Utilising the computationally cheap estimations, in the next chapter we use this ROM in order to propagate uncertainties in the input parameters.

REFERENCES

- [1] R. Tóth, *Lecture Notes in Control and Information Sciences*, Vol. 403 (Springer-Verlag Berlin Heidelberg, 2010) pp. 2–3.
- [2] B. Bamieh and L. Giarré, *Identification of linear parameter varying models*, in *Proc. of the 38th Conf. on Decision and Control* (IEEE, 1999) pp. 1505–1510.
- [3] B. Bamieh and L. Giarré, *Identification of linear parameter varying models*, *International Journal of Robust and Nonlinear Control* **12**, 841 (2002).
- [4] A. A. Khalate, X. Bombois, R. Tóth, and R. Babuska, *Optimal experimental design for LPV identification using a local approach*, in *Proc. of the 15th IFAC Symposium on System Identification* (IFAC, 2009) pp. 162–167.
- [5] Q. Liu, J. Gross, S. Pfeiffer, and H. Werner, *A local approach for the LPV identification of an actuated beam using piezoelectric actuators and sensors*, *Mechatronics* **24**, 289 (2014).
- [6] D. J. Stilwell and W. J. Rugh, *Stability preserving interpolation methods for the synthesis of gain scheduled controllers*, *Automatica* **36**, 665 (2000).
- [7] H. H. Rosenbrock, *The stability of linear time-dependent control systems*, *Journal of Electronics and Control* **15**, 73 (1963).
- [8] K. K. Gupta and C. Bach, *Systems Identification Approach for a Computational-Fluid-Dynamics-Based Aeroelastic Analysis*, *AIAA Journal* **45**, 2820 (2007).
- [9] R. Harder and R. Desmarais, *Interpolation using surface splines*, *Journal of Aircraft* **9**, 189 (1972).

- [10] MATLAB, *Data Analysis—Regression Analysis*, in *Matlab 2016b* (The Mathworks Inc., 2016) pp. 3–11—3–15.
- [11] P. S. Beran, N. Khot, E. F.E., R. Snyder, J. Zweber, L. Huttzell, and J. Scott, *The Dependence of Store-Induced Limit-Cycle Oscillation Predictions on Modelling Fidelity*, U.S. Dept. of Defense, Defense Technical Information Center [ADA415759](#), 44 (2002).

5

REDUCTION OF UNCERTAINTIES EMPLOYING BAYES' THEOREM

The final part of this dissertation deals with the uncertainty quantification problem. In Chapter 3, we developed high fidelity aeroelastic solvers, which provide accurate estimates for the three test cases that have been investigated. In order to alleviate the computational burden of these solvers, we developed Reduced Order Models (ROM) in Chapter 4. These cheap models will now be utilized for performing uncertainty quantification.

The aim of this chapter is to provide probabilistic estimates on aeroelastic characteristics and then use Bayesian techniques and experimental data in order to reduce the uncertainties. Linear instabilities or dynamic aeroelastic behaviour is estimated and the linear ROMs developed in Chapter 4 will be used for two aeroelastic systems – Goland wing and the experimental wind turbine. Initially, uncertainties are assumed for defining priors and (artificial/experimental) data is generated/used to identify the input parameters. Section 5.1 provides the methodology for the propagation problem and the framework for applying Bayesian inference. Application to the test case of Goland Wing is provided in Section 5.2, while the wind turbine problem is discussed in Section 5.3 along with identification of structural and rotational parameters using experimental data.

5.1. UNCERTAINTY PROPAGATION AND BAYESIAN UPDATING

We investigate the effect of epistemic uncertainty in structural and aerodynamic parameters on aeroelastic characteristics such as the location of the flutter boundary or the blade bending moment. Two test cases are considered - Goland wing and the experimental wind turbine. For the Goland wing, structural param-

eters \mathbf{s} are uncertain and the probabilistic flutter boundary is located by checking for the unstable eigenvalue at the corresponding density. While in case of wind turbine, the effect of \mathbf{s} and localised forcing terms \mathbf{g} on the generated structural moment is investigated. This framework uses Bayes' theorem [1]:

$$\mathbb{P}(\mathbf{s}, \mathbf{g} | \Lambda) \propto \mathbb{P}(\Lambda | \mathbf{s}, \mathbf{g}) \cdot \mathbb{P}_0(\mathbf{s}) \cdot \mathbb{P}_0(\mathbf{g}),$$

where Λ is the experimental data (aeroelastic measurements (eigenvalues) for the Goland wing and experimental structural moment measurements for the wind turbine), and parameters \mathbf{s} and \mathbf{g} are to be identified. $\mathbb{P}_0(\mathbf{s})$ and $\mathbb{P}_0(\mathbf{g})$ are the *prior* distributions, chosen based on any previously available information and expert opinion. $\mathbb{P}(\Lambda | \mathbf{s}, \mathbf{g})$ is the *likelihood* derived from a statistical model describing the relationship of the simulation predictions to the experimental observations and it represents the difference between the experimental data and simulation model. At least experimental noise should be accounted for here, whose magnitude is known from the experimental data in case of the wind turbine. Finally $\mathbb{P}(\mathbf{s}, \mathbf{g} | \Lambda)$ is the *posterior*, which in this framework is the answer to the question: What is known about the values of \mathbf{s}, \mathbf{g} ?

In the absence of experimental data for the Goland wing, we use numerical data from the Navier-Stokes solver with artificially introduced noise. The data in the current investigation always refers to stability eigenvalues at sub-critical conditions (i.e. densities/Mach numbers without flutter). Finally a posterior predictive distribution (ppd) of the flutter density is obtained from the propagated posteriors.

During the uncertainty propagation, we also take into account the effect of change in the structural modal matrix with change in structural parameters. The initial ARX model (4.2) is based on training with the mode shapes ϕ_s , obtained from the deterministic structural parameter values \mathbf{s} . However these mode shapes will vary for each sample $\hat{\mathbf{s}}$ that is drawn from the probability space, which will change both the generalized displacements \mathbf{y}_s and the generalized aerodynamic load vector \mathbf{F}_s . We incorporate this effect by constructing a new modal matrix $\hat{\phi}_s$ for $\hat{\mathbf{s}}$, which is then used to find the modal deformations in terms of ϕ_s to be used in the ARX model. Explicitly, if $\hat{\mathbf{y}}_s$ denotes the generalized displacement for $\hat{\mathbf{s}}$, we solve the minimization problem $\hat{\phi}_s \hat{\mathbf{y}}_s = \phi_s \mathbf{y}_s$ for \mathbf{y}_s to be used in the aerodynamic equation. Similarly, the generalized force $\hat{\mathbf{F}}$ for $\hat{\mathbf{s}}$ is obtained from $(\hat{\phi}_a^T)^{-1} \hat{\mathbf{F}} = (\phi_a^T)^{-1} \mathbf{F}$, where ϕ_a is the modal matrix for the aerodynamic mesh. In this manner, the trained ARX model based on the baseline model can still be used for estimating the aerodynamic forces; hence efficiency of the ROM is not affected. The steps for the uncertainty analysis are detailed in following sections.

5.1.1. DEFINING AND PROPAGATING PRIORS ON THE STRUCTURE

In defining structural uncertainty, our goal is to obtain a probabilistic estimate on the aeroelastic characteristics of the system. In case of the Goland wing, based on the high sensitivity of this stability boundary to the structural parameters [2] and lack of knowledge of the deterministic values of these parameters, we achieve bounds on the boundary by uncertainty propagation through the cheap LPV-ARX model. In the preliminary UQ problem for the Goland wing, also aerodynamic (Mach number M_∞) uncertainty is considered. Let $\bar{\mathbf{s}}$ be the mean (also deterministic/nominal) values of the structural parameter vector. Additionally for the wind turbine, let $\bar{\mathbf{g}}$ be the mean of the the localised forcing term. In the absence of more specific information, we assume uniform probability densities, for example with $\pm 10\%$ and $\pm 1\%$ variation about $\bar{\mathbf{s}}$ and $\bar{\mathbf{g}}$, we get:

$$\mathbf{s} \sim \mathcal{U}(0.9\bar{\mathbf{s}}, 1.1\bar{\mathbf{s}}), \quad \mathbf{g} \sim \mathcal{U}(0.99\bar{\mathbf{g}}, 1.01\bar{\mathbf{g}}).$$

The assumption of a uniform prior could be replaced with uncertainty based on expert opinion obtained via Bayesian elicitation [3]. Incorporation of other density functions is straightforward within this methodology, as the cheap ARX model allows us to use Monte Carlo in the input probability space. For the Goland wing, we obtain eigenvalues of the matrix J in (4.23) for each sample from the prior distribution and r largest eigenvalues are stored in $\Lambda \in \mathbb{C}^r$. While in case of wind turbine, the structural moment history with respect to the azimuthal position of the blade is obtained. The numerical approximation of eigenvalues of J as obtained from (4.23) or the structural moment from (4.25) can be written in the form:

$$\hat{\Lambda} := \begin{cases} \hat{\Lambda}(\mathbf{s}; \rho) & \text{for Goland wing} \\ \hat{\Lambda}(\mathbf{s}, \mathbf{g}) & \text{for wind turbine.} \end{cases} \quad (5.1)$$

The density at free-stream conditions ρ_∞ is related to M_∞ by $M_\infty = \frac{V_\infty}{\sqrt{\gamma P_\infty / \rho_\infty}}$, where γ is the specific heat ratio and P_∞ is the pressure. The LPV-ARX/numerical estimate of flutter density $\rho_{\text{flutter}} \in \mathbb{R}$ is the solution of:

$$\max_i |\hat{\Lambda}_i(\mathbf{s}; \rho_{\text{flutter}})| = 1. \quad (5.2)$$

This provides us probabilistic estimates on the flutter density or the structural moment history and we will see later that for these priors and the cases considered, the estimated uncertainty is significant. The Bayesian framework is now introduced in order to identify the input parameters from data, and thereby reduce this uncertainty.

5.1.2. BAYESIAN UNCERTAINTY REDUCTION USING DATA

Let $\Lambda^+ \in \mathbb{C}^r$ be a *measured* value of the eigenvalue vector at density ρ^+ or the structural moment vector. Eigenvalues Λ^+ are related to the structural model employing (5.1) and an additive random variable ε , specified as an unbiased normal distribution assuming independent noise $\Sigma = \sigma_\Lambda^2 I$ is used to account for noise in the measurements. In case of the wind turbine, the full covariance matrix Σ is obtained from the experimental data (due to the moments reported for repeated runs or rotations of the turbine), which is used in the likelihood estimation. We neglect systematic modelling errors for the current investigation as in [4]. This gives the statistical model:

$$\Lambda^+ = \hat{\Lambda}(\mathbf{s}; \rho^+) + \varepsilon \quad (5.3)$$

$$\varepsilon \sim \mathcal{N}(0, \sigma_\Lambda^2), \quad (5.4)$$

which gives the probability of observing Λ^+ given \mathbf{s} , also known as the likelihood as:

$$\mathbb{P}(\Lambda^+ | \mathbf{s}, \rho^+) := \mathbb{P}_\varepsilon(\Lambda^+ - \hat{\Lambda}(\mathbf{s}; \rho^+)). \quad (5.5)$$

For the wind turbine, the likelihood can be written as:

$$\mathbb{P}(\Lambda^+ | \mathbf{s}, \mathbf{g}) := \mathbb{P}_\varepsilon(\Lambda^+ - \hat{\Lambda}(\mathbf{s}, \mathbf{g})). \quad (5.6)$$

5.1.3. EXPLICIT EXPRESSION FOR POSTERIOR OF FLUTTER DENSITY

The prior $\mathbb{P}_0(\mathbf{s})$ defined initially on the structural parameters can be now updated with the likelihood given by (5.5) with Bayes' theorem to obtain the posterior:

$$\mathbb{P}(\mathbf{s} | \Lambda^+, \rho^+) \propto \mathbb{P}(\Lambda^+ | \mathbf{s}, \rho^+) \mathbb{P}_0(\mathbf{s}), \quad (5.7)$$

$$\propto \exp \left[-\frac{1}{2} \frac{\sum_{i=1}^r (\Lambda_i^+ - \hat{\Lambda}_i(\mathbf{s}; \rho^+))^2}{\sigma_\Lambda^2} \right] \mathbb{P}_0(\mathbf{s}). \quad (5.8)$$

Similarly an expression for the posterior considering the covariance matrix can be written down for the wind turbine. The distribution is sampled using Metropolis-Hastings (MH) Markov Chain Monte-Carlo (MCMC) algorithm [5]. The MH algorithm samples the posterior distribution, using a reversible Markov random-walk, with each step selected from a proposal distribution. The particular implementation used here cycles through each component of s and g , changing only one at a time, with a normal proposal distribution, whose variance is tuned during the run. The total number of steps in the chain is 10000, wherein the first 1000 samples were discarded in a *burn-in* period, and the remaining samples thinned by a factor of 2 to improve the independence of consecutive samples. Standard checks of MCMC convergence were applied [5, 6].

5.2. UQ AND BAYESIAN UPDATING - GOLAND WING

The viscous version of the LPV-ARX model is used in this section. In the preliminary UQ problem, the 7-parameter structural input $\mathbf{s} \in \mathbb{R}^7$ and the Mach number M_∞ are assumed to be distributed uniformly $\pm 10\%$ about the nominal values $\bar{\mathbf{s}}$ and \bar{M}_∞ . Figure 5.1 shows the variation of the magnitude of the dominant eigenvalue with density at Mach number 0.9. The lines correspond to the probability of the eigenvalue exceeding the corresponding line at fixed ρ . Thus under the assumed uncertainties, there will never be flutter if $\rho < 0.2219$ and there will always be flutter if $\rho \geq 0.3008$, which represents a large uncertainty in flutter altitude of $\sim 2000\text{m}$.

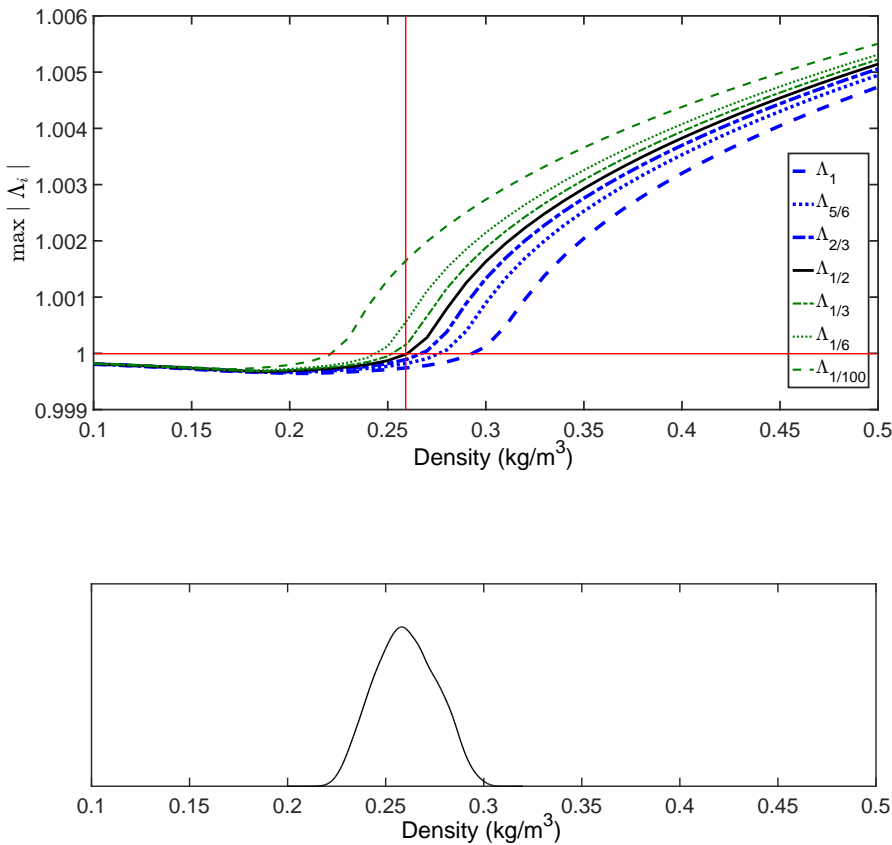


Figure 5.1: Change in the dominant eigenvalue with density at Mach 0.9 with structural uncertainties, where $\Lambda_j \mid \mathbb{P}(\Lambda > \Lambda_j) = j$. The uncertainty in the flutter density ($|\Lambda| = 1.0$) is shown in the pdf below.

To reduce this uncertainty, experimental data is used to identify the struc-

tural parameters through Bayesian updating. For this, a twin problem is set-up to generate data in the absence of real experimental data. A random sample $\mathbf{s}_{\text{truth}}$ is drawn from $\mathbb{P}(\mathbf{s})$. The artificial measurement data are then obtained from the CFD solver as:

$$\Lambda^+ = \hat{\Lambda}(\mathbf{s}_{\text{truth}}; \rho^+) + \varepsilon. \quad (5.9)$$

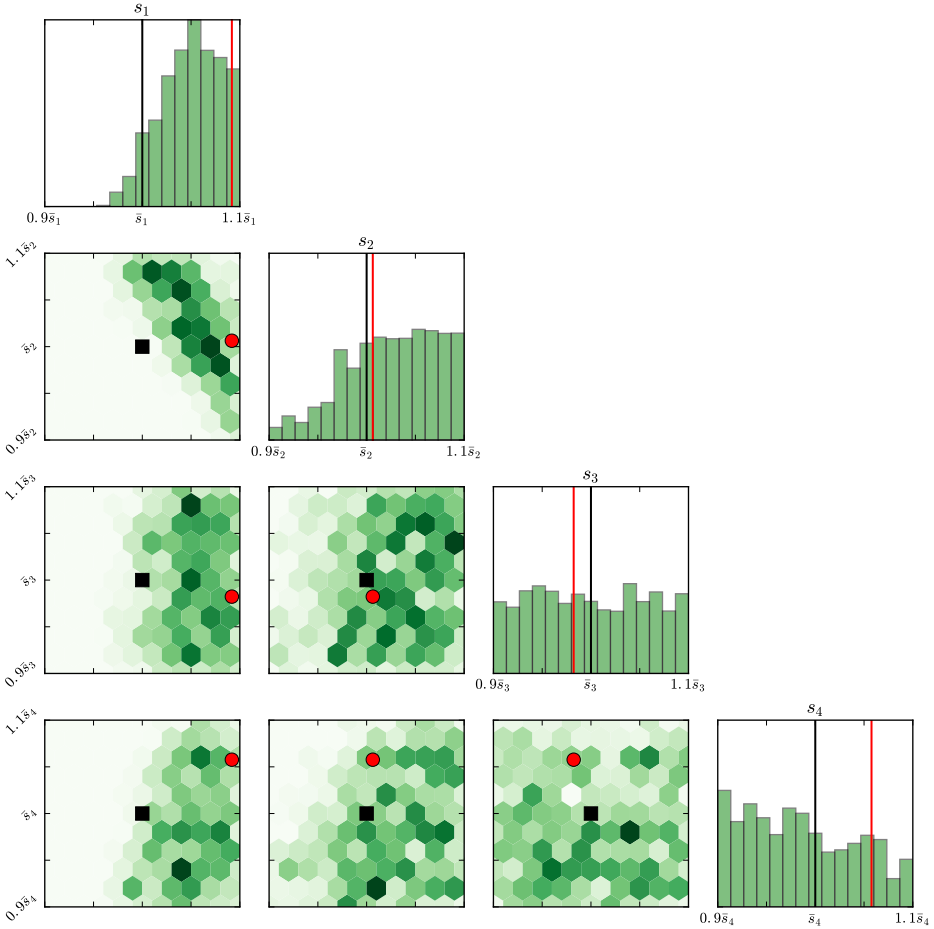


Figure 5.2: Posterior distributions with 1-d histograms of each parameter \mathbf{s} and 2-d scatter plots for each parameter-pair for $\rho^+ = 0.27$ and $\sigma_\Lambda = 0.0001$ for Goland wing. Black lines and squares show mean value of parameters $\bar{\mathbf{s}}$ and red lines and circles show true value of the parameters $\mathbf{s}_{\text{truth}}$

The additive noise is sampled from an unbiased normal distribution with known variance given by $\varepsilon \sim \mathcal{N}(0, \sigma_\Lambda^2)$. Figure 5.2 shows 1-d marginal posterior

histograms for each parameter, and 2-d marginal histograms for each parameter pair. The 1-d marginals indicate the specificity of posterior knowledge of each parameter in isolation. We can see that the parameters s_1 and s_2 have been somewhat identified as they are skewed towards their maximum values (we assumed uniform distributions initially). The 2-d marginal plots provide correlation information - where we can see that s_1 and s_2 are strongly correlated with a negative gradient. This suggests that the experimental observations can be obtained by either increasing the thickness of s_1 (leading/trailing edge spar) or s_2 (upper/lower skin element), or some combination of the two. In contrast parameter s_3 (area of leading/trailing edge spar) and s_4 (area of center edge spar) have not been identified at all - the posterior is almost indistinguishable from the prior. This is not surprising given that only (scalar) measurement is used in the calibration, leading to a highly underdetermined inverse problem. However, even then the flutter uncertainty has been substantially reduced as seen in Figure 5.3, thus implying that the measurements are informative about this and identification of correlation between parameters s_1 and s_2 is able to reduce the uncertainty in flutter density.

A parametric study is also performed on the effect of the location of the measured data (given by ρ^+) and σ_Λ , shown in Figure 5.3. It is observed that as measurement density ρ^+ moves closer to the true flutter density, there is a reduction in the variance of the ppd of the flutter density and the predicted mean density moves closer to the true density. Similarly a smaller variance on the measurement noise σ_Λ results in denser estimates on the flutter density. A measurement point at $\rho^+ = 0.27$ and $\sigma_\Lambda = 0.0001$ gives a ppd estimate on flutter density almost identical to the true density. This method can be used to utilize flutter test data to update the probability bounds on the instability boundary.

5.3. UQ AND BAYESIAN UPDATING - WIND TURBINE

5.3.1. PROPAGATION OF INPUT UNCERTAINTIES

The structural parameters of the wind turbine that are considered uncertain are the distribution of mass, Young's modulus and moments of inertia in two directions. In the experimental data of the wind turbine, these properties are specified at different chord locations of the blade. During uncertainty propagation, the structural parameters at these locations are considered as uncertain employing multivariate distributions with a covariance operator. Since the use of the ROM enables computationally cheap aeroelastic estimations, these uncertainties can be propagated with brute-force Monte Carlo method.

Besides structural uncertainty, the rotational speed of the wind turbine is also found to be uncertain from the experimental measurements, as already dis-

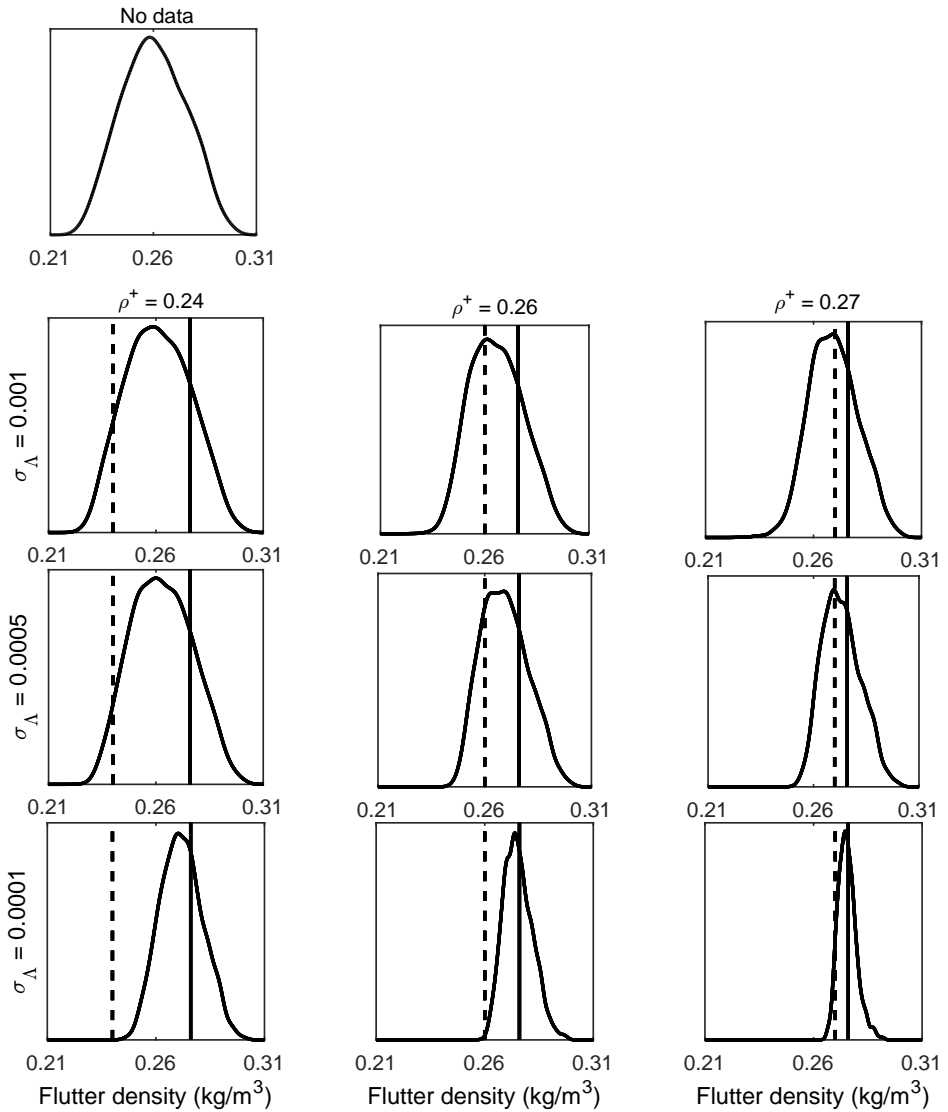


Figure 5.3: ppds of flutter density for Goland wing under different σ_Λ and ρ^+ . Vertical solid line: true flutter density. Vertical dotted line: measurement density ρ^+ .

cussed in Chapter 3. This uncertainty is introduced through the location of the tower forcing terms \mathbf{g} . We first investigate the effect of the structural uncertainty on the structural moment of the turbine. Thereafter, the effect of uncertain tower forcing is ascertained, and finally all the uncertainties are combined to form a realistic prior for the Bayesian identification problem.

Figures 5.4-5.6 show the confidence intervals for the two output quantities of interest - normalised generalised force and structural moment at 30%-span location. For the structural uncertainty cases, the generalised forces are also plotted in order to demonstrate the relative effect on the two output quantities. The confidence intervals are plotted for 1, 2 and 5% variation (shown by the gray shaded area) in the structural parameters with respect to the mean (deterministic) values (shown by the black solid line). For other blades, the confidence intervals of the two output quantities are shown in Appendix A. One common observation from all the propagations is the difference between the response surfaces of the structural moment (captioned as (a) to the left) and the generalised force (captioned as (b) to the right) under the same variation in the input parameters. In case of generalised force in the blade, the variability introduced by uncertain input is relatively less, since the forcing introduced by the tower wake dominates the response. Also there is a direct effect of the uncertain structural input on the structural moment, while the effect is indirect on the generalised force.

The variation of the structural moment is due to the change in aeroelastic frequency of vibration of the blade, introduced by the change in the structural properties of the blade. This effect is however neutralised as the blade approaches the tower and is subjected to the wake forcing. This can be clearly observed in responses from higher variability in the input forcing, such as Figure 5.5a for 2% variability in input parameters. The tower forcing is introduced at around 1.5π azimuthal position. The uncertain response has a staggered distribution around the mean, which can be observed from the crests and troughs of the harmonic response. The shaded area (uncertain response) in the crest after the 1.5π azimuthal position is symmetric about the mean in terms of the frequency, while the variation is only in terms of difference in amplitude. The effect of the tower wake thus collapses the frequency change introduced by the uncertain inputs. For the case with 5%- variation (Figure 5.6), the uncertain response for structural moment has a significant spread due to the larger change in structural frequency. This large uncertain response with 5%- variation is considered to be large for the current investigation.

In the next step, rotational uncertainty is introduced by considering the location of the localised forcing term to be uncertain. Figures 5.7a and 5.7b show the uncertain response in the structural moment for 1% and 2%- variation in the localised forcing term respectively. It is observed that the localised forcing

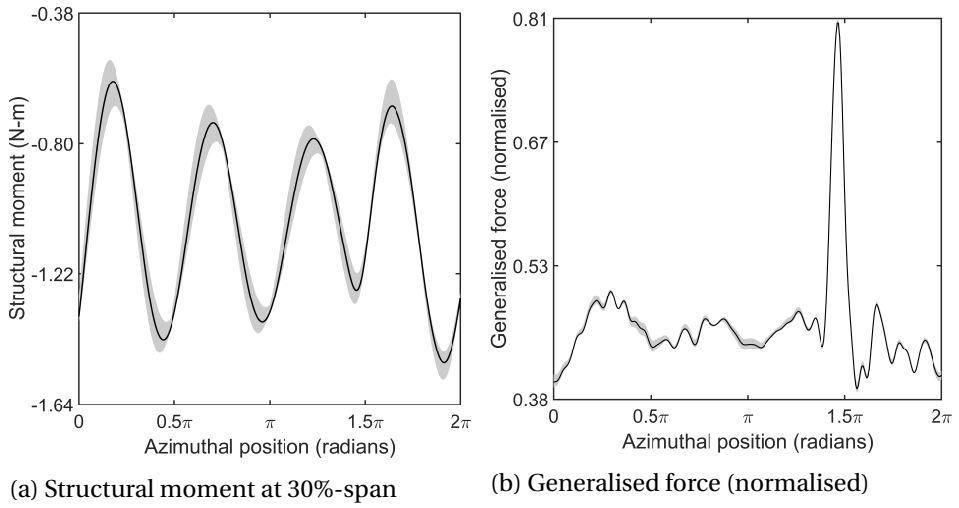


Figure 5.4: Confidence intervals for blade 1 at $\text{TSR} \approx 1.55$ assuming uniformly distributed input parameters - Blade sectional distribution of Mass, Young's modulus, moments of inertia I_x and I_y with 1% variation.

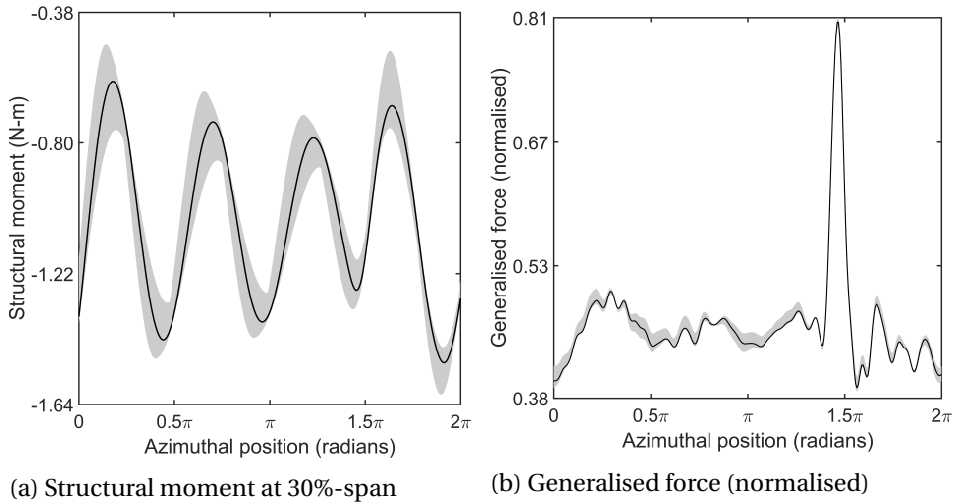


Figure 5.5: Confidence intervals for blade 1 at $\text{TSR} \approx 1.55$ assuming uniformly distributed input parameters - Blade sectional distribution of Mass, Young's modulus, moments of inertia I_x and I_y with 2% variation.

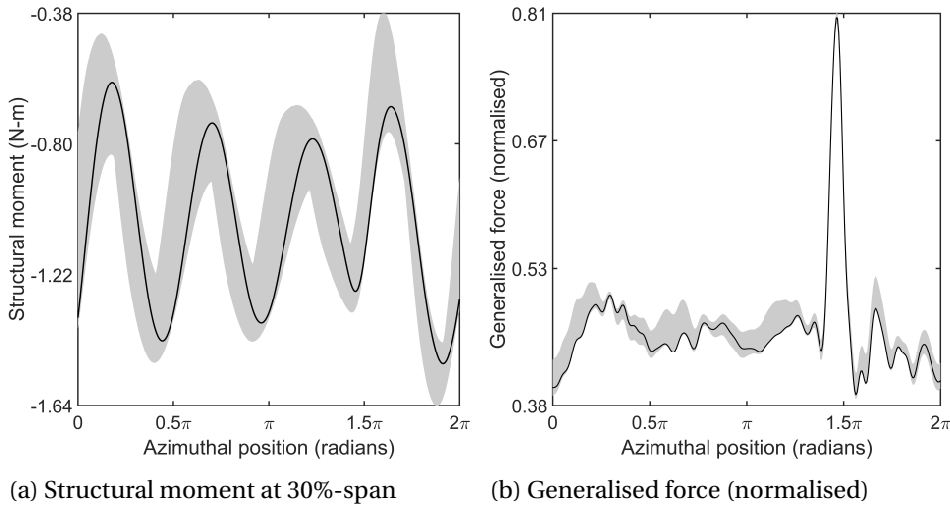


Figure 5.6: Confidence intervals for blade 1 at $\text{TSR} \approx 1.55$ assuming uniformly distributed input parameters - Blade sectional distribution of Mass, Young's modulus, moments of inertia I_x and I_y with 5% variation.

uncertainty introduces larger spread in the response of the blade moment after the 1.5π azimuthal position. This is expected since the localised forcing term takes into account the forcing from the tower wake and the rotational uncertainty would in turn result in a phase shift in the incidence of the tower wake. When 2% variation is considered (Figure 5.7b), the spread is comparatively large leading to significant difference with respect to the experimentally observed uncertainties.

In the final propagation problem, both the structural and localised forcing uncertainties are considered, the corresponding blade moment response is shown in Figure 5.8. As already discussed, for the localised forcing term, 1% variation is considered. For the structural parameters, both 1% and 2% variations are considered. The structural moment response is found to be symmetrical about the mean location. This uncertain response is in agreement with the experimentally observed uncertainties - hence the considered uncertainties in this investigation are close to physically observed response. In order to consider for the higher spread in the response around the 1.5π azimuthal position, we consider 2% and 1% variation in the structural and tower forcing terms respectively in the Bayesian identification problem.

5.3.2. REDUCTION OF UNCERTAINTIES

Experimental data (shown in Figure 3.8b) is now introduced in (5.8) in order to identify the input parameters of the wind turbine, introduced in the previous sec-

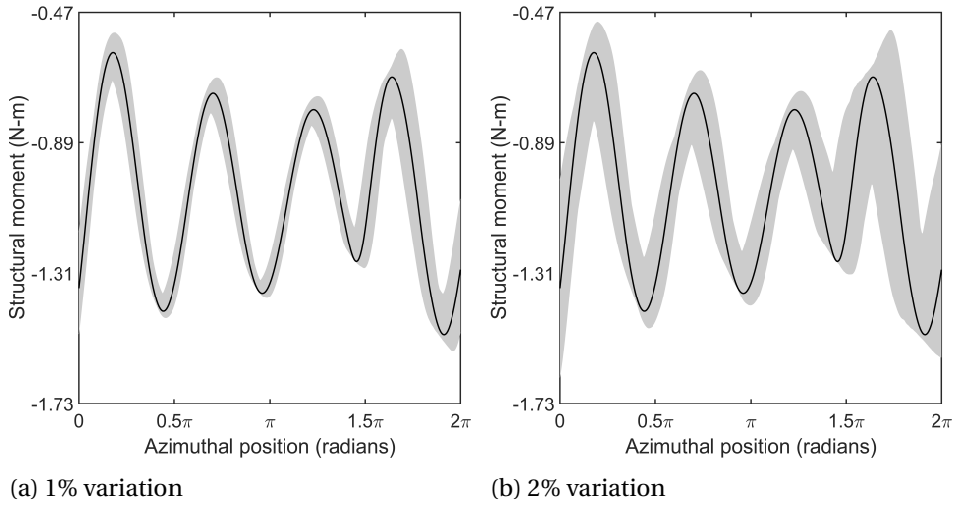


Figure 5.7: Confidence intervals for structural moment at 30%-span location of blade 1 at $\text{TSR} \approx 1.55$ assuming uniformly distributed localised forcing term in the ARX model.

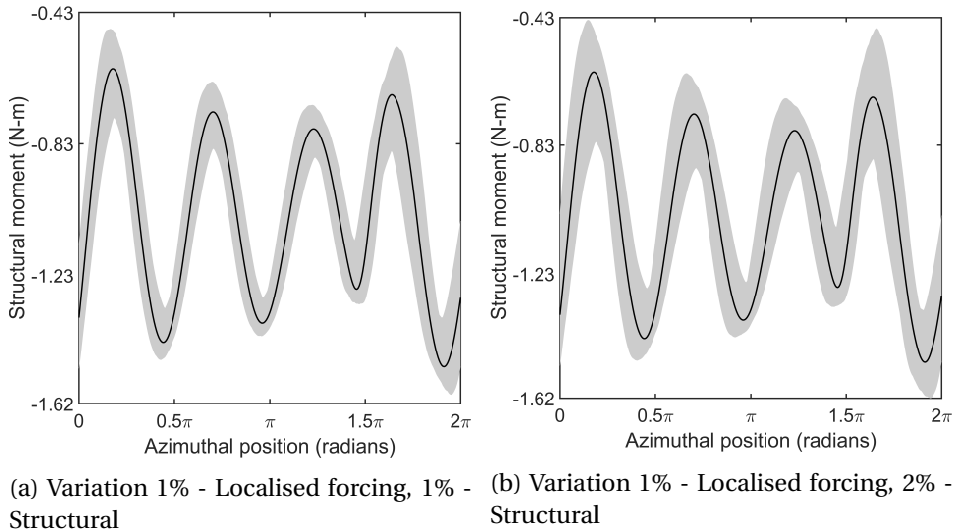


Figure 5.8: Confidence intervals for structural moment at 30%-span location of blade 1 at $\text{TSR} \approx 1.55$ assuming uniformly distributed localised forcing term and structural parameters - Mass, Young's modulus and moments of inertia I_x and I_y in the ARX model.

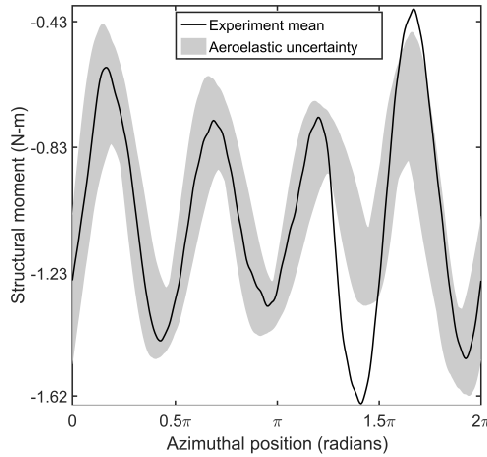


Figure 5.9: Experimental mean and structural moment response for 1% and 2% variations in localised forcing and structural parameters.

tion. As already discussed, in this section, we consider 2% and 1% variation in \mathbf{s} and \mathbf{g} respectively. It may be noted here that the localised forcing vector is composed of the multiple locations, where localised forcing terms are introduced in the ARX model, thus referring to the different azimuthal locations. Figure 5.9 shows the comparison of the considered uncertainty with respect to the mean of the experimental measurements. In the Bayesian reduction problem, there are two considerations in the analysis presented here. First, the aeroelastic uncertain response has significant overlaps with respect to the experimental mean at most azimuthal positions, except near the 1.5π azimuthal position. Around this point when the blade is in front of the tower, the discrepancy is large. Secondly, there is large variance in the experimental measurements, as shown in Figure 3.8b. Thus, three different scenarios with respect to the data used for identification are considered, which are identified with acronyms:

- FT OV: Full time or azimuthal position history is considered, with the original variance reported in the experiment
- FT RV: Full time or azimuthal position history is considered, with a reduced variance (of 1% with respect to original).
- RT OV: Reduced time or truncated azimuthal position history is considered, where the data near the 1.5π azimuthal position is ignored, and the original experimental variance is assumed. The truncated time history avoids the time instances where there is large discrepancy, which is around the 1.5π position.

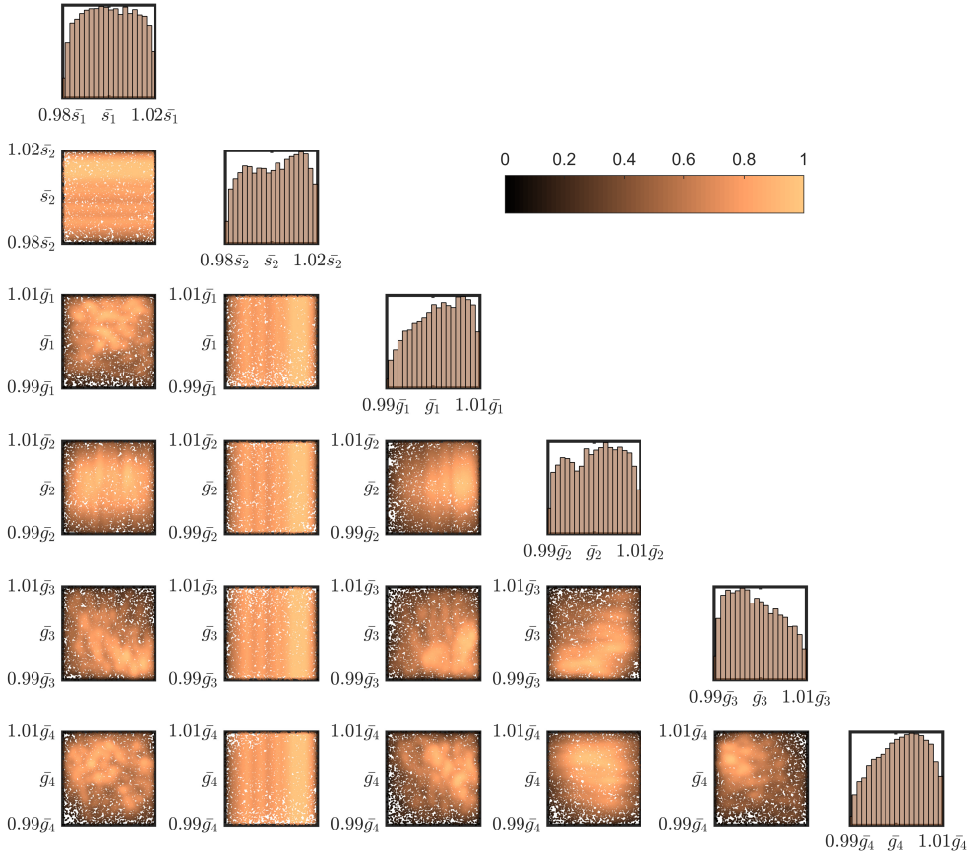


Figure 5.10: Posterior distributions with 1-D marginals of structural parameters s_1 and s_2 , localised forcing parameters g_1 - g_4 and 2-D scatter plots for each parameter pair with data **FT OV**.

The posteriors for the two structural parameters s_1 and s_2 (which are distributions of mass and Young's modulus of the blade respectively) and the four localised forcing parameters are presented with respect to these acronyms in Figures 5.10 - 5.12. Other parameters are not presented for conciseness. The density of samples in the 2-D marginals is represented in the legend, indicating increasing data density from 0 to 1. In Figure 5.10 for data scenario **FT OV**, the 1-D marginals indicate that the structural parameters are not identified, while localised forcing parameters g_1 , g_3 and g_4 are somewhat identified with the mean moment tending towards the extreme range. Similarly, the 2-D marginals show that certain localised forcing terms are correlated. For example, g_3 and g_4 are tending towards a positive correlation with a positive offset for g_4 , while g_2 and g_4 resemble a negative correlation.

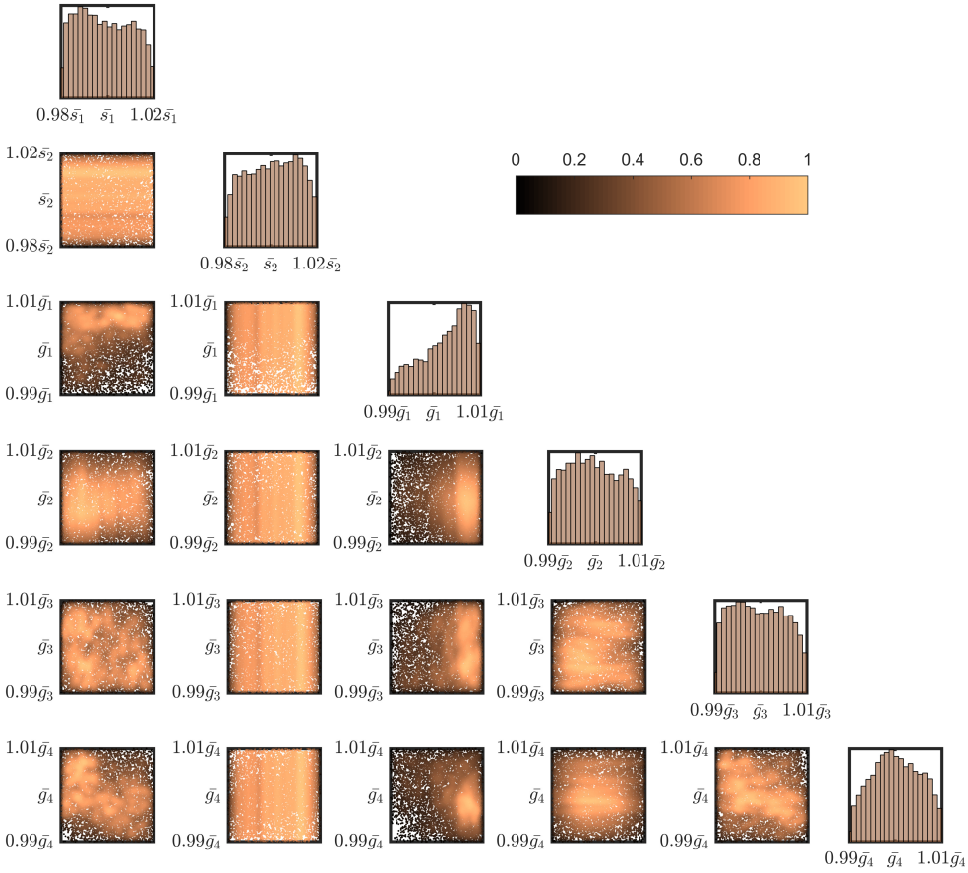


Figure 5.11: Posterior distributions with 1-D marginals of structural parameters s_1 and s_2 , localised forcing parameters g_1 - g_4 and 2-D scatter plots for each parameter pair with data FT RV.

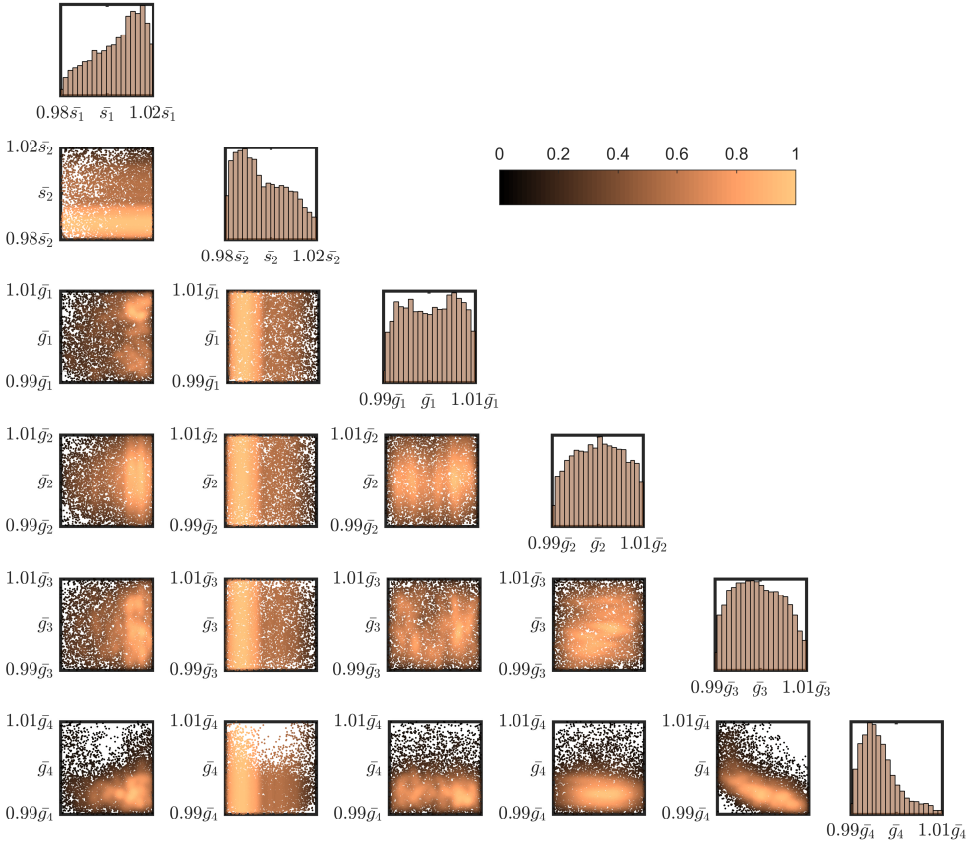


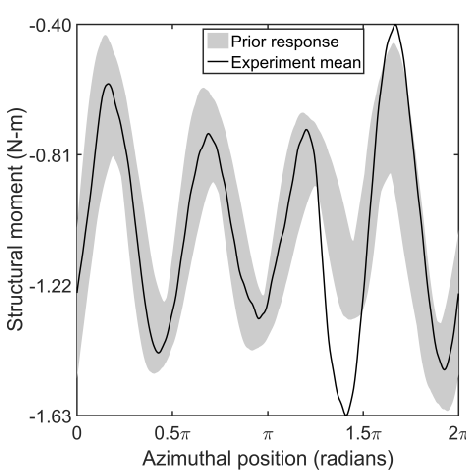
Figure 5.12: Posterior distributions with 1-D marginals of structural parameters s_1 and s_2 , localised forcing parameters g_1 - g_4 and 2-D scatter plots for each parameter pair with data **RT OV**.

In the next data scenario **FT RV**, we reduce the variance to 1% of the original value reported in the experiment, which is shown in Figure 5.11. The reduction of variance clearly identifies the localised forcing parameters g_1 and g_4 , as can be seen in the 1-D histograms. The 2-D marginals reveal the parameter dependencies much clearly. Localised forcing parameters g_1 and g_4 are concentrated towards the edge of the prior range assumed. Parameters s_1 and g_4 also show a concentration towards the upper edge of the prior uncertain domain. In both the cases with the full azimuthal position history, the structural parameters are not clearly identified. On the other hand, the localised forcing parameters g_1 and g_4 defining the location of the tower wake forcing is identified.

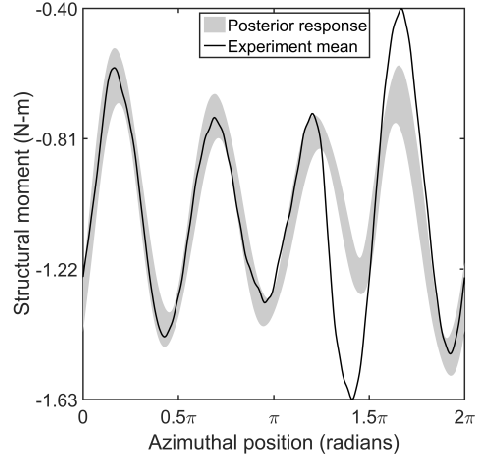
In order to investigate the poor identification of the structural parameters, we select a truncated azimuthal position history from the experimental data. Explicitly, data between π and 1.3π azimuthal positions (Figure 5.9) are chosen, which is motivated by the phase of the harmonic response of the structural moment being constant with respect to the experimental data during the half cycle. Figure 5.12 shows the posteriors identified with the truncated azimuthal position data. We observe that in this case, both the structural parameters s_1 and s_2 are somewhat identified compared to scenarios **FT OV** and **FT RV**. Also g_3 and g_4 demonstrate skewed posteriors, they show a clear negative correlation in the 2-D histogram. Similarly, s_1 and g_4 is also scattered towards the lower edge of the prior uncertain domain.

The improved identification of the structural parameters with truncated azimuthal position data can be explained from the phase of the structural moment response of the uncertain parameters with respect to the experimental mean. The change in the structural parameters of the wind turbine blade results in a change in the aeroelastic frequency, which induces a phase shift. Consequently, the sum of differences between the structural moments with respect to the experimental data in the likelihood function is large, when summed across different harmonic cycles for the full rotation cycle. On the other hand, consideration of half cycle of the harmonic response (scenario **RT OV**) results in samples that are clearly identified with respect to the experimental data. In the next step, we propagate the posterior distributions to predict the ppd of the structural moment.

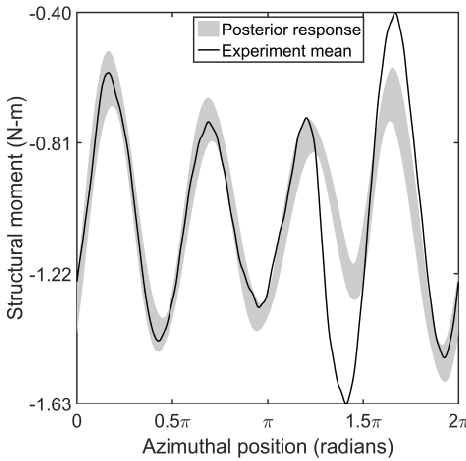
Figure 5.13a shows the confidence intervals under prior distribution for the assumed uncertainty. The confidence intervals using the posteriors under the three data scenarios are shown in Figures 5.13b - 5.13d. The reduction in uncertainty is clearly observed in all the three cases. With the full azimuthal position data (Figures 5.13b and 5.13c), qualitative comparison between the two variances considered in the data is almost identical. In case of **RT OV**, it can be observed that there is a larger reduction in uncertainties at all azimuthal loca-



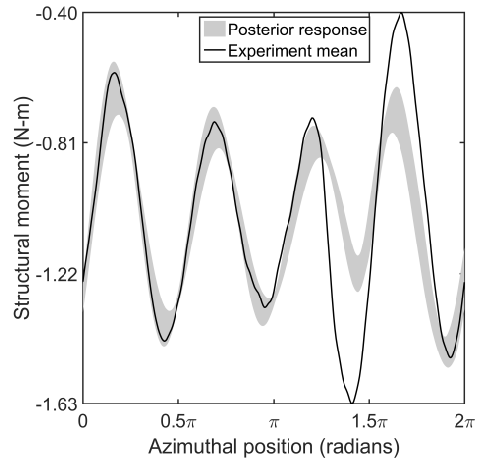
(a) Blade moment response under prior.



(b) Response under posterior with scenario FT OV.



(c) Response under posterior with scenario FT RV.



(d) Response under posterior with scenario RT OV.

Figure 5.13: Posterior predictive confidence intervals of structural moment at 30%-span location of blade 1 at TSR ≈ 1.55 for full cycle of wind turbine blade.

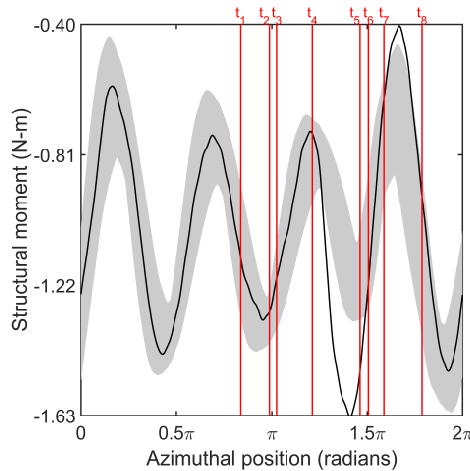


Figure 5.14: Azimuthal positions or time instances at which probability density estimates of structural moment under the prior and posteriors are compared.

tions. In order to obtain a quantitative comparison, we select time or azimuthal position instances and plot the probability density estimates at these locations.

The time instances are marked $t_1 - t_8$, which are selected such that structural moments at crests, troughs and between them are obtained, with more time locations considered around the 1.5π azimuthal position. From Figure 5.15, it is observed that there is reduction in the variance with respect to the prior at all locations. However, comparisons of scenarios **FT OV** and **FT RV** reveal that the reduction in variance of the experimental data does not reduce the uncertainty in blade moment significantly. This is attributed to the experimental data being not informative enough to reduce the uncertainty in structural moment due to change in structural parameters of the blade. This validates our earlier discussion on the choice of a truncated azimuthal position history of structural moment. It can be seen for scenario **RT OV**, there is a reduction in uncertainty at locations t_1 , t_3 and t_7 . All these time instances correspond to azimuthal positions located between the crest and trough, at which the identification data was used in the likelihood. However use of this scenario **RT OV** also leads to change in the mean of the posterior predictive structural moment at locations t_2 , t_5 , t_6 and t_8 . Since the data only corresponds to a half cycle of the experimental data without any information from the tower forcing location, it provides estimates which can be biased.

To summarise, it can be said that the experimental data is not informative enough to identify the structural parameters of the system. The uncertainty due to the forcing from the tower wake can lead to large uncertainties in the structural

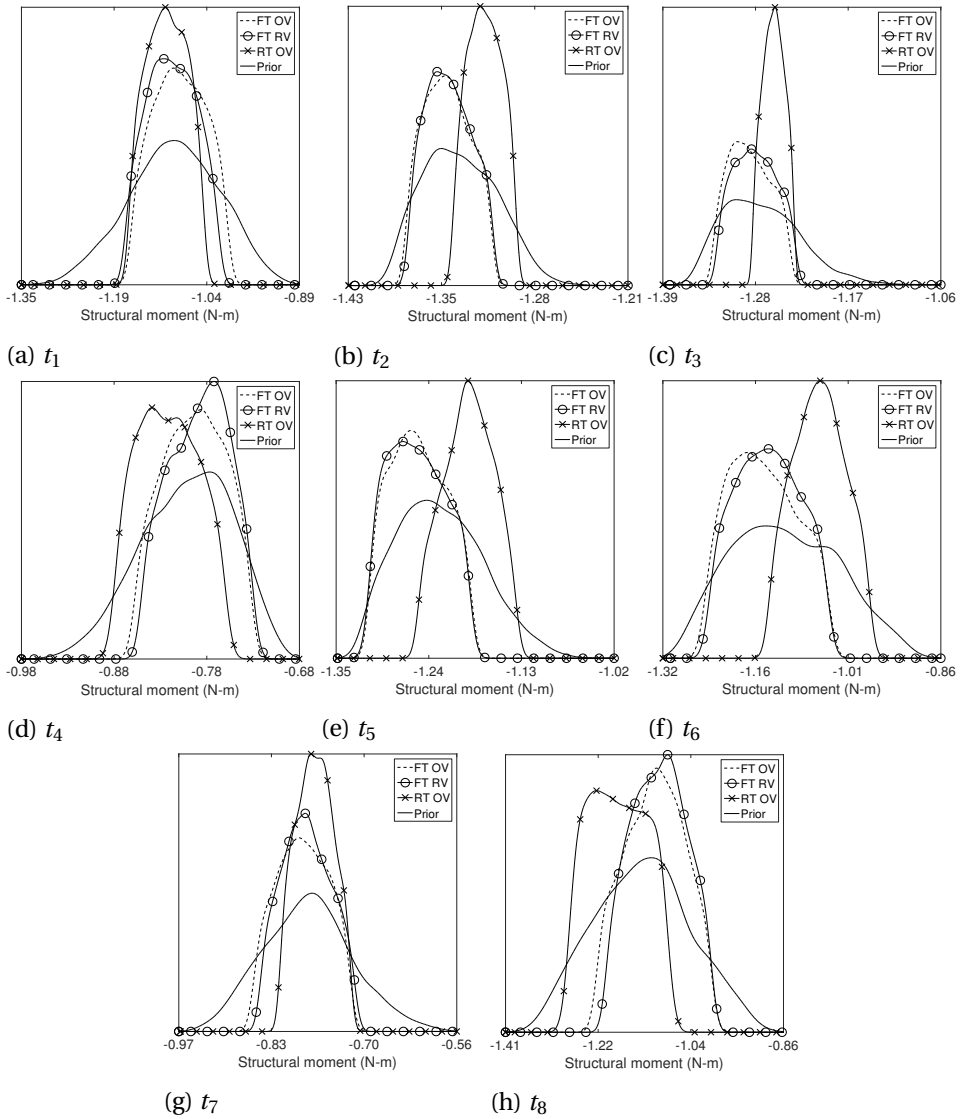


Figure 5.15: Probability density estimates of structural moment at 30%-span location of blade 1 at $TSR \approx 1.55$ for time instances $t_1 - t_8$.

moment. However, due to the complex nature of the wake dynamics, the discrepancy between the experimental uncertainties and aeroelastic responses is large at these locations. As a result, the reduction in uncertainties of the structural moment after identification is not large. However, uncertainties have reduced at all azimuthal positions as evident from Figure 5.13. Also, it has been established that the localised forcing terms, which take into account the tower wake, can be identified with this methodology (Figure 5.11). This uncertainty can be critical in terms of evaluating the fatigue behaviour of a wind turbine blade under uncertain operational conditions.

REFERENCES

- [1] A. Gelman, J. B. Carlin, H. S. Stern, and D. B. Rubin, *Bayesian Data Analysis*, 3rd ed. (Chapman & Hall/CRC, 2004) pp. 6–7.
- [2] H. H. Khodaparast, J. E. Mottershead, and K. J. Badcock, *Propagation of structural uncertainty to linear aeroelastic stability*, *Computers and Structures* **88**, 223 (2010).
- [3] A. O’Hagan and J. E. Oakley, *Probability is perfect, but we can’t elicit it perfectly*, *Reliability Engineering and System Safety* **85**, 239 (2004).
- [4] R. Sarma and R. P. Dwight, *Uncertainty Reduction in Aeroelastic Systems with Time-Domain Reduced-Order Models*, *AIAA Journal* **55** (2017), 10.2514/1.J055527.
- [5] W. Hastings, *Monte Carlo sampling methods using Markov chains and their applications*, *Biometrika* **57**, 97 (1970).
- [6] S. Chib and E. Greenberg, *Understanding the Metropolis-Hastings Algorithm*, *The American Statistician* **49**, 327 (1995).

6

CONCLUSION

This dissertation explores three main scientific challenges as outlined in Section 1.3. In this chapter, the findings of this dissertation, challenges and future research directions with respect to these three domains are summarised. Section 6.1 outlines the contributions in these three domains, while Section 6.2 provides recommendations for further research in aeroelasticity for wind turbines, reduced order modelling in aeroelasticity and Bayesian data assimilation pertaining to aeroelastic problems. Finally section 6.3 summarises the chapter and the dissertation.

6.1. CONTRIBUTIONS OF THE DISSERTATION

6.1.1. AEROELASTIC MODELLING

Aeroelastic models for three test cases – a two-Degree-of-Freedom NACA 0012 airfoil, the Goland wing and wind turbine have been developed and validated. The wind turbine is based on an experimental 3-bladed model. A detailed aeroelastic model of the downwind wind turbine is considered, including all the structural details namely blade, nacelle and tower. The structural model is based on a normal modes solver, while the fluid model is based on a 3D Navier-Stokes solver, employing the RANS turbulence closure, Launder-Spalding $k - \epsilon$ model for airfoil and Goland wing, while the SST $k - \omega$ model is employed for the wind turbine.

For the airfoil and Goland wing, the output quantity of interest is the flutter boundary. Depending on the availability of validation data, the flutter boundary is plotted in the respective coordinate system. For the airfoil, the flutter boundary is plotted in terms of the change in the inverse mass ratio at flutter with the

Mach number. For the Goland wing, the change in free stream velocity at flutter is plotted with respect to the Mach number. The aeroelastic solver for the airfoil is validated with experimental findings, while the numerical test case of Goland wing is verified by comparing the solver estimates to other numerical solvers available in literature. For the wind turbine, structural moment at a span-wise location is the quantity of interest, which is validated against experimental results.

Chapter 3 shows the validation results for the three test cases. The aeroelastic estimates from the developed solver closely match the experimental or numerically obtained flutter boundary, both for the airfoil and Goland wing. The flutter boundary for the airfoil is in close quantitative agreement with the BMP experiment throughout the Mach number range. Both Euler and Navier-Stokes solvers are developed for the Goland wing and the solvers are able to obtain a good qualitative agreement, with an accurate representation of the transonic dip. The error analysis shows that the maximum discrepancy or relative error is less than 5%, and hence the solver is considered to be validated.

As mentioned, the aeroelastic solver for the downwind wind turbine considers all structural details, and hence the mesh generation requires detailed consideration in order to resolve the boundary layer and capture the tower and blade vortices. A hybrid mesh has been employed in this dissertation. For assessing the accuracy of the aeroelastic solver for the wind turbine, the experimental structural moments for each rotation of the turbine are obtained with respect to the azimuthal position. The range of the measurements is found to be large for all azimuthal positions with larger spread when the blade is in front of the tower. The mean structural moment from the aeroelastic solver is able to reconstruct the trend in both the experiments conducted at two values of TSR. The aeroelastic frequencies and the effect of the tower wake on the blade moments are clearly visible.

The wind turbine solver is further investigated extensively for assessing the ability of the solver to reconstruct tower and blade vortices. The dependence of the vortex structures on the TSR is analysed and it is observed that higher TSR at a low inlet air velocity leads to distinct tip vortices, while at a low TSR and a high inlet velocity, the blade vortices are distinct. Furthermore, a low-frequency unsteadiness is observed in the blade moment and an amplitude and frequency modulation dependence on the TSR has been established.

Based on the aeroelastic investigations for all the test cases, it is established that the solvers are able to provide accurate representation of the aeroelastic characteristics with agreement to experimental or numerical benchmarks, which concludes the first numerical challenge of this dissertation. Owing to the computational expense, these validated solvers cannot be employed to provide dy-

dynamic aeroelastic predictions. The high-fidelity solvers are used to generate data in order to train reduced order models, which are presented in Chapter 4.

6.1.2. DATA-DRIVEN ROMs

In this dissertation, data-driven ROMs are developed employing ideas of system identification. Three different ROMs are developed - an ARX model, LPV - ARX model and ARX model with local (Gaussian) forcing term. The ARX model is based on time-marching recurrence relation, mapping input data to output quantities of interest. Throughout this dissertation, the input parameters are the modal displacements of the wing/blade, while the output parameter is the modal force or moment on the wing/blade surface. Coefficients defining the model are first trained using high-fidelity training data. In the LPV-ARX model, the coefficients are parametrised based on the operating conditions. The LPV-ARX implementation enables the use of the ARX model at multiple conditions, which is convenient for performing uncertainty quantification.

The ARX and LPV-ARX models are initially employed to reconstruct test signals in the frequency range of interest. Both single and multi-mode excitation test signals are employed to ascertain the robustness of the ROMs. An error analysis shows that the models are able to reconstruct signals in the frequency range of interest at which the instability or the flutter point is expected. Once verification with test signals is acceptable, the models are employed to predict the flutter boundary of the airfoil and the Goland wing. In both the cases, the ROM is able to predict the flutter boundary accurately with respect to the full solver predictions with significant reduction in the computational costs.

Finally, for the wind turbine, the ARX model is modified by inclusion of a localised forcing term in order to account for the jump in the blade moment due to the tower wake. The local forcing is the form of a Gaussian shape, which corresponds to the effect of the tower wake on the blade moment. As in the other test cases, test (forced) signals are initially reconstructed and then the model is employed to predict blade moment. The model is employed for moment prediction at two values of TSR of the turbine and it is evident that the model is able to predict blade moment accurately. Also the local forcing term is able to represent the modulation in the low-frequency unsteadiness.

The ROMs developed in this dissertation are able to provide accurate predictions of aeroelastic characteristics. This has been achieved with considerable reduction in the computational expense of the solver. The development and verification of the ROM concludes the second numerical challenge of this dissertation. The ROMs are then employed to propagate uncertainties in the input and operational parameters of the system.

6.1.3. UNCERTAINTY REDUCTION

Chapter 5 discusses the uncertainty propagation and reduction section of this dissertation. The methodology for this section is based on prior identification of uncertain input parameters, generation and inclusion of data in a statistical model in order to perform parameter estimation and finally propagation of the identified parameters to reduce the output uncertainty. The test cases of Goland wing and wind turbine are analysed. For the Goland wing, based on a sensitivity analysis, seven structural parameters and the Mach number are considered as uncertain. The input uncertainties resulted in a significant spread in the flutter altitude. Since the Goland wing is a numerical test case and hence in the absence of experimental data, synthetic data from higher fidelity numerical experiments are used to form the likelihood. The posteriors of the structural parameters reveal clear identification of two structural parameters. The propagated posteriors are able to reduce the flutter density significantly. A parametric investigation is also performed based on the location of identification data and the assumed variance in the Gaussian error. It is established that the data from pre-flutter conditions can be used to reduce uncertainties, which establishes the relevance of this dissertation for real-world applications.

For the wind turbine system, the uncertain parameters are: distribution of four structural parameters - mass, Young's modulus, and moments of inertia in two directions. Additionally, based on the experimental observations, rotational uncertainty is also considered. The localised forcing term in the ROM enables implementation of the rotational uncertainty. In the wind turbine, experimental data is employed in the parameter estimation step. It is observed that structural parameters are not clearly identified, while the localised forcing terms defining the rotation are somewhat identified. This is attributed to the large discrepancy between experimental measurements and model predictions at the azimuthal position when the blade is in front of the tower. In order to obtain better identification, a modified data scenario is implemented, which ignores the data where the discrepancy is large. This resulted in better identification of the parameters and reduction in the blade moment uncertainty.

The incorporation of the ROM in the Bayesian framework and the demonstration of the methodology for both numerical and experimental data concludes the third and final numerical challenge of this dissertation. This technique has been demonstrated to be viable for practical applications, both in terms of providing accurate predictions with cheap computational resources and utilisation of experimental data for parameter estimation to improve model predictions. However, the non-conformity between the experimental and model predictions in the wind turbine problem is found to be an issue for the identification. Due to the inadequacy of the model to reconstruct the solution behind

the tower, the uncertainties could not be reduced substantially, which is eventually improved by ignoring the data around azimuthal locations behind the tower. In view of these limitations and other possible developments, future research directions are summarised in the next section.

6.2. DIRECTIONS FOR FUTURE RESEARCH

6.2.1. AEROELASTIC MODELLING

In section 3.4.2, production of large scale vortices from the mid span of the blade is demonstrated, which is attributed to the large change in angle of attack at that location. During the blade design process, these can be avoided by designing the airfoil such that discontinuities along the leading or trailing edge profiles are avoided. This will mitigate the production of large scale vortices, which can negatively impact the power production.

The forcing introduced by the tower vortices on the blade results in sudden jump in the generated blade moment at every rotation of the blade. This effect can result in fatigue of the blade structure. Future research can be directed towards prediction of structural fatigue in downwind turbines utilising the reduced order models developed in this dissertation. The dependence of frequency of the low-frequency unsteadiness of the blade moment and the Tip Speed Ratio of the turbine on development of structural fatigue can be a design consideration in the blade design process.

In terms of increasing the complexity of the computational model, the boundary conditions of the model can be modified to take into account the atmospheric boundary layer (ABL) at the inlet of the domain. The impact of the turbulent nature of the ABL on the wind turbine performance has already been investigated. The topography of the land and variation in the land surface fluxes can significantly impact the wind-farm-atmosphere interactions. Consideration of these factors for the design and optimisation of wind farms is still an ongoing development. In this context, the performance of the aeroelastic model with the presence of the ABL is an interesting area for research. Additionally, presence of ABL can lead to other aeroelastic characteristics with respect to the low-frequency unsteadiness and instabilities, which can be investigated in detail.

Future developments in the computational model could be to incorporate variable rotational speed of the turbine based on integration of pressure field on blade surface. The current model is based on prescribing a fixed rotating speed in the rotating domain of the computational mesh. Variation in rotational speed outside design conditions can be encountered at start-up or shut-down of a turbine or during operation of the turbine due to change in inflow conditions, which was also observed in the reported experiment in this dissertation. The operation

of the turbine and the resulting aeroelastic characteristics on the blade surface can be considered in the extended model.

Furthermore, the structural model for the wind turbine can be improved by taking into account shear deformation, which can be important for low-aspect ratio blades. Additionally, coupling between flapwise bending, edgewise bending and torsional modes can be included to take into account the effect of geometrical twist of the blade. Also, the bend-twist coupling can be considered, which is known to affect the stability characteristics of aeroelastic systems [1].

6.2.2. DATA-DRIVEN ROMS

As mentioned in Chapter 4, the stability of the LPV-ARX model can be defined in a global or a frozen sense (Reference for these are provided in Section 4.2). The frozen method can be applied based on the behaviour of the scheduling parameter. Under the assumption that the scheduling parameter changes slowly, the stability of the global LPV-ARX model can be based on the local identified ARX models. However, future developments in the LPV-ARX model could explore use of stability preserving interpolation methods which guarantee global stability. If the scheduling parameter is expected to change rapidly, extension of the global stability preserving methods can be useful for robustness of the model.

The identification approach of the LPV-ARX model could be further investigated. In Section 2.3, the contributions for global identification methods such as subspace-methods are summarised. Owing to the recent developments in closed-loop systems [2], these could be employed for identifying the dynamical system. The closed-loop approach could also be used for investigating feedback control, which can be crucial component of the aeroelastic system. This would involve a control system in the physical system and the identification data has to be obtained from this closed loop. Considering that the real systems would operate under the influence of a control system, the feedback control system could be integrated in generating the training data.

The choice of interpolation points in LPV-ARX identification is crucial in determining the accuracy of the global model. As mentioned in Chapter 4, earlier investigations have explored optimisation procedures for choice of interpolation points, which resulted in optimal models with respect to computational costs. Future investigations can be directed towards incorporation of a greedy approach for choice of interpolation points based on gradient of the response function with each additional point. Additionally, prior knowledge of the behaviour of the response function with change in operating conditions can be employed for better identification. For example, the flutter boundary is known to develop a transonic dip around the range of Mach numbers near the transonic regime, thus requiring finer resolution of interpolation points in that regime.

Further LPV-ARX implementations may require use of multiple scheduling parameters. In this regard, incorporation of multiple parameters would require multivariate interpolation methods. One of the challenges expected is the choice of the interpolation or the training points for the local ARX models. Use of fine grids can increase computational costs significantly. In this regard, techniques to improve the choice of sampling points to obtain optimality in terms of computational costs can be explored as mentioned above.

As shown in Chapter 4, the ROM developed for the wind turbine includes a localised forcing term to take into account the forcing introduced by the tower wake on the blade. This term is based on the rotational speed of the turbine and also reconstructs the low-frequency unsteadiness of the tower wake. If the low-frequency behaviour of the wind turbine is characterised with respect to an operating parameter of the turbine such as the Tip Speed Ratio, the localised forcing term could be trained based on the obtained parameter dependence. This would further generalise the ROM with better understanding of the training requirements.

Other research directions can be towards development of nonlinear ROMs for predicting nonlinear instabilities such as Limit Cycle Oscillations. Part of the research effort of the author was directed towards developing such models. Recommended directions for further investigations can include, among others: investigation of basis functions used in the ROM expansions and design of training signals. From the experience of the author, extensive investigation for obtaining a correct training signal is required.

6.2.3. UNCERTAINTY REDUCTION

The modelling uncertainty for the case of the wind turbine can be included in order to improve the identification of the uncertain parameters. Since the model is unable to obtain quantitative agreement with respect to the experimental measurements near the tower, the modelling uncertainty may provide better agreements with respect to the truth.

The uncertain structural parameters in the wind turbine uncertainty analysis can be chosen based on a sensitivity analysis. This would allow reduction of the uncertain parameter space and in absence of the ROM, the computational costs of the full model can be reduced.

In the localised forcing term for the wind turbine, the variance of the forcing term can be employed as an additional uncertain parameter. If the low-frequency behaviour is characterised, this term can be useful to incorporate the parameter dependence.

6.3. SUMMARY

The contributions of the dissertation have been summarised with respect to the three numerical challenges introduced in Chapter 1. Within each domain, suitable models, mathematical formulations and techniques for solving the problem has been developed and they have been successfully implemented in all the three test cases that are explored in this dissertation. The implementations are demonstrated to be accurate with respect to experimental or other numerical findings. Based on the three disciplines, this dissertation has presented a technique to predict the stochastic nature of a dynamic aeroelastic characteristic of a system, which can lead to instabilities or fatigue. This method is demonstrated to work on experimental or real world data recorded during the experiment, which is the aim of the dissertation. The entire methodology can be implemented for practical applications in the future. The gaps or future research directions within these disciplines have also been summarised.

REFERENCES

- [1] A. R. Stäblein, M. H. Hansen, and G. Pirrung, *Fundamental aeroelastic properties of a bend – twist coupled blade section*, [Journal of Fluids and Structures](#) **68**, 72 (2017).
- [2] S. T. Navalkar and J.-W. van Wingerden, *Nuclear Norm-Based Recursive Subspace Identification for Wind Turbine Flutter Detection*, [IEEE Transactions on Control Systems Technology](#) **26**, 890 (2018).

ACKNOWLEDGEMENTS

Before starting my journey to Delft, I was anxious about the atmosphere and life that awaited me in the PhD office. To the people outside the community, it is a mystic world occupied by people who are not always able to explain what they are doing. Being able to experience that at HSL 1.01 in TU Delft has indeed taught me many lessons with interesting tales. At times, people in office were not very optimistic, worried about the bug in the code or complaining about the coffee that tasted wrong. Nevertheless, we all lived and experienced it together in the company of colleagues/friends/family, which indeed made great memories and I would like to take this opportunity to thank them for making my time in Delft memorable.

To begin with, I would like to thank my supervisor, Richard Dwight for offering me the PhD position in Delft. Richard has been always supportive and encouraging in our discussions. He allowed me to work independently, which has served me well, even after leaving Delft. His technical analysis and understanding of the problem was always clear and contributed greatly to my research. One thing that really stood out for me was his reviewing of documents. They really helped improve the quality and clarity of the manuscripts.

I am also thankful to Hester Bijl for agreeing to be my promoter. Hester was always filled with energy and encouragement whenever we met. We perhaps met mostly during my final year and in spite of her busy schedule, she provided me the appointments and also reviewed this document. Special thanks to Axelle Viré for collaborating on the wind turbine application. Axelle, your expertise on wind turbines helped me during the final work of my PhD. I appreciate your prompt responses to my queries and also for reviewing my manuscript and this dissertation. I would also like to acknowledge the members of the doctoral committee for reading this dissertation and providing me with important feedback. Your comments have definitely improved the quality of this document and also provided me the opportunity to think about future research directions.

This brings me to my colleagues and friends in the aerodynamics department. Each of you has provided me with a unique and sometimes crazy experience. And when I talk crazy, the first person that comes to my mind (and I am sure many would agree) is Shaafi. You have been a great friend and you really made my time in Delft exciting. I hope that we have many more adventures and exciting trips to come. To Martin, the most UnGerman German I have seen. I

hope you continue to have this cheerful attitude. Your initiatives led to many dinners, which mostly ended being pizza (due to your affinity!). I thank you for all the UQ/Bayes discussions and providing me many technical inputs. Thanks to Wouter Edeling for your technical discussions during the early days and finally helping me with the Dutch translations.

Thanks to Beppe for being a great friend. I hope you are enjoying your time in Torino now and hopefully less tensed. Thanks to Jun, Tiago and Zeno for some intriguing discussions, be it football or politics. To Varun and Yi, the mimetic group within the group. I will always remember your unique personalities and also the hiking trips that we enjoyed together. To Theo, Jacopo, Valeria and Giuseppe Correale, I remember vividly my first few months in NL with you guys. I wish you all the success in your bright careers ahead. To the members of The party, Haohua and Weibo for some amazing hot-pot. I appreciate the company of all my colleagues: Prashant, Alberto, Mustafa, Henri, Iliass, Wouter T., Paul, Jan, Koen, Qingqing, Liesbeth, Mirja, Wouter V., Kyle, Xiaodong, Yu, Alex, Rogier. Special thanks goes to Colette for her prompt responses and assistance in easing out all the bureaucratic stuff for the defense.

This brings me to two of my closest friends, Shantanav and Akash. Thank you guys for being there always. Shantanav, I have to say that you inspired me to go for a PhD. I would like to thank my flatmate and friend, Deepak. Your work ethic has inspired me to work and I wish you the best for your career. Thanks to Rajit and Ashish for your friendship and the many dinners and movie/series nights. I would like to express my gratitude to Gaurav, Darwin, Aayush, Sanjeev, Sumit, Mishra, Ram, Uttiya, Devashish, Avinash, Ashish for all the wonderful moments. Special thanks to Ritukesh, Antaran, Prarthana and Ekata. I will always remember all our get-togethers and the great times we shared.

I would like to thank my mother, Saraswati Sarma for always providing me with everything. Your sacrifices are the fundamental foundation to anything I achieve. Thanks to my father, Kailash Sarma, for enduring hardships to provide for me in difficult times. To my sisters, Neeta, Moni and Bini Ba for your constant presence, love and helping me in everything since I was born. I will never be able to return what all five of you have done for me. Thanks to Bablu, Amitabh and Bhaskar Bhideu for your friendship, encouragement and assistance. To my small nephews, Titu and Dimpu for the fun-filled moments. I am indebted to my companion, Lupa, for being a constant motivation and encouragement all these years. I wish and I know that you will achieve all your dreams. Final thanks to my cousin, Violina for your friendship, support and being there for me always. I am sure you will soon write my name in such a document.

14 November 2018, Amsterdam
Rakesh Sarma



CONFIDENCE INTERVALS OF BLADE MOMENT

The confidence intervals of structural moment and generalised forces for blades #2 and #3 considering uncertainty in structural parameters in shown here for completeness. Corresponding results for blade #1 are in Section 5.3.1. The four structural parameters that are considered uncertain are - Sectional distributions of Mass, Young's modulus, moments of inertia I_x and I_y . Variations of 1%, 2% and 5% on the bounds of the uniform distributions are assumed. The large variation of structural moment with increase in structural uncertainty (e.g. with 5%) is observed to be significant. The structural moment variation provides an idea on the amount of uncertainty that is employed to define the uncertainty problem for the Bayesian identification problem.

The difference in response for structural moment and generalised force is also observed for blades 2 and 3. It is interesting to observe the difference in uncertainty introduced in structural moment and generalised force by 5% variation in the parameters. The impact of the tower wake observed in the generalised force is much higher compared to the structural uncertainty. On the other hand, the variation introduced in the structural moment is significant. This is attributed to the difference in response to the tower wake for structural moment and generalised force. Due to inertia, the structure does not respond abruptly as compared to the corresponding change in the generalised force.

A

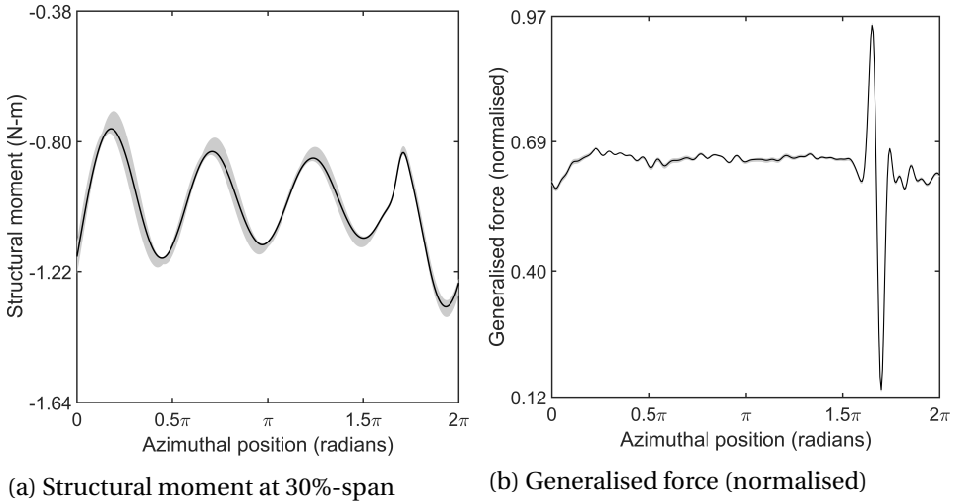


Figure A.1: Confidence intervals for **blade 2** at $\text{TSR} \approx 1.55$ assuming uniformly distributed input parameters - Blade sectional distribution of Mass, Young's modulus, moments of inertia I_x and I_y with **1% variation** on uniform distribution bounds.

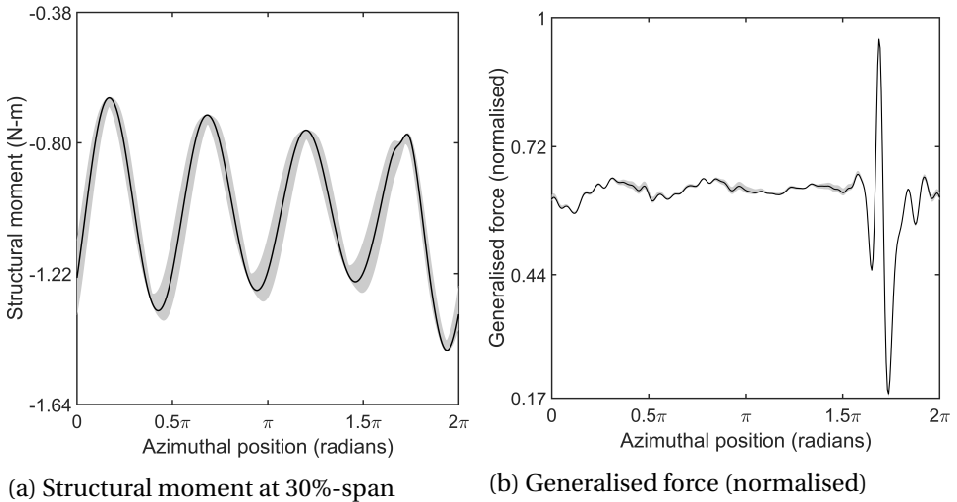


Figure A.2: Confidence intervals for **blade 3** at $\text{TSR} \approx 1.55$ assuming uniformly distributed input parameters - Blade sectional distribution of Mass, Young's modulus, moments of inertia I_x and I_y with **1% variation** on uniform distribution bounds.

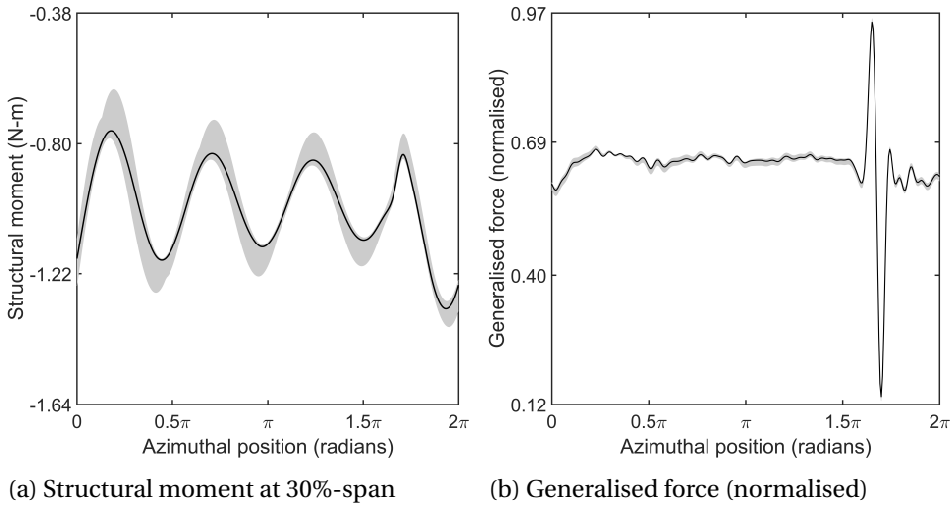


Figure A.3: Confidence intervals for **blade 2** at $\text{TSR} \approx 1.55$ assuming uniformly distributed input parameters - Blade sectional distribution of Mass, Young's modulus, moments of inertia I_x and I_y with **2% variation** on uniform distribution bounds.

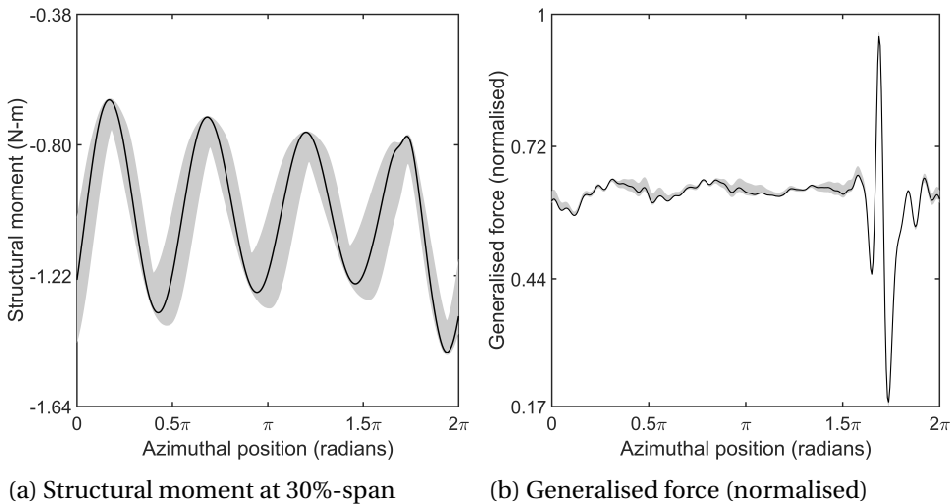


Figure A.4: Confidence intervals for **blade 3** at $\text{TSR} \approx 1.55$ assuming uniformly distributed input parameters - Blade sectional distribution of Mass, Young's modulus, moments of inertia I_x and I_y with **2% variation** on uniform distribution bounds.

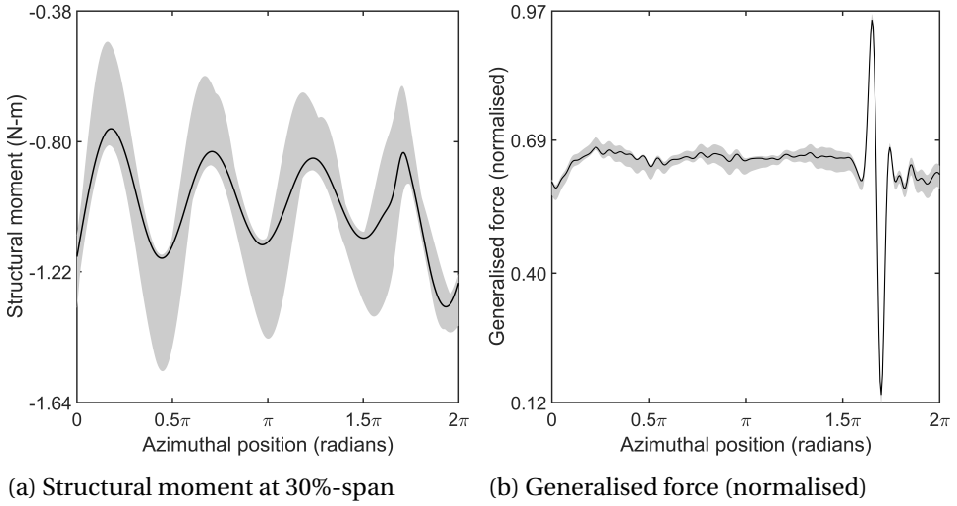


Figure A.5: Confidence intervals for **blade 2** at $\text{TSR} \approx 1.55$ assuming uniformly distributed input parameters - Blade sectional distribution of Mass, Young's modulus, moments of inertia I_x and I_y with **5% variation** on uniform distribution bounds.

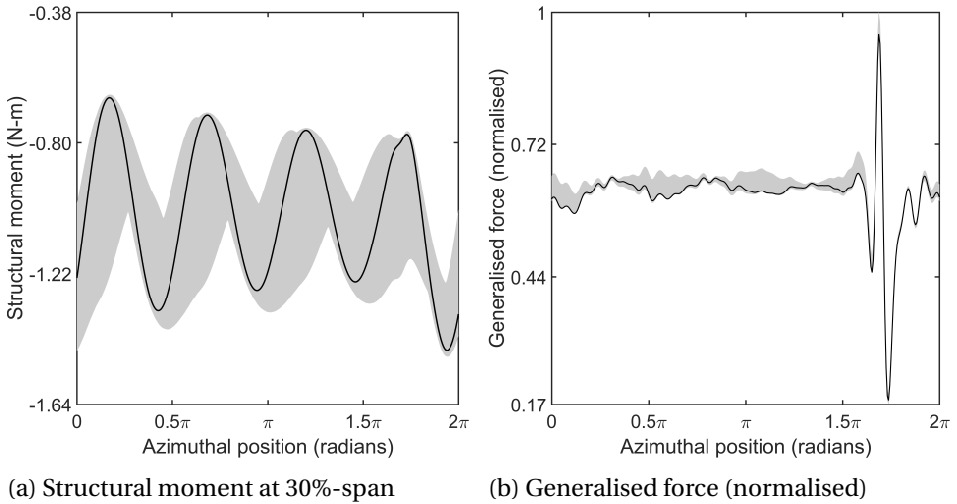


Figure A.6: Confidence intervals for **blade 3** at $\text{TSR} \approx 1.55$ assuming uniformly distributed input parameters - Blade sectional distribution of Mass, Young's modulus, moments of inertia I_x and I_y with **5% variation** on uniform distribution bounds.

B

INFINITE PLATE SPLINE

The aeroelastic system consists of the fluid and the structural meshes. The nodes used for defining the structural mesh, (x_s, y_s) in aeroelastic simulations are significantly fewer than those of the fluid mesh, (x_a, y_a) . Hence the structural and fluid meshes are not conforming, which requires an interpolation technique. The Infinite Plate Spline method is implemented in this dissertation, which is explained in more detail here.

The Infinite Plate Spline was developed by Harder and Desmarais in 1972. The method is based on the superposition of solutions obtained from the partial differential equations of an infinite plate. Point loads are applied at known data points and the corresponding deflections are calculated. A smooth surface passing through the structural points is obtained by substituting these loads back into the solution. The surface obtained can then be used to estimate the deflection of the fluid mesh. The differential equation relating the deflection and loads applied to a plate is given by:

$$\mathcal{D}\nabla^4\delta z = q. \quad (\text{B.1})$$

Here \mathcal{D} is the plate flexibility, δz is the deflection of the plate and q is the distributed load. The solution of this problem is given by

$$\delta z(x, y) = a_0 + a_1x + a_2y + \sum_{i=1}^N F_i r_i^2 \ln r_i^2, \quad (\text{B.2})$$

where r_i is the distance from point (x, y) to the structural point $(x_{s,i}, y_{s,i})$. The $N+3$ unknowns a_k and F_i are calculated by applying force and moment equilibrium,

given by:

$$\begin{aligned}\sum F_i &= 0, \\ \sum x_i F_i &= 0, \\ \sum y_i F_i &= 0,\end{aligned}\tag{B.3}$$

and the N known deflections δz_i . Equation (B.2) can be written in matrix form as:

$$\delta z(x, y) = \begin{bmatrix} 1 & x & y & K_1(x, y) & \dots & K_N(x, y) \end{bmatrix} \begin{bmatrix} a_0 \\ a_1 \\ a_2 \\ F_1 \\ F_2 \\ \vdots \\ F_N \end{bmatrix}, \tag{B.4}$$

where $K_i(x, y) = r_i^2 \ln r_i^2$. Applying the equilibrium conditions with the surface passing through the structural mesh, the system of equations becomes:

$$\begin{bmatrix} 0 \\ 0 \\ 0 \\ \delta z_{s,1} \\ \delta z_{s,2} \\ \vdots \\ \delta z_{s,N} \end{bmatrix} = \begin{bmatrix} 0 & 0 & 0 & 1 & \dots & 1 \\ 0 & 0 & 0 & x_{s,1} & \dots & x_{s,N} \\ 0 & 0 & 0 & y_{s,1} & \dots & y_{s,N} \\ 1 & x_{s,1} & y_{s,1} & 0 & \dots & K_{1,N}^s \\ 1 & x_{s,2} & y_{s,2} & K_{2,1}^s & \dots & K_{2,N}^s \\ \vdots & \vdots & \vdots & \vdots & \ddots & \vdots \\ 1 & x_{s,N} & y_{s,N} & K_{N,1}^s & \dots & 0 \end{bmatrix} \begin{bmatrix} a_0 \\ a_1 \\ a_2 \\ F_1 \\ F_2 \\ \vdots \\ F_N \end{bmatrix} = [\mathcal{C}][F], \tag{B.5}$$

where $K_{i,j}^s$ is the function K_j evaluated at the i -th structural point. The equation can be solved for the unknown vector F . The displacements at M fluid nodes can be evaluated as:

$$\begin{bmatrix} 0 \\ 0 \\ 0 \\ \delta z_{a,1} \\ \delta z_{a,2} \\ \vdots \\ \delta z_{a,M} \end{bmatrix} = \begin{bmatrix} 1 & x_{a,1} & y_{a,1} & K_{1,1}^a & \dots & K_{1,N}^a \\ 1 & x_{a,2} & y_{a,2} & K_{2,1}^a & \dots & K_{2,N}^a \\ \vdots & \vdots & \vdots & \vdots & \ddots & \vdots \\ 1 & x_{a,M} & y_{a,M} & K_{M,1}^a & \dots & K_{M,N}^a \end{bmatrix} [\mathcal{C}^{-1}] \begin{bmatrix} 0 \\ 0 \\ 0 \\ \delta z_{s,1} \\ \delta z_{s,2} \\ \vdots \\ \delta z_{s,N} \end{bmatrix}. \tag{B.6}$$

A linear relationship between the structural and fluid node points is obtained by taking the product of the terms on the right hand side of equation (B.6), which is

known as the transformation matrix T ,

$$\delta z_a = T \delta z_s. \quad (\text{B.7})$$

The forces from the fluid mesh f_a to the structural mesh f_s can be transferred by application of the principle of virtual work, which ensures conservation of energy. The virtual work is given by:

$$W = \delta z_s^T f_s = \delta z_a^T f_a. \quad (\text{B.8})$$

Putting equation (B.7) in equation (B.8), the relationship between the forces can be obtained as:

$$f_s = T^T f_a. \quad (\text{B.9})$$

Relations (B.7) and (B.9) are employed in the transformations between fluid and structural meshes of the aeroelastic system.

C

IMPLEMENTATION OF ARX

The ARX model is obtained by solving for unknown coefficients, which is estimated based on training the model with data generated from forced motion signals. A summary of the steps involved in the model generation for an aeroelastic test case is provided here.

1. Develop modal solver for the structure, for example as shown in Section 3.1.3 for wind turbine blades. The modal solution provides the natural frequencies of vibration and mode shapes of the structure. The modal matrix ϕ is formed by including a finite number of mode shapes.
2. Based on the natural frequencies identified, training signals $\mathbf{q}^{\dagger(t)}$ are designed. For example, chirp signals are used in this dissertation and an overlap of training frequency and operating frequency has to be ensured as shown in Figure 4.3.
3. Steady state solution of the Euler/Navier-Stokes solver is obtained.
4. Forced motion aerodynamic simulations are performed in order to generate training inputs $\mathbf{q}^{\dagger(t)}$ (modal displacements), and outputs $\mathbf{F}^{\dagger(t)}$ (modal forces) as given by (4.4). It is to be noted that the displacement is prescribed based on the modal displacement, from which the mesh displacement is obtained by multiplying with ϕ .
5. A least squares solution for the coefficients A_F , A_q of the ARX model is formulated, such as given by (4.5).
6. The order of A_F , A_q is optimised such that the error in reconstruction of the training signal is minimised.

7. The steady state solution is used to obtain the initial solution, when ARX is used for prediction.
8. The model is coupled to a structural solver and is used to predict aeroelastic characteristics, such as flutter point is predicted by (4.23).

For other versions of the ARX solver, namely LPV-ARX and ARX with Gaussian forcing, the primary steps remain the same as above, except with additional terms.

BIOGRAPHY

Rakesh SARMA

Rakesh Sarma was born on 17 December, 1987 in Guwahati, Assam, which is located in the North-Eastern part of India. He was influenced to pursue a scientific career from an early age, drawing inspiration from his elder sisters. Hence after completing his high school in the year 2004 from Don Bosco School Guwahati, he had no hesitation in starting his secondary education in Science from Cotton College, Guwahati. Following the footsteps of many other Indians, he decided to become an engineer and eventually completed a Bachelors degree in Mechanical Engineering from Assam Engineering College Guwahati in the year 2010. At this point, he realised that he wanted to become a researcher in the area of fluid mechanics and started a Master degree in Indian Institute of Technology Jodhpur. He graduated in the year 2013 with a thesis on computational fluid dynamics for solar power application. In September 2013, he started his PhD in TU Delft, this document being the product of his research. Since March 2018, he started working as a post-doctoral researcher in CWI Amsterdam in the field of machine learning for space weather applications. In his free time, Rakesh enjoys reading books, watching football, listening to music, playing badminton, swimming. He is also passionate about hiking, travelling, exploring new cultures and cuisines.

LIST OF PUBLICATIONS

Journals

5. **R. Sarma**, R.P. Dwight, and A. Viré, *Aeroelastic validation and Bayesian updating of a downwind wind turbine*, Journal of Fluids and Structures (2018), in review.
4. **R. Sarma**, and R.P. Dwight, *Uncertainty Reduction in aeroelastic systems with Time domain ROMs*, [AIAA journal](#) **55**, 7 (2017).
3. P. Sharma, **R. Sarma**, L. Chandra, R. Shekhar, P.S. Ghoshdastidar, *Solar tower based aluminum heat treatment system: Part I. Design and evaluation of an open volumetric air receiver*, [Solar Energy](#) **111** (2015).
2. P. Sharma, **R. Sarma**, L. Chandra, R. Shekhar, P.S. Ghoshdastidar, *On the design and evaluation of open volumetric air receiver for process heat applications*, [Solar Energy](#) **121** (2015).
1. G. Singh, D. Saini, N. Yadav, **R. Sarma**, L. Chandra, R. Shekhar, *Dust Deposition Mechanism and Cleaning Strategy for Open Volumetric Air Receiver Based Solar Tower Sub-systems*, [Energy Procedia](#) **69** (2015).

Conferences

5. **R. Sarma**, R.P. Dwight, and A. Viré, *Efficient time-domain ROMs for aeroelasticity and UQ in downwind turbines*, [7th European Conference on Computational Fluid Dynamics](#), Glasgow, 2018.
4. **R. Sarma**, R.P. Dwight, and A. Viré, *Bayesian updating of uncertainties in an experimental downwind turbine*, [7th European Conference on Computational Fluid Dynamics](#), Glasgow, 2018.
3. **R. Sarma**, R.P. Dwight, and A. Viré, *Bayesian identification of structural parameters and instabilities in aeroelastic wind turbines*, [11th ASME Conference on Energy Sustainability](#), Charlotte, 2017.
2. **R. Sarma**, and R.P. Dwight, *Reducing Epistemic Uncertainty of Fluid-Structure Instabilities through ROMs*, [SIAM Conference on Uncertainty Quantification](#), Lausanne, 2016.
1. **R. Sarma**, and R.P. Dwight, *System Identification for uncertainty quantification in aeroelastic problems*, [ECCOMAS Thematic Conference on UQ in Computational Sciences and Engineering](#), Crete, 2015.